THE UNIVERSITY OF CHICAGO

FERMION MEDIATED INTERACTIONS IN QUANTUM DEGENERATE ^{133}CS-^{6}LI BOSE-FERMI MIXTURES

A DISSERTATION SUBMITTED TO
THE FACULTY OF THE DIVISION OF THE PHYSICAL SCIENCES
IN CANDIDACY FOR THE DEGREE OF
DOCTOR OF PHILOSOPHY

DEPARTMENT OF PHYSICS

BY
GEYUE CAI

CHICAGO, ILLINOIS
MARCH 2025

ABSTRACT

Quantum simulation with ultracold quantum gases is one of the important building blocks of modern Atomic, Molecule and Optics physics (AMO physics). Benefiting from the clean and versatile experimental platforms, quantum simulation emphasizes building connections with other physics systems. In recent years, it has remained at the very frontier of modern physics research. Among topics of quantum simulation, Bose-Fermi mixtures present unique scientific interests. From the theoretical point of view, a majority of important physics mechanisms involves both bosons and fermions. In the meantime, harder challenges arising from experimenting with two or more species encourage experimentalists to develop more advanced platforms. Mediated interaction is a fundamental and widely observed phenomenon in many physical systems ranging from conventional superconductivity, Coulomb interaction, giant magnetoresistance to Yukawa interaction. Mediated interaction is no exception, being a vital concept in Bose-Fermi mixtures.

This thesis presents experiments with quantum degenerate ^{6}Li-^{133}Cs Bose-Fermi mixtures, with its focus on fermion mediated interaction. We have created the first quantum degenerate fermionic ^{6}Li bosonic ^{133}Cs mixtures and found the first experimental observation of fermion mediated interaction with a Bose-Einstein condensate(BEC) in mixture system. Encouraged by this observation, we study sound propagation in BECs with fermion mediated interactions. A significant dependence of BEC sound speed on the Bose-Fermi interaction strength a_{BF} is observed, which indicates the fundamental impact of mediated interactions on Bose-Fermi mixtures.

Eventually, we extend our study towards challenging strong interaction regime where Bose-Fermi interaction scattering length $|a_{\mathrm{BF}}|$ is comparable to Fermi wavelength $1/k_{\mathrm{F}}$. With advancement in observation toolbox, we made the first observation of a new resonance in the strong interaction regime, which indicates a possible boson-boson pairing mechanism originating from mediated interaction. This newly observed resonance would help reveal

the fundamental underlying connection between many body aspect of mediated interaction induced pairing and few body aspect of Efimov physics.

Our investigation represents significant progress in understanding of fermion mediated interaction mechanism in Bose-Fermi mixtures. It offers a more complete physics picture of Bose-Fermi mixtures in a different parameter regime. The observation of possible boson-boson pairing induced by fermions, sheds light on strongly interacting Bose-Fermi quantum gases research and will hopefully encourage new ideas and theories for strong interacting Bose-Fermi mixture.

To my family and friends

TABLE OF CONTENTS

ABSTRACT iii

LIST OF FIGURES viii

LIST OF TABLES xi

1 INTRODUCTION 1
1.1 Ultracold Quantum Gases 1
1.2 Bose-Fermi Mixtures 2
1.3 Fermion Mediated Interaction 3
1.4 Overview of the Thesis 4

2 PREPARING QUANTUM DEGENERATE BOSE FERMI MIXTURES 6
2.1 Vacuum System 6
2.2 Laser Cooling 9
2.3 Ultracold Collision and Feshbach Resonance 15
2.4 Cooling in Dipole Trap 22
2.5 Magnetic Field Control 28
2.5.1 Bitter Coil and Its control 28
2.5.2 Fast field jump 35

3 HIGH RESOLUTION IMAGING OF BOSE-FERMI MIXTURES 41
3.1 Some Theory of Optics 41
3.2 Designing High Resolution Imaging System 43
3.3 Imaging System Optimization 53
3.4 Camera Setting and Imaging Related State 58
3.5 Imaging High Optical Density Cloud 65
3.6 Design flaw and ideas for future improvement 69

4 FERMION MEDIATED INTERACTION: STATIC LIMIT AND SOUND PROPAGATION 71
4.1 Static Limit: Introduction 71
4.2 Effective Trap Frequencies Measurement 74
4.3 Effective Interaction Measurement 76
4.4 Bose-Fermi Soliton 78
4.5 Introduction: Sound Propagation in Bose-Fermi Mixture 81
4.6 Measurement of Sound speed Shift 85
4.7 Sound Mode Revival 90

5 BOSE-FERMI MIXTURE WITH STRONG COUPLING 93
5.1 Theory of Bose-Fermi Mixtures 94
5.1.1 Boson Pairing Induced by Fermion Mediated Interaction 94
5.2 Phase Imprinting Measurement 109
5.3 Excitation and Loss from Mediated Pairing 115
5.4 RKKY-Efimov Transition across Critical Temperature 119

6 OUTLOOK 124
6.1 BCS-BEC Mixtures and 80MHz RF Coil 124
6.2 Bose-Fermi vortex and Pancake trap 125
6.3 Dimensionality of Fermi Gas and Optical Lattice 126
6.4 Further Questions from Fermion Mediated Pairing Project 127

A TAPERED AMPLIFIER MAINTENANCE 129
A.1 Basics on Tapered Amplifier 129
A.2 Toptica TA Repairing 132

B MISCELLANEOUS 141

C LIST OF PUBLICATIONS 142

REFERENCES 143

LIST OF FIGURES

2.1 Block diagram showing the overall structure of the essential vacuum system. . . 9
2.2 Cs energy level diagram of D2 line. 11
2.3 Li energy levels involved in early laser cooling. 12
2.4 Circuit diagram of the Zeeman slower current driver. 13
2.5 Image of fluorescence signal of Cs atom beam. 16
2.6 Illustration of two channel model 20
2.7 Scattering properties for Cs and two lowest ground state Li in commonly used magnetic field range. 21
2.8 A summary of the entire experimental sequence towards dual quantum degeneracy. 24
2.9 Picture of dipole trap layout. 25
2.10 Setup for dipole trapping Engineering. 27
2.11 The bank of electronic boxes for Bitter coil. 29
2.12 Structure of the Bitter coil circuit. 30
2.13 Schematic of circuit for box 5. 33
2.14 Laplace transforms of field response. 37
2.15 Optimized magnetic field jump. 38
2.16 Optimized magnetic field jump using Gaussian filter method 40

3.1 Generalization of optical system 42
3.2 Microscope layout 44
3.3 Design of microscope objective. 45
3.4 Layout of DMD's optical path. 46
3.5 MTF curves of the DMD projection system. 46
3.6 Root mean square spot radius of the DMD projection spot. 47
3.7 Cartoon for the physical setup. 47
3.8 A photo of the physical layout of the vertical imaging system. 48
3.9 Important vertical dimension of imaging system. 50
3.10 Fitted cloud width of BEC with zero scattering length $a_{BB} = 0$ for different vertical microscope objective position. 53
3.11 Fitted zero Bohr BEC Gaussian width versus optical resolution 54
3.12 DMD diffraction. 56
3.13 Microscope objective tilt correction along tight axis of final trap. 57
3.14 Microscope objective tilt correction along shallow axis of final trap. 57
3.15 Comparison of imaging quality before and after the tilting correction. 58
3.16 Dark Current Count vs. CCD Temperature 60
3.17 The four pulses for dual imaging in fast kinetic mode. 61
3.18 Power broadening and interaction shift of microwave pumping. 62
3.19 Hyperfine structure of Cs ground and excited states. 64
3.20 Modified Li RF locking circuit. 65
3.21 Li EOM RF driving circuit. 66
3.22 High density effect causing a modified-modified Beer-Lambert law. 68

4.1 Mediated interactions between Cs atoms by exchanging Li atoms near the Fermi surface. . . . 72
4.2 Dipole oscillations of a Cs BEC immersed in a Li degenerate Fermi gas. . . . 75
4.3 Bare and effective Cs-Cs scattering length. . . . 77
4.4 Formation of Bose-Fermi solitons. . . . 79
4.5 Bosonic quasi-particles (phonons) coupled to a fermionic quantum field. . . . 82
4.6 *In situ* imaging of the phonon propagation. . . . 83
4.7 Sound wave dynamics in Bose-Fermi mixtures with tunable interspecies scattering length a_{BF}. . . . 86
4.8 Sound propagation across the Feshbach resonance. . . . 87
4.9 Zoomed in fine scanning of the position for sound propagation re-emergence. . . . 91

5.1 Bound State of fermion trapped by the double well potential. . . . 97
5.2 Effective potential from mediated interaction. . . . 99
5.3 Energy spectrum and wave function of Cs atom pair. . . . 101
5.4 Energy spectrum of Efimov resonance. . . . 102
5.5 Example of phase shift computation. . . . 104
5.6 Local Fermi wave vector k_F vs. inter species scattering length a_{BF}. . . . 105
5.7 Estimation of fermion density enhancement inside BEC. . . . 106
5.8 Tilmann Enss Model [42] prediction with Increasing Fermion Density. . . . 106
5.9 Predicted resonance position with different models. . . . 107
5.10 Comparing cutoff models. . . . 108
5.11 full model could be approximated by the perturbative RKKY model without a qualitative loss in prediction power . . . 109
5.12 Quantum mixtures of heavy bosonic ^{133}Cs atoms and light fermionic ^{6}Li atoms in different regimes. . . . 110
5.13 Our analysis procedure for phase imprinting experiments. . . . 111
5.14 Dispersion of Cs BEC embedded in a Li degenerate Fermi gas. . . . 114
5.15 Resonant decay and excitation Cs BECs induced by the Li degenerate Fermi gas. 116
5.16 Time-of-flight measurement of heating and loss feature. . . . 117
5.17 Improved bimodal fitting algorithm. . . . 117
5.18 Fermion mediated resonances in the thermal and quantum regimes. . . . 120
5.19 A general summary of Bose-Fermi mixtures in different regimes. . . . 123

6.1 Relevant scattering lengths around a stable Bose-Fermi mixtures are possible. . 125
6.2 A possible schematic of optical lattice layout . . . 127

A.1 Schematic of a laser diode. Picture adopted from Ref. [81] . . . 130
A.2 TA structure, observing direction in perpendicular to active area. . . . 131
A.3 Toptica MOPA TA layout. The 'TASK' unit is where the TA chip locates. . . . 133
A.4 Layout inside the 'TASK' unit. The 'brass wedge' refers to where the two wedges sits . . . 134
A.5 Structure of Eagleyard TA chip. The photo is adopted from [144] to illustrate the structure of TA chip. The inset picture comes from dataset of Eagleyard Toptica 134

A.6 Photo from another angle showing the TA chip structure mounted on the gold bone. This picture is adopted from Eagleyard Toptica's website 135
A.7 Appearance of seed light transmitted through TA chip. 137

LIST OF TABLES

2.1 Useful LiCs oven parameters 8
2.2 Zeeman slower driver monitor output voltage. 14
2.3 Abbrevations in Fig. (2.12) 31

3.1 Useful Vertical Imaging Parameters. 61

A.1 TA output without isolator. 139
A.2 TA output after isolator. 140
A.3 TA output at different injection power 140

CHAPTER 1

INTRODUCTION

1.1 Ultracold Quantum Gases

As I write this thesis, it has been almost 30 years since the first creation of a Bose-Einstein condensate with ultracold ^{87}Rb atoms, which probably marks the birth of ultracold atom research. Since its birth, quantum simulation is one of the most important areas of research with ultracold gases. A famous and so frequently quoted sentence by Richard Feynman pointed out the central, spiritual motivation of quantum simulation research. On the practical side, cold atoms experiments feature versatile and clean control of experimental parameters, which enables their ability to establish connections with other research fields in physics with a relatively low cost, on bench and repeatable experimental schemes. In fact, significant progress in this field is achieved due to the ability to engineer a new class of Hamiltonians. Starting from creation of BECs and degenerate Fermi gases and learning about interaction tuning with Feshbach resonances, to building optical lattice, realizing single site resolution with quantum gas microscope, studying of topological phases and cooling more atomic species or even mixtures, to optical tweezer and polar molecules and magnetic atoms and hybridized system with optical cavities, numerous advancements were made.

With all these techniques in experimental toolbox, hundreds and thousands theoretical proposals have been tested. From superfluids to Ising models, from spin-orbital coupling mechanism to BCS-BEC mechanisms, from quantum chemistry to Mott insulators. Besides, quantum simulation research is important not only for its science value but also as a motivation to develop more advanced scientific equipment and providing detection solutions for other fields. Even nowadays, quantum gases still remains the very frontier of modern physics research

1.2 Bose-Fermi Mixtures

Among the topics of ultracold gas quantum simulation, experiments with Bose-Fermi mixtures have its unique value. Experiments with mixture gases are not simply a linear extrapolation the existing research. The early Bose-Fermi mixtures experiments come from ^{6}Li and ^{7}Li mixture at Laboratoire Kastler Brossel by Christophe Salomon's group [135] and Randall Hulet at Rice [5], as well as heteronuclear mixtures of ^{6}Li and ^{23}Na from Massachusetts Institute of Technology [65], ^{40}K and ^{87}Rb at European Laboratory for Nonlinear Spectroscopy [58]. Later around 2010, our experimental project of fermionic ^{6}Li and bosonic ^{133}Cs, here at Uchicago physics James Franck Institute, started its construction.

A not often noticed fact is: even nowadays, the shopping list for Bose-Fermi mixture is not adequate: Firstly, on the periodic table, there are far more bosonic species than fermionc species. Secondly, the requirement that a convenient tunable interaction requires a broad inter-species Feshbach resonance which naturally requires a stronger coupling of outer shell electrons couple. In other words, Alkaline metal like elements are a better choice than alkaline earth metal elements or others elements. The combined filtering from these two requirements extremely narrows down the choice of selections of fermionic species. For alkali metal elements, this means we need odd number of both neutrons and protons which is for some reason hated by nuclear structures. In fact, ^{40}K is radioactive with extremely long half time indicating the instability of its nucleus. The natural abundance of ^{40}K is only 0.012% meaning an expensive enriched source is needed. ^{6}Li is stable but still has $< 10\%$ natural abundance. In fact, there is almost no other suitable choices except radioactive ^{134}Cs, which would be perfect for next generation Bose-Fermi experiment if reliable supply is possible. The other choice could be ^{195}Pt, with its possible advantage/disadvantage of magnetic moments causing numerous resonances. It also requires UV laser around 300nm. Such latter was not available until recent years. The third choice is using elements with two outer shell electrons, such as Erbium, Ytterbium or Dysprosium and search for inter-species

Feshbach resonances at low field.

Despite experimental difficulty comes that comes with dealing with two atomic species, Bose-Fermi mixtures experiments offer unique value in certain topics. In the study of Efimov physics, the mass imbalance and different interaction and molecular levels provides a very testbed for verifying and exploring theoretical concepts: Especially the universality assumption of Efimov scaling. When it comes to molecular physics, they offer unique platforms to synthesize heteronuclear fermionic molecules [107] which opens the gate for quantum degenerate molecule research and could serve as a electron dipole moment measurement device [2]. Besides, the combination of atoms from both quantum statistics enables a convenient research on polaron physics [163] [51]. Another exciting research topic are BEC-BCS mixtures, which requires adding fermions with two spin states [47] [129], which serves as a platform to test advanced many body theories.

1.3 Fermion Mediated Interaction

Mediated interaction is a widely existing phenomenon in nearly all physics research categories, ranging from condensed matter, high energy physics, optical cavity and cold atom systems. In condensed matter research, phonon mediated interaction between electrons lying in the center of conventional superconductors with progressively more advanced theory developed during its history from early famous BCS theory to more recent Eliashberg-Midgal theory [7]. When it comes to electron-electron interactions, Coulomb interaction arises from the exchange of virtual photons between charges. In solids, the Ruderman–Kittel–Kasuya–Yosida (RKKY) interaction describes the long range interaction between nearby impurities or nuclear spins by exchanging electrons. In the language of quantum field theory, Feynman diagrams often contain particle exchange mechanisms. For example, Yukawa mechanism comes form exchange of Yukawa particle, which is a famous textbook example of how coupling and mediated interaction. Research on cold atoms is no exception, boson mediated

interaction between bosons is discussed in textbook [123] and photon mediated interaction was already investigated few decades ago by Serge Haroche. In recent years, the discovering of fermion mediated interaction [35] [29] [39].

For mediated interaction in different systems, there is an interesting vague 'philosophical' trend behind them: the properties (to be more exact, the induced interaction format) is determined by the property of force carrying particles. An clear example is the Yukawa interaction $V(r) \sim e^{-\mu r}/r$ with μ being mass of gauge Boson, which reduces to the Coulomb interaction when the mediator is a massless boson (photon). In the case of fermions, the Fermi surface is important for such mediated effects. In some sense, the 'sharpness' (T/T_F and dimension) is critical to inducing these interactions [104]. In our Bose-Fermi mixtures of ^{6}Li and ^{133}Cs, particle-hole excitation near the Fermi surface has a tunable coupling with the excitation in the Bose-Einstein condensate. This science part of this thesis begins with studying fermion mediated interaction in the static weakly coupling regime, and gradually paves the way to dynamics of sound mode excitation, and eventually the investigation is pushed into strong interaction regime beyond long wavelength and static limit. The newly observed resonance feature in this regime, is an possible indication of the boson-boson pairing induced by the many-body effect of Fermi sea and indicates its possible connection with few-body Efimov physics.

1.4 Overview of the Thesis

This rest of the thesis is organized as follows:

• Chapter 2 describes the overall process to prepare a dual degenerate Bose-Fermi mixture. I will review essential building blocks of the experimental setup and try to build a picture how the dual species cooling works. In addition, I will provide some tips for experimental troubleshooting.

• Chapter 3 focuses on probing and manipulating of the Bose-Fermi quantum mixtures

with an introduction on aberration and imaging theory.

• Chapter 4 briefly reviews the first two experiments investigating the fermion mediated interactions. The first experiment being the first observation of fermion mediated interaction between bosons in a cold atom system and the second experiment demonstrated the fundamental impact of mediated interactions on dispersion properties in BEC. These two experiments probe the Bose-Fermi mixtures' basic properties and pave the way for later further investigation into the strong coupling regime.

• Chapter 5 presents the investigation on the topic of strongly interacting Bose-Fermi mixtures. This chapter includes some theoretical approaches beyond static and long wavelength limit. After that, it presents the discovery of a newly observed resonance feature in a Bose-Fermi mixture in strong coupling regime, which is a possible verification of 2-body boson-boson pairing by many-body effect and a 3-body boson-boson-fermion Efimov coupling in the many body regime.

• In Chapter 6, I list a few ideas to search for future science, along with some suggestions for system upgrade options which could make our apparatus more versatile and user friendly.

CHAPTER 2

PREPARING QUANTUM DEGENERATE BOSE FERMI MIXTURES

Our versatile experimental apparatus is the foundation for all our experimental efforts. Because we must accommodate both atomic species, this setup presents significant technical and experimental challenges.

In this chapter, I will describe the apparatus and the basic procedures to produce quantum degenerate Bose-Fermi mixtures. Since Jacob Johansen's thesis[79] and Krutik Patel's thesis [120] presented a details discussion this topic, I will focus on previously undiscussed aspects and briefly review the topics which are discussed in these two theses. The goal of this chapter is to review the process to reach dual degeneracy, and possibly, to serve as a good user manual for system issue troubleshot.

2.1 Vacuum System

In typical quantum gas experiments, the number density of atom gas sample are on the order of $10^{18}/m^3$ to $10^{19}/m^3$, with a typical temperature ranging from a few nK to a few μK. Whereas air under atmosphere condition has a number density of $3 \times 10^{25}/m^3$ with temperature of $300K$. To achieve a clean and controllable experimental platform, quantum gas experiments need to be isolated from atmosphere, so that the sample lifetime (usually referred as vacuum lifetime or one body lifetime) is less affected from collisions with air molecules which carry much higher kinetic energies.

For this purpose, these experimental apparatuses must be set up with an ultra-high vacuum (UHV) systems. These systems are carefully designed and assembled with various vacuum parts. These parts are made with carefully chosen and tested material with are compatible under UHV working condition. However, these parts must be cleaned and handled

carefully to avoid any contamination that might cause outgassing under UHV conditions. After the system is assembled, the entire system need to be heated to few hundreds of degree Celsius and pumped with vacuum turbo pump (commonly referred to as baking), to get rid of molecules(commonly water molecules) absorbed when the parts are in contact with air.

After baking, the entire vacuum system undergoes a leak check to ensure the entire vacuum system is properly sealed. In addition to a care vacuum system construction, the high quality vacuum need to be maintain with ion pumps, which are in vacuum parallel metal plates with voltage as high as a few thousand voltages in between, so that the molecules in vacuum are ionized and absorbed by these plates. Furthermore, it is very common that sometimes these ion pumps need to be baked to keep them under good working performance.

Our vacuum system is consists with an dual species oven, a 2D MOT chamber, a Zeeman slower, a main chamber and a science chamber. The dual species oven is a letter 'F' shape steel parts which contains Li metal and Cs metal in it. We heat up the dual species oven so that it generate hot metal vapor for later use. To maintain a good vacuum performance, we keep the oven at a temperature which is just sufficient to generate enough vapor metal vapor pressure. During system operating time, the Li oven is kept at 330°C and the Cs oven is kept at 55°C. Beyond system operating time, these oven are turned off to reduce workload of the ion pumps near the oven end.

In practice, an active locking circuit heat up the Li oven with heat tape, and with aluminum foil surrounding the oven. The aluminum foil reduces the power it took to maintain the oven temperature, and smoothing the temperature profile around the oven. It also reduce the amount of heat release to nearby environment, reduces its effect on nearby optical paths. One the other hand, we use heat conduction to maintain the Cs oven temperature. The Cs oven temperature is passively tuned by changing the number and configuration of surround aluminum foil. In the table below I summarize the important information of the oven:

Since the occasion of oven problem is rare and troubleshot it could be subtle, I would

Li oven temperature	330°C
Cs oven temperature	55°C
heating tape resistance	36Ω
variac voltage	57-60V

Table 2.1: Useful LiCs oven parameters

like to list a few cautions from past experience at the end of this section:

• It is suggested that the oven being turn on at two stages with the first stage reaching roughly the middle point of the aimed temperature. This reduces the risk of vacuum leak from a too fast expansion of vacuum component.

• If you find the oven temperature is MUCH lower than expected, don't crank on variac voltage without figuring out why. Sometimes it comes from shorting of the heating tape, since their external cover are made with fiber glass. Check for shorting in between tape and the chamber and check for the resistance of the entire heating tape.

• In the occasion someone need to re-wrap the oven, please choose high temperature rate heating tapes, so that they do not burnt through the fiber glass cover.

• A lesson we learned from oven change in 2017: due to the very different vapor pressure vs. temperature curves from Cs and Li metal, the Li metal tends to migrate to cold spots on the oven and may block the entire oven. The previous oven is taken down with a big amount of both Li and Cs metal in them. Therefore, it is critical to make sure there is no obvious cold spot where the Li migration process could happen. The oven before 2017 last for 5 years, and the current oven lasts for at least 7 years.

• * A fun and probably not so important fact: When filling a new oven with Cs and Li metal, the operation is performed under nitrogen air environment. However, you would observed that the surface of the Li metal would turn purple. This is due to chemical reaction between nitrogen and Li, forming Li_3N. Fortunately it didn't seems to hurt our vacuum quality in the past.

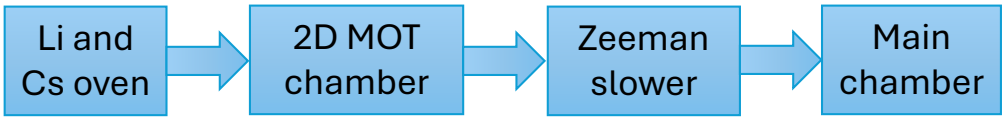

Figure 2.1: Block diagram showing the overall structure of the essential vacuum system. The 2D MOT is designed for Cs only.

2.2 Laser Cooling

As the Li and Cs and heated, their vapor pressure come out of the wedge opening in the oven, and go through the 2D MOT chamber. At this point, the temperature of the atomic vapors are at least 7 or 8 magnitude hotter than our final sample with a speed of few hundreds meter per second, starting from here, we use a combination of different laser cooling techniques to bring down the temperature. To keep things concise, I will divide the cooling stage into early laser cooling and later evaporation cooling stage, each in a separate section.

The following paragraph is a quick review of the basics of atomic transitions. For a more detailed and comprehensive discussion of Li and Cs transitions, I would highly recommend Ref. [143] and Ref. [56]. These are one of the best notes on this topic for Li and Cs.

The principle lying in the heart of early stage laser cooling, is the use of atomic transitions. Both Li and Cs are alkali, meaning their outer shell contain only one electrons. This fact makes their energy level diagram simpler. To build up a general concept, these hydrogen-like atom has a bare Hamiltonian similar to that of a hydrogen. On the top of this, one need to consider orbital angular momentum L, electron spin S and nuclear spin I. Naturally these spins are coupled: the coupling of orbital angular momentum L and electron spin S generate fine structure of the energy levels, whereas further coupling of nuclear spin I give rise to hyperfine structure of the energy level diagram. At low magnetic field regime, these

coupling are more described as Zeeman regime, meaning that the total angular momentum $J = L + S$ and $F = L + S + I$ are good quantum numbers. At high magnetic field, the energy level enters the Paschen-Back regime, which means that the magnetic field is so high such that the coupling in between spin and external magnetic field overwhelm the strength of coupling in between spins. In this case, good quantum numbers are each spin themselves. If the magnitude of these two coupling are comparable, then it is in intermediate regime, in which case no convenient quantum number could be found.

For a quick note, for our experiment, which eventually performing experiment at a magnetic field around 900 G. For Li, both ground and excited state are described by Paschen-Back regime, whereas for Cs, the excited state are in Paschen-Back regime and the ground state is on intermediate regime. Here the term 'excited state' refer to the state relevant to optical pumping during the imaging process at the end of the sequence, which will be discussed a bit more in detailed in chapter 3.

Following the guide of Ref. [143] and Ref. [56], I wrote some Matlab code which would plot the hyperfine energy shift versus magnetic field for relevant for both species. Save your time if you ever need to calculate the hyperfine energy splitting and there should exist a more user-friendly and advanced version by Henry Ando.

Fig. (2.2) and Fig. (2.3) shows the relevant energy level diagram involved for Cs and Li laser cooling separately.

The first not often mentioned step is: the wedged atom beam output (or nozzle in other cold atom systems) ensure the atomic beam came out directionally, which in fact reduces the entropy of the atom beams. Right after the atom beam output, we use a 2D MOT chamber to reduce the divergence of the atom beam. Yet this only works for Cs atom whereas the Li atoms are so light that they will diverge even if we converge them in this stage. In practice, we only use 2D molasses (ie. turn on bias field) configuration here, since we found that the 2D MOT configuration (bias field + field gradient) is not improving the MOT loading stage

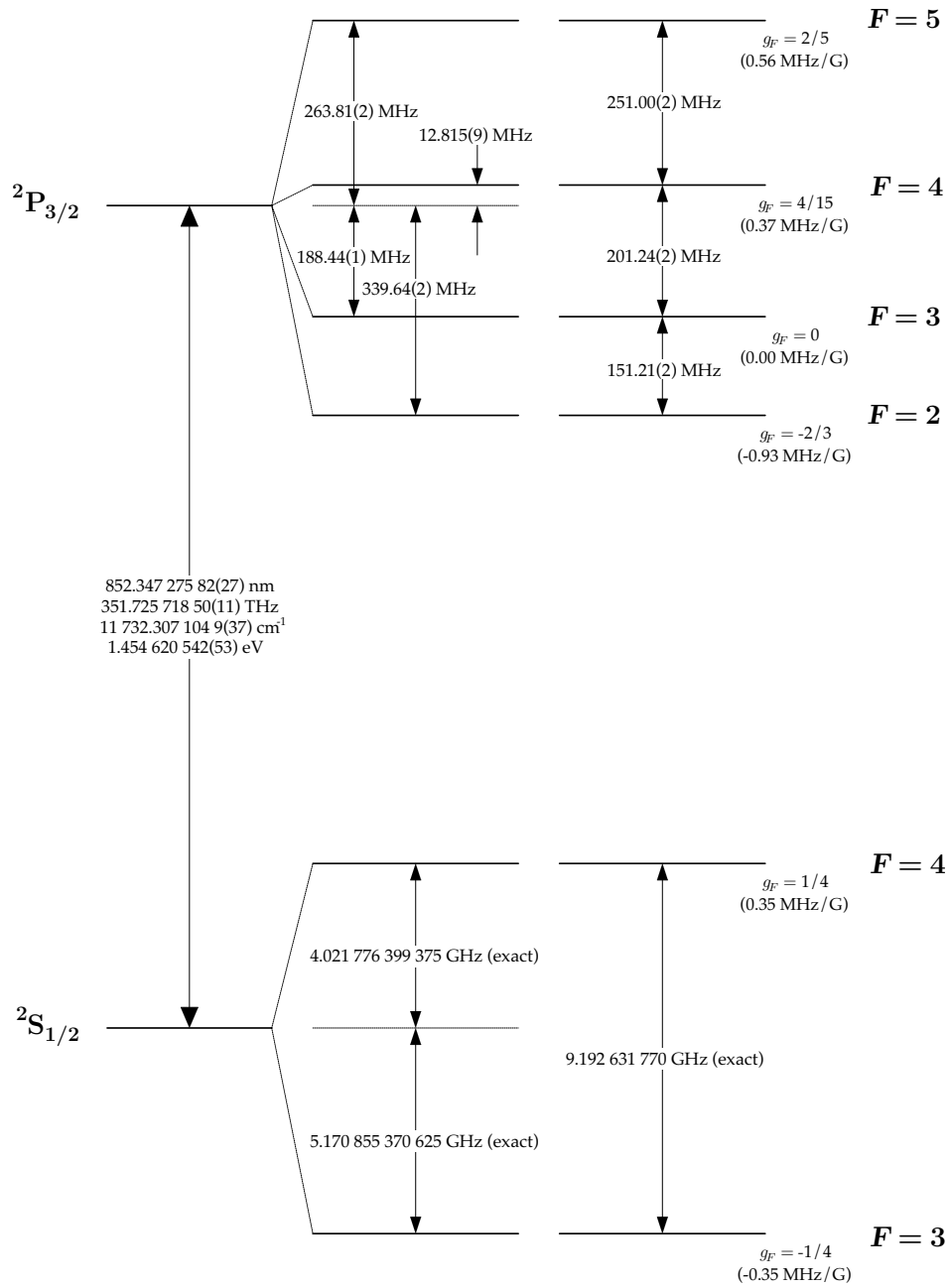

Figure 2.2: Cs energy level diagram of D2 line. During early stages laser cooling, both the ground state and excited state are in the Zeeman regime. The cooling is done via the ground state F = 4 and the excited F = 5 manifold, on the D2 line. This figure is taken from Ref. [143].

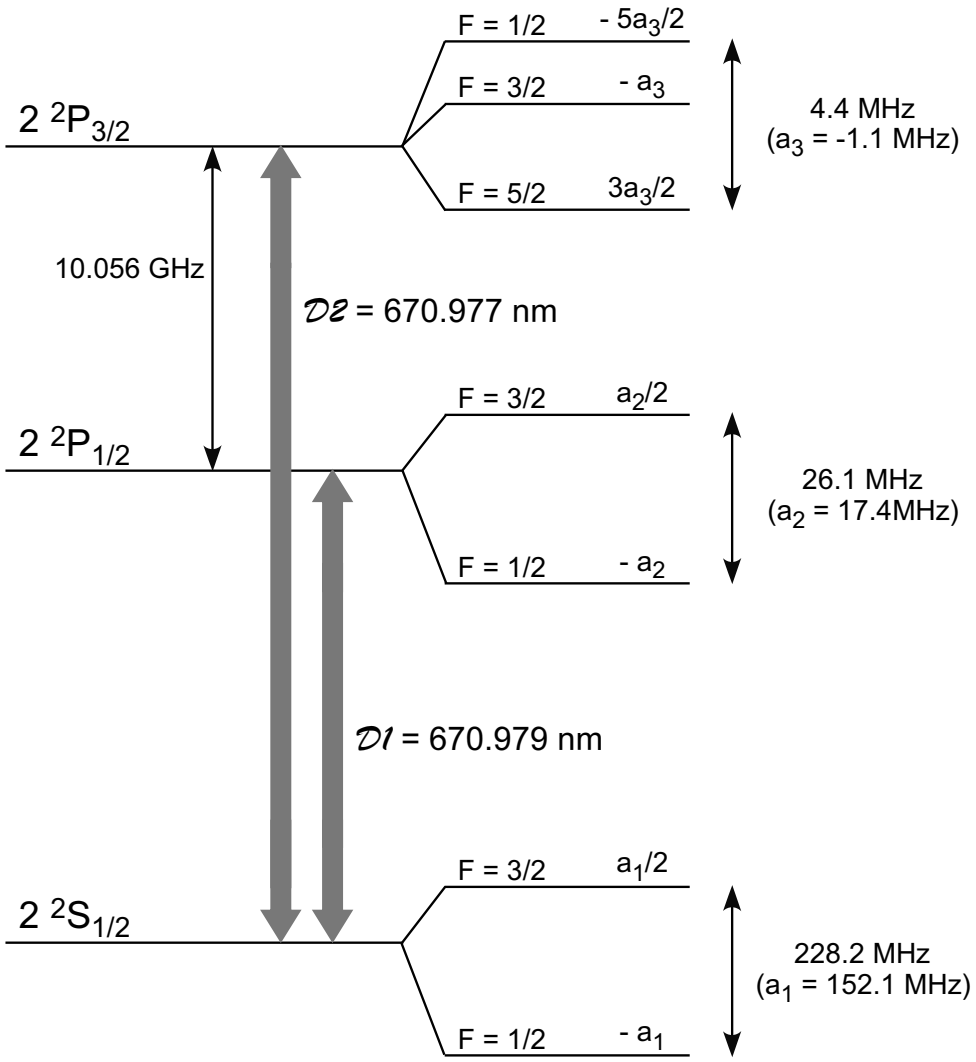

Figure 2.3: Li energy levels involved in early laser cooling. The cooling process is done via the ground state F = 3/2 and the $2\,^2P_{3/2}$. Note that for the excited states, the entire hyperfine structure splitting is only 4.4MHz, which is smaller than the line width from spontaneous decay. This diagram is taken from Ref. [56]

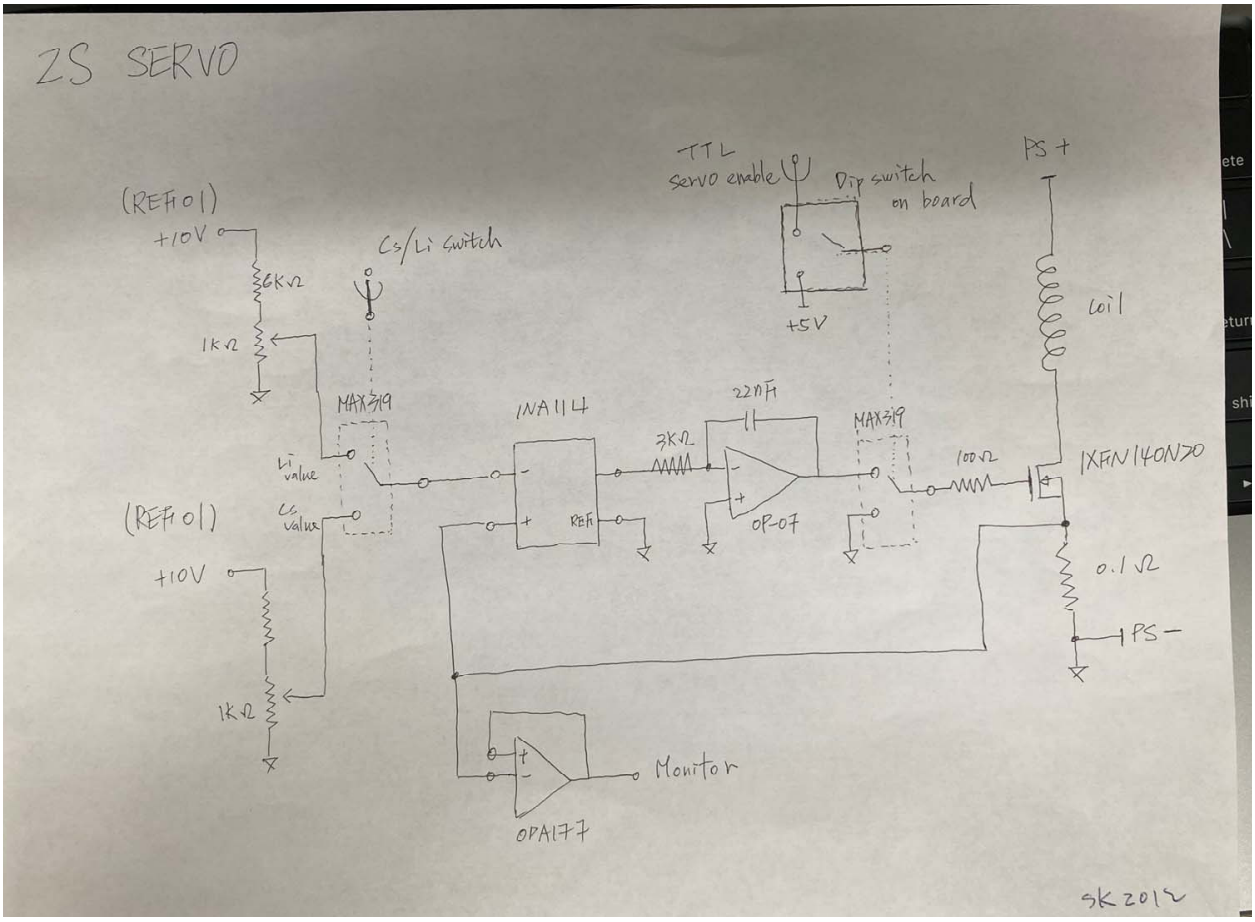

Figure 2.4: Circuit diagram of the Zeeman slower current driver. In the actual setup, there are five copies of identical circuit each controlling one of the 5 coils. This circuit is designed by Dr.Shih-Kuang Tung. Photos taken by author unless otherwise noted.

later.

After passing through the 2D MOT chamber, Li and Cs atoms are slowed down in the Zeeman slower. The Zeeman slower is made from rigid stainless vacuum tube surrounded by 5 coils made with water-cooled hollow core magnetic wires. Out of these 5 coils, one of them serves as a bias coil, in order to cancel the stray magnetic field from the Zeeman slower. The other 4 coils have different current to generate a changing magnetic field such that the Zeeman level are varying as the slowing process go on. The Zeeman slower's current is controlled by a two-mode FET circuit so that it could accommodate both atom species.

After the Zeeman slowing stage, the atoms are slowed down to speed of few meters per

channel	Li mean(mV)	Li spread(mV)	Cs mean(mV)	Cs spread(mV)
1	712	700∼736	45	38∼52
2	676	648∼704	96	88∼104
3	712	696∼736	38	33∼44
4	840	824∼856	3	-5∼10
5	76	50∼84	85	78∼91

Table 2.2: Zeeman slower driver monitor output voltage. These values are obtained after highly time-consuming high-dimensional optimization. The voltage reading might drift as time goes, but will capture the bulk part.

second, close to the limit of Doppler temperature $T_D = \frac{\hbar\Gamma}{2k_B}$. For Cs it is $\sim 120\mu K$ and $\sim 140\mu K$ for Li. Here Γ is the linewidth of the cooling transition. The slowed down atoms travel into main chamber with part of them captured by the magneto-optical-trap (MOT). The MOT loading process starts here. For Cs atom, we have ~ 3 second of loading whereas for Li we load to ~ 10 second. Li needs a longer loading time comes from many reasons: We are a bit in short of 671nm laser power, and Li has larger horizontal velocity as well as lower natural abundance ($< 8\%$ for ^{6}Li).

We further do a compressed MOT process (cMOT) in which both the MOT frequency and magnetic field gradient are ramped, in order to increase the phase space density for later loading process.

The later cooling process differs a bit for the two species. For Li, the hyperfine splitting is 4.4MHz which is even smaller than the line width due state decaying. No convenient subdopper cooling is available near D2 line. (People developed gray molasses cooling scheme later in the days, see Ref. [62] for the working principle and check for Ref. [134] for a convenient plan.) Due to this reason, the Li cMOT is simply followed by a state transfer process and go straight into dipole trap loading process. The state transfer is done by turning on the MOT transition light a bit longer, therefore the Li atom are pumped into the dark state in the lower manifold of the ground state.

For Cs, the cMOT stage is followed by a Cs optical molasses cooling/ polarization gradient cooling /Sisyphus cooling. After which Cs atoms are loaded into a degenerate Raman side

band (dRSC) lattice. The Cs atoms are loaded into an optical lattice, and the vibration quanta are taken away during this cooling process. The dRSC stage lasts for about 30ms. The dRSC is performed at $F = 3$ manifold of the ground state and $F' = 4$ manifold of excited state. For this reason, dRSC requires different laser frequency from the MOT laser and repumper laser. In fact, the repumper and the MOT laser switch roles during dRSC. For a detailed description of the dRSC, Ref. [92] is a good reference.

I would like to end this section by a few bullets point which might help for system health troubleshot.

• Near the 2D MOT chamber, one can use a CCD to check for the situation for atom beams. This is a useful diagnostic when suspecting very early stage system health issue. See Fig. (2.5)

• The connection wire in between the circuit output and the Zeeman coil is done by using very rigid but fragile wire. Be gentle when handling the Zeeman current driver. Besides, due to engineering flaw, the Zeeman slower circuit is very noisy. Yet it doesn't mean its broken.

• dRSC: During dRSC stage, since the MOT laser and repumper laser switches role. The laser locking performance of the 'repumper' is more important. Whether the lock is fast enough, and quality of laser mode matters here. If in future, the experiment has evolved so much that it requires even better Cs number stability, here is one of the place to consider upgrading.

2.3 Ultracold Collision and Feshbach Resonance

This section gives an overview of ultracold collisions. Before diving into the topic, I would like to mention a bit about the mathematic formalism in ultracold collisions. In many quantum mechanics textbooks, the scattering theory is usually presented Born Oppenheimer approximation and partial wave expansion formalism, yet these algebra need to be specified a bit before applying into the problem of ultracold collision. Distinguishing between different

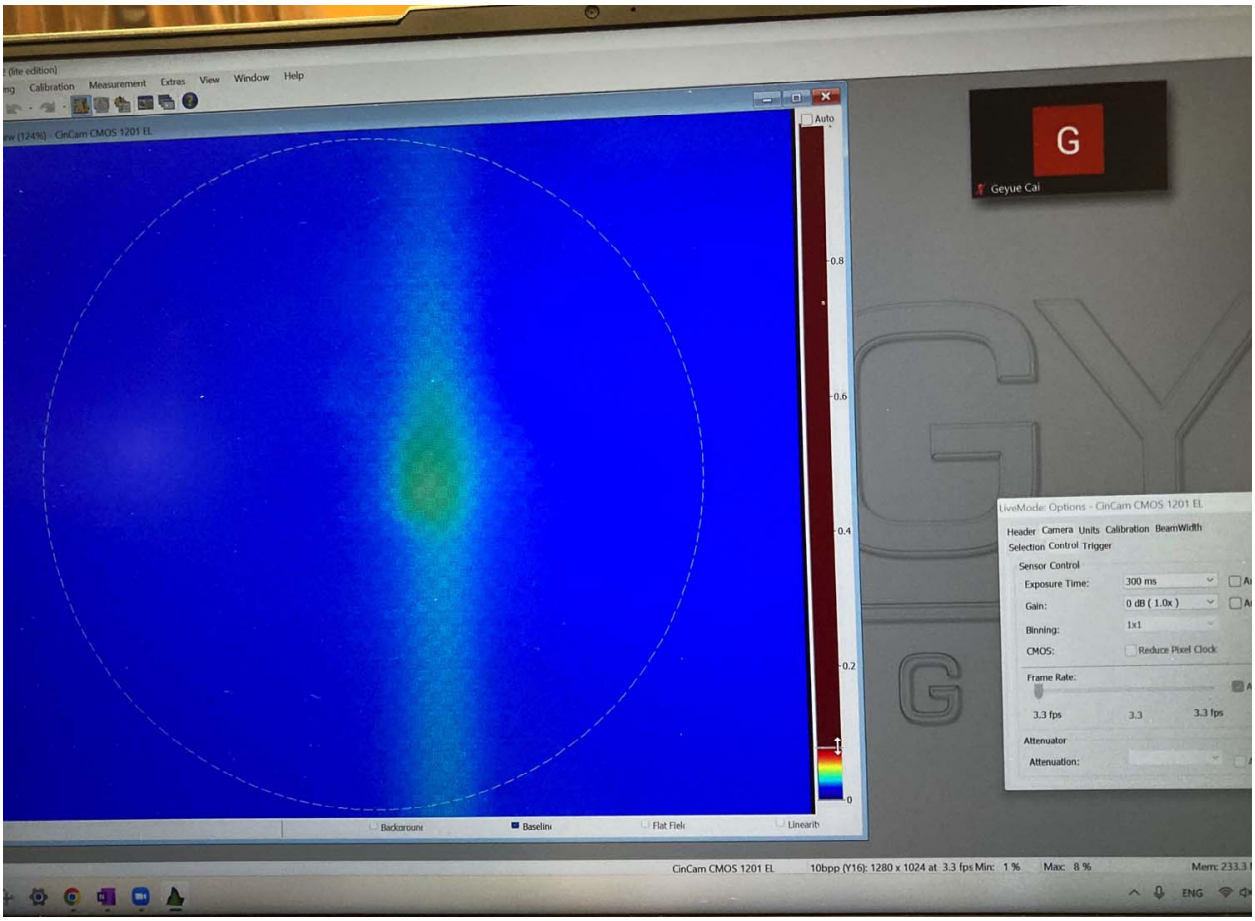

Figure 2.5: Image of fluorescence signal of Cs atom beam. The Cs atom beam coming out of oven is slowed by Zeeman slowing beaming, the scattered fluorescence is captured by a beam profiler. The stronger signal in the middle comes from fluorescence signal of 2D MOT beam. These fluorescence signals requires a longer exposure time to capture.

formalisms can sometimes be challenging. In this section, I would like to introduce this topic in a way which is easiest to understand from my own point. For more in depth investigation of the topic, see Ref. [25].

Start from a traveling particle, its wave function is represented as a plane wave:

$$\varphi = Ae^{ikz} \tag{2.1}$$

When it scatters on another particle with an isotropic potential, the plane wave will be disturbed (Similar to the spirit of static perturbation theory).

$$\varphi = e^{ikz} + f(\theta)\frac{e^{ikr}}{r} \tag{2.2}$$

The second term is induced by the scattering process which behaves as an outgoing wave at far field. For the moment, we will forget about the plane wave focus on solving the second term. Or equivalently, we are asking this question: What is the eigenstate of for two particles with a mutual interaction $V(r)$ In the center of mass coordinate, we have the following Hamiltonian:

$$H = \frac{\hbar^2 k^2}{2m_r} + V(r) \tag{2.3}$$

Where $\hbar$ is the reduced Planck constant, k is the relative momentum, m_r is the reduced mass and $V(r)$ is inter particle potential.

For an isotropic inter particle potential, recall the mathematics when solving a hydrogen atoms. By separation of variable, the wave function φ is expressed as:

$$\varphi = R(r)\Theta(\theta)\Phi(\phi) \tag{2.4}$$

Following this, the problem is reduced to solving the radial function $R(r)$ under the potential

$V(r)$. More specific, we arrive at the so called radial equation:

$$-\frac{\hbar^2}{2m_r}\frac{d^2u}{dr^2}+[V(r)+\frac{\hbar^2}{2m_r}\frac{l(l+1)}{r^2}]u=Eu \tag{2.5}$$

Where $u \equiv rR(r)$, l is the quantized angular momentum in the center of mass frame, $E=\frac{\hbar^2k^2}{2m_r}$ is the eigen-energy of the system. The term $\sim \frac{\hbar^2}{2m_r}\frac{l(l+1)}{r^2}$ is the centrifugal potential barrier. At very large separation, $kr \gg 1$, 2.5 is in radiation zone in the language of optics. When we assume the potential is localized, 2.5 reads as:

$$-\frac{d^2u}{dr^2}+\frac{l(l+1)}{r^2}u=k^2u \tag{2.6}$$

The general solution to 2.7 is linear combination of spherical Bessel functions. While considering outgoing or incoming scattering process, we use spherical Hankel function to represent their solutions. For a majority of ultracold experiments which the physics of interest happens at temperatures $< \mu K$, therefore only $l=0$ case is considered. This greatly simplified the following algebra.

On the other hand, angular momentum l determines the symmetry/anti-symmetry property of the radial equation. Which naturally put restriction on the species of collisions. Therefore, for our experiment we mostly consider Cs-Cs interaction and Li-Cs interaction, and only worry about Li-Li collision when Fermi gases have more than one component.

For most ultracold scattering processes, the potential $V(r)$ originates from Van der Waals interactions in between atoms. This made $V(r)$ a strong and short range potential. The effective range of these potential ranges from few tens of a_0 to less than few hundreds of a_0. Given $l=0$ and $V(r)$ is short range, we return to the simplest case.:

$$-\frac{d^2u}{dr^2}=k^2u \tag{2.7}$$

The solution is simply a sinusoidal function

$$\varphi = A\sin(kr) + B\cos(kr) \tag{2.8}$$

In ultracold experiment, the temperature is as low as few tens of nK. In this limiting case, we would imagine the solution eventually looks like a linear slope start from somewhere near $r = 0$. Therefore, the entire wave function 2.2 reads as

$$\varphi = 1 - \frac{a}{r} \tag{2.9}$$

. Equation 2.9 suggests that the function looks like the wave function bumped at $r = a$, looks like the scattered sinusoidal wave function picks up a phase shift δ. Here the value a is called scattering length, usually represents in unit of Bohr radius a_0. Or equivalently,

$$\tan\,\delta = -ka \tag{2.10}$$

The 2.10 is the core of ultracold scattering process.

In the meanwhile, the short range strong potential $V(r)$ is replaced by a pseudo potential for convenience.

$$V = g\delta(r) \equiv \frac{2\pi\hbar^2 a}{m_r}\delta(r) \quad , \quad \equiv \frac{4\pi\hbar^2 a}{m}\delta(r) \quad \text{(identical particles)} \tag{2.11}$$

Where g denotes the interaction strength.

All the above algebra shows that the ultracold collision could be simply replaced by a short range delta function. Yet it is the tunability of these interactions make cold atom experiment unique. Now consider two atoms colliding in the continuum, yet in a real world the Van der Waals interaction naturally induces many underlying bound states with different eigen-energies. The incoming continuum state is referred as entrance channel (open channel)

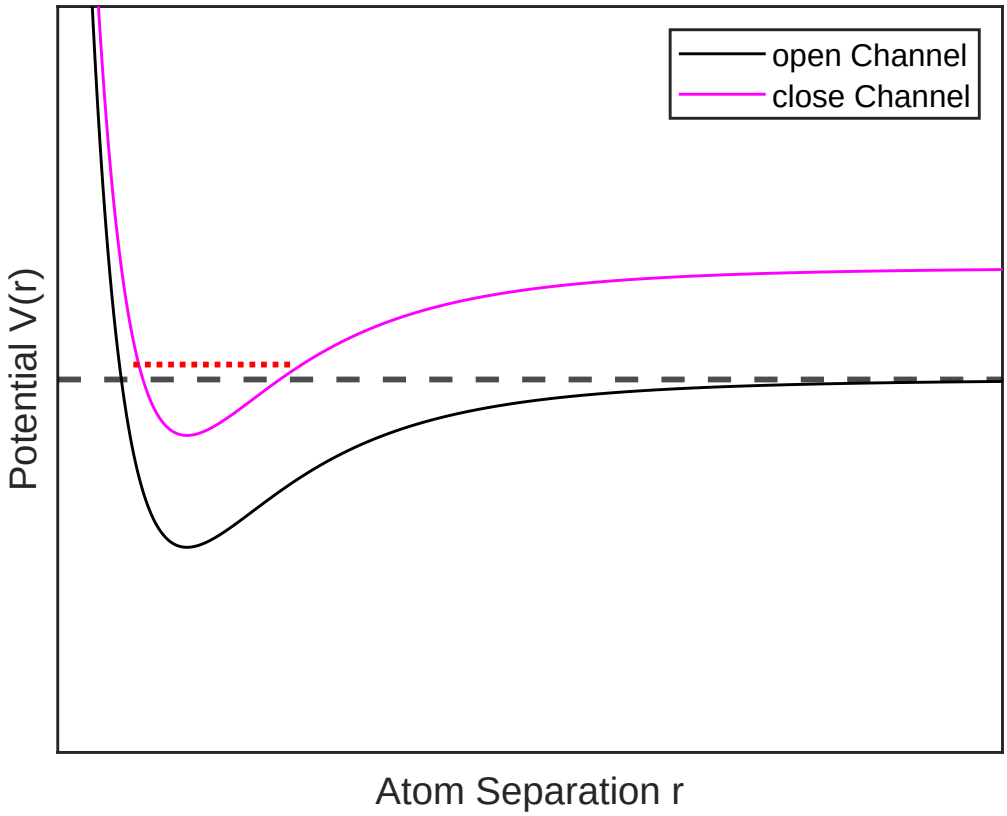

Figure 2.6: Illustration of two channel model, the red dotted line denotes the bond state in the closed channel. Sometimes people need to consider multiple channels in their calculation to obtain the correct scattering properties.

whereas the later is denoted as closed channel.

When the eigen energy of the bond state is close to continuum, one could imagine that the wave function in two channels are going to have strong overlap, leading to the coupling between channels. Because the bond state and continuum state usually have different property(say, magnetic dipole moment). The energy of the bond state usually could be tuned by external conditions, such as magnetic field or laser light. This mechanism gives rise to resonant feature while the bond state is tuned near continuum, granting the tunability of the interaction between atoms. These resonances are named as Fano-Feshbach resonance (or Feshbach resonance for short). A resonance tuned by a magnetic field is called a magnetic Feshbach resonance, whereas one induced by a laser is called an optical Feshbach resonance, see Ref. [74] for example.

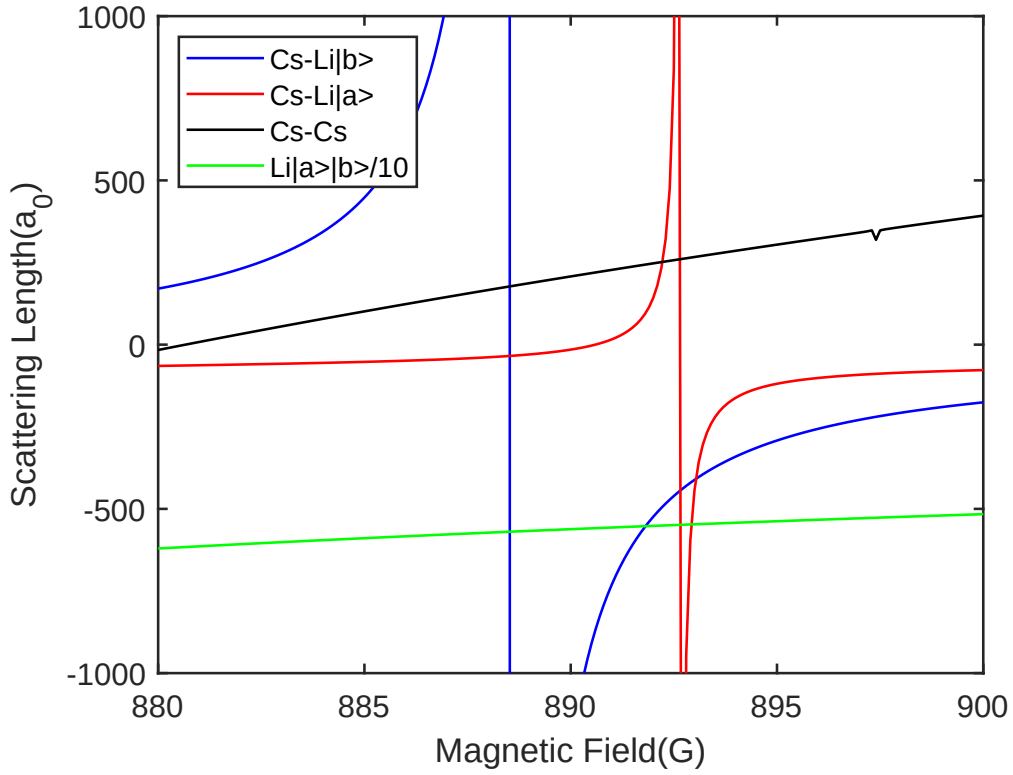

Figure 2.7: Scattering properties for Cs and two lowest ground state Li in commonly used magnetic field range. Note that the Li|a>-Li|b> scattering is scaled down by a magnitude for displaying on the figure.

Our experiment uses the lowest ground state of Cs $|F = 3, m_F = 3 >$ and the two lowest ground state of Li $|F = 1/2, m_F = 1/2 >, |F = 1/2, m_F = -1/2 >$, conventionally denoted as Li-|a> and Li-|b>. The interaction between inter and intra species of them are of not exception, 2.7 shows the scattering properties of our commonly used atoms at our usual operating range of magnetic field. One last point to mention is that: for a stable quantum degenerate Bose-Fermi mixture, we requires a_{BB} to be mildly repulsive whereas we want some tunability in between Li and Cs. Therefore, the combination of Li|a> and Cs is a perfect choice, which featuring a 2G wide narrow Feshbach resonance.

2.4 Cooling in Dipole Trap

After the early laser cooling state, further evaporative cooling in a dipole trap is necessary to reach lower temperatures. This requires loading atom into far-off resonance laser beam. When atoms interact with light away from resonance, the scattering rate decays as $1/\Delta^2$, where Δ is the detuning. In the meanwhile the trapping potential drops as $1/\Delta$. Therefore, a high-power and far-off-resonance laser is ideal for dipole trapping. In many cases, doped fiber laser near 1064nm is a perfect fit for such purpose. In our system, we have 3 major paths for optical trap:

• BFL: Short for Big fiber laser, which comes from a 200W 1064nm multiple frequency single mode laser from IPG. It passes AOM and then splits into two 80W beam, forming a crossed dipole trap for Li atom trapping. The two arms travel in parallel before they being focused by a 2-inch lens on a translational stage. The translation stage is capable of moving the focus of dipole trap as far as 2cm, making it convenient for trap loading and cooling scheme which is otherwise almost impossible for Li-Cs experiment. The reason we have to use a dipole trap with power as high as 200W is the lack of sub-Doppler cooling method for Li. Even so, the beam has to be focused down to reach deep enough trap depth therefore reducing its capture volume from Li cMOT. Here is some number to give a sense of it: After

cMOT we have 6-11 million Li atoms and usually 300k is loaded into BFL, as low as $2 \sim 5\%$.

• oTOP trap: Oscillating Time-average Optical dipole trap for Cs trapping. The laser light comes from a single frequency single mode 30W 1064nm laser from Precilaser. This trap is almost an elliptical sheet: At the focus, it is $76\mu m$(diameter) in vertical direction with a horizontal spread of $1086\mu m$(diameter). This trap has a long beam path with an AOM at a position far away from atom position. Since the driving frequency of AOM could affect its diffraction angle, we control the vertical position of atom by tuning the AOM driving frequency. Also, the AOM frequency is modulated at 100kHz during loading from Cs cloud after RSC cooling. Such modulating scheme greatly increase the capture volume and increase the loading efficiency. Right after RSC cooling, we have $15 \sim 27$M Cs atoms and we usually load $3.5 \sim 5$M atoms into oTOP trap. It seems that, due to the fact the oTOP can load so many atoms that there is some additional high density losing process. This extra losing process actually helps us suppress down number instability in early stage laser cooling, greatly increase the robustness of Cs number.

• Dual color trap: Laser light from a 780nm diode laser and part of the 1064nm laser from the Precilaser is combined and sent into the same fiber. This creates a dual color trap for final stage sympathetic cooling. The 780nm increases trapping strength for Li while weakening trapping potential for Cs. At atom position, the foci of these two beams do not overlap. My guess for the reason of trap center separation is: The fiber end is cleaved with a small angle with respect of light propagation direction (for preventing back reflection). Therefore, due to difference in refraction index, the 780nm and 1064nm beams propagates into free space with a slight difference in angle. Both the 780nm and 1064nm have beam diameters of $60\mu m$.

Now with the dipole trap setup explained, summarize the entire sequence in 2.8

I would like to end this section by some troubleshot suggestions. • Given the complexity of experimental sequence, it is always good to calm down and check which stage is actually

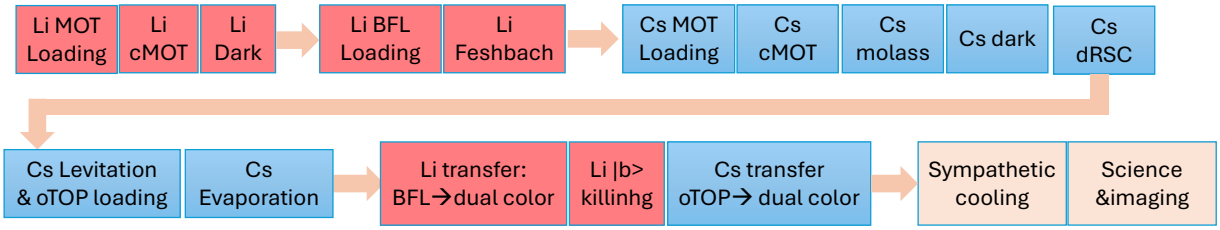

Figure 2.8: A summary of the entire experimental sequence towards dual quantum degeneracy. Dual MOTs scheme doesn't work for Li and Cs. The Li MOT and trap loading happens first since Li has a much simpler Feshbach resonance feature. After Li is loaded into BFL, the BFL trap is moved far away during Cs early stage cooling. The reason being the large dipole moment while Cs in excited $^2P_{3/2}$ state hurts Li number. After Cs dRSC, a levitation gradient is turned on for oTOP loading. After Cs trap loading, the oTOP is moved above the loading position. The experiment is then ramped to high magnetic field around 890G. The Li is first transfer into dual color trap followed by a resonant pulse blowing away the unwanted species(usually), the Cs is then transferred into dual trap with $a_{BF} \sim 0a_0$. After sympathetic cooling, the science and detection stages take place.

casing problem. Especially don't conclude that the problem being early laser cooling stage, since they are more unstable but sometimes not being the actual problem. Some common sanity check includes: Turning off one species, imaging frequency, dipole trap intensity and noise, turning off unrelated dipole trap etc.

- BFL: Early stage loading into BFL: The position overlap could be tuned by MOT frequency and field gradient, the trap depth is more related to BFL AOM as shown Fig. (2.9). For the BFL to dual color trap transfer stage, trap position overlap and trap size match is more important. It is wise to check these two things before proceeding and tweak them:

(a) Check trapped Li atoms position before and right after trap transfer (cloud center changes as intensity varies).

(b) Do a short time of flight for the end of BFL stage, compare the Li cloud size, aspect ratio and numbers with record. Problems in trap overlap could be fixed by the position of translational stage parameter and the pair the mirrors with micrometer reading on them (most of time you need to move a few degree or even less one degree to fix the problem). On the other hand, if BFL dipole trap crossing is bad, you will observe unstable and low

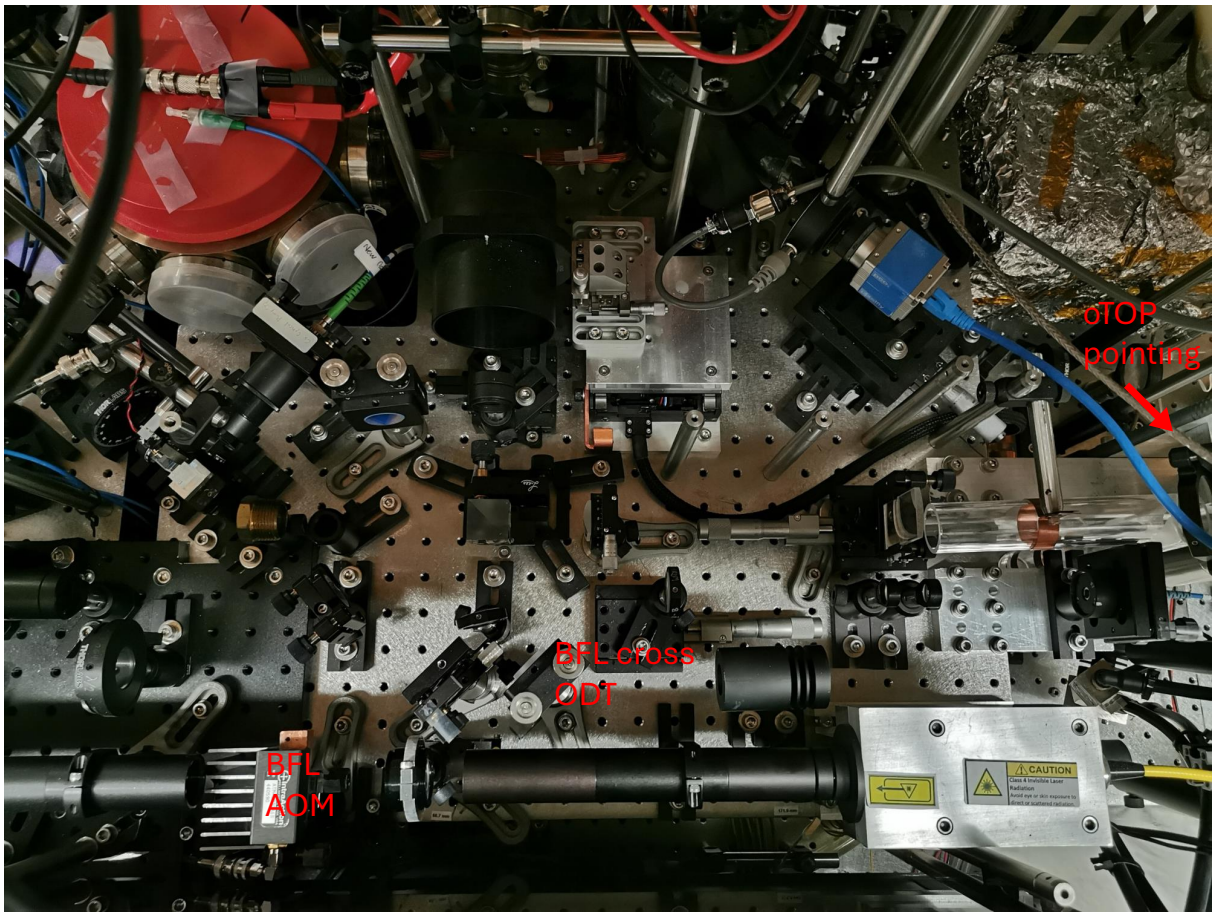

Figure 2.9: Picture of dipole trap layout. The dual color trap and oTOP trap are combined with a PBS and travel through the hole of the 2 inch lens. The two arms of the BFL trap travel in parallel and get focused by the 2 inch lens on the translational stage. The mirror mount labelled 'BFL cross trap' is the one responsible for overlapping of the two arms inside the chamber. On the most right it is the nob for oTOP pointing.

number, as well as an unstable trap aspect ratio from day to day, and you will find the tweak BFL AOM has strong effect on the BFL trap (which shouldn't be the case but could be true when poor crossing happens). And as always, BFL is really high power, so try your best avoid dust pollution and use IR viewer to ensure laser safety.

• oTOP: Problem of oTOP loading from Cs dRSC cloud is usually related to early laser cooling, we focus on trap transfer from oTOP to dual color trap. Since the oTOP trap is highly elliptical, horizontal overlap with dual color trap is not an issue for most of the time. The vertical overlap could be adjusted by oTOP AOM's carrier driving frequency. However, if a problem does happen, Fig. (2.10) shows the place for troubleshooting.

• Species mixing stage is the most tricky part. Cs in oTOP is moving down and trying to make a transfer into dual color trap. In the meanwhile, the 780nm power in dual color trap is ramped down to mitigate its anti-trapping effect on Cs yet in the meanwhile, the combined potential in dual color should be strong enough to hold Li. Troubleshot this part of the sequence could be complicated.

• Fiber coupling: As a waveguide, the incoming beam wavelength, the refraction index of cladding and core of fiber, as well as the fiber core radius determine mode field radius and V-number in a non-trivial way. Sometimes it is hard to get the all the parameters you need, so I would recommend the following: Put on a collimated package on fiber and measure the out coming beam radius D. Since focal length f satifies $f/D = constant$ for given wavelength. You will quickly know what's the best combination of incoming beam radius and aspheric focal length. Beside that, also pay attention to beam profile, for example, transmitting through out rim of AOM aperture could distort the beam. (PS:I found these subtle knowledge not often seen, yet these are important tricks to achieve coupling efficiency above 50%.)

• Li |a> |b> ratio: For many years the Li |a> species is always a bit high in population, ranging from 60% to 70%. Yet neither me nor Krutik Patel have verified the correct nob to

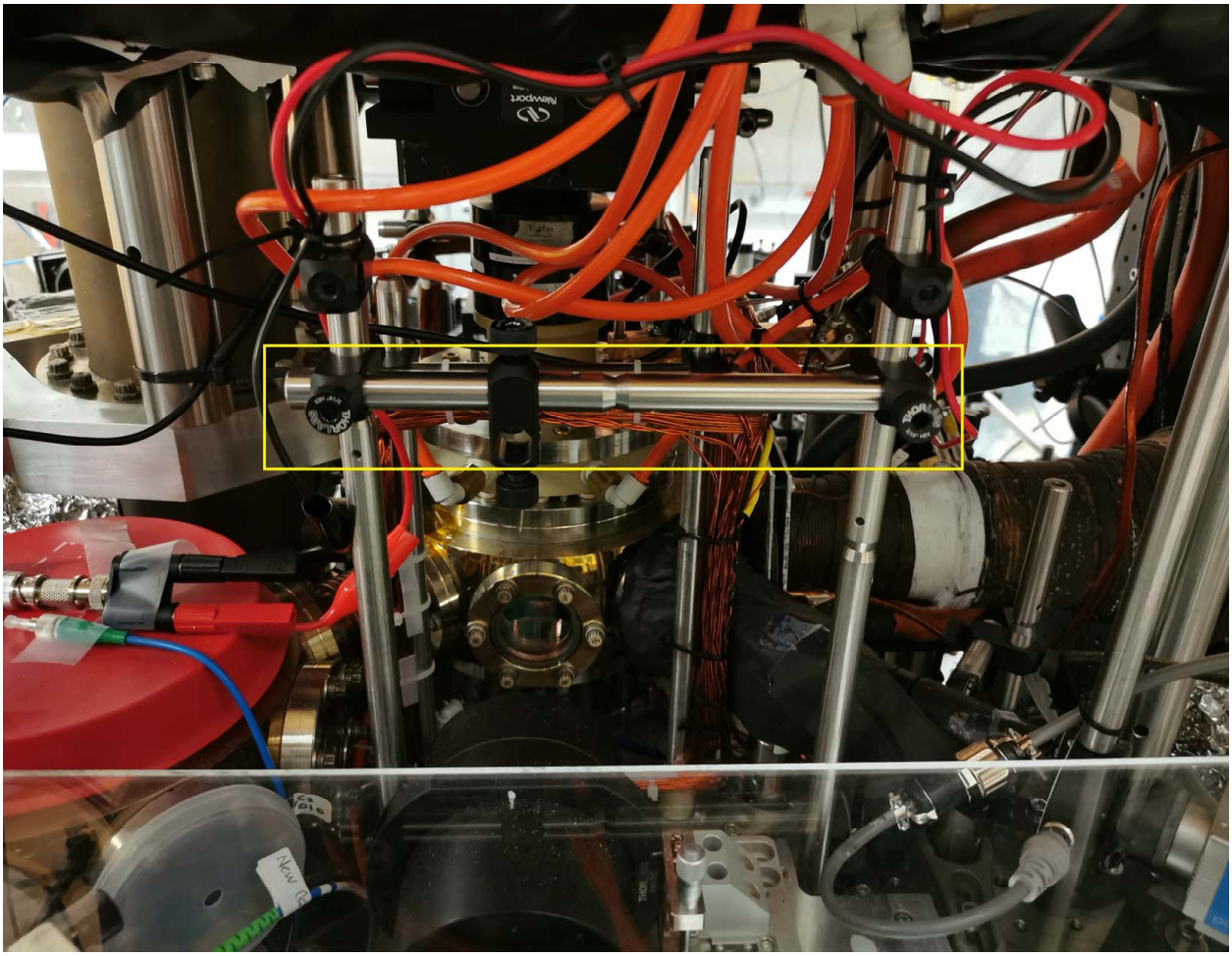

Figure 2.10: Setup for dipole trapping Engineering. The frame labeled is in yellow is for constructing and diagnosing oTOP and dual color dipole trap problem. By placing a half wave plate and a **plate** polarization beam splitter. You can reflect the dipole beam upwards and observe their behavior right before they transmit into vacuum chamber. It is a good idea to tweak the mount of plate beam splitter so the beam travel upwards parallel to gravity. Using a beam profiler makes it possible to compare the beam waist position and its overlap.

tune the population label. I would still be curious of what's the answer.

2.5 Magnetic Field Control

This section will introduce the generation and control of magnetic field. I will skip the part nicely written by Dr.Jacob Johansen and focus on explaining the working principle of the main coil control circuit as well as the 'Smart Shim Jump' function we developed in 2023.

2.5.1 Bitter Coil and Its control

The Bitter coil (also called main coil or Feshbach coil) is one of the core parts of the experiments. The very basic working principle in a sentence is: Taking computer input to controlled a set of field effect transistors (FETs) with a PID circuit. These circuits were designed in the very early years of LiCs project and were not very well documented. I hope they works well in future so you don't have to read the rest of this section.

Fig. (2.12) demonstrates the working principle of the entire setup. For the lower coil path, the current goes though current and then a bank of high current FETs, after which it returns back to power supply. For upper coil path, since it has a built in HH or AH configuration, the 4 sets of FETs will determine which path the current will flow through. For the upper coil, the current flows in AH configuration mostly during MOT loading/ cMOT stage as these stages requires mostly magnetic field gradient. For this reason, the AH path does not need a high current rating cable as you will see.

The upper left corner of Fig. (2.12) is where the computer command starts.

• Ch5.20/Ch5.18: Control the allowed current output from power supply, as what people do to a regular power supply. The circuit is controlled by feedback on FETs, therefore, most of the time these two channels are only for safety measure during some stage. The fact that they directly come out of noisy computer output into power supply imply this point as well.

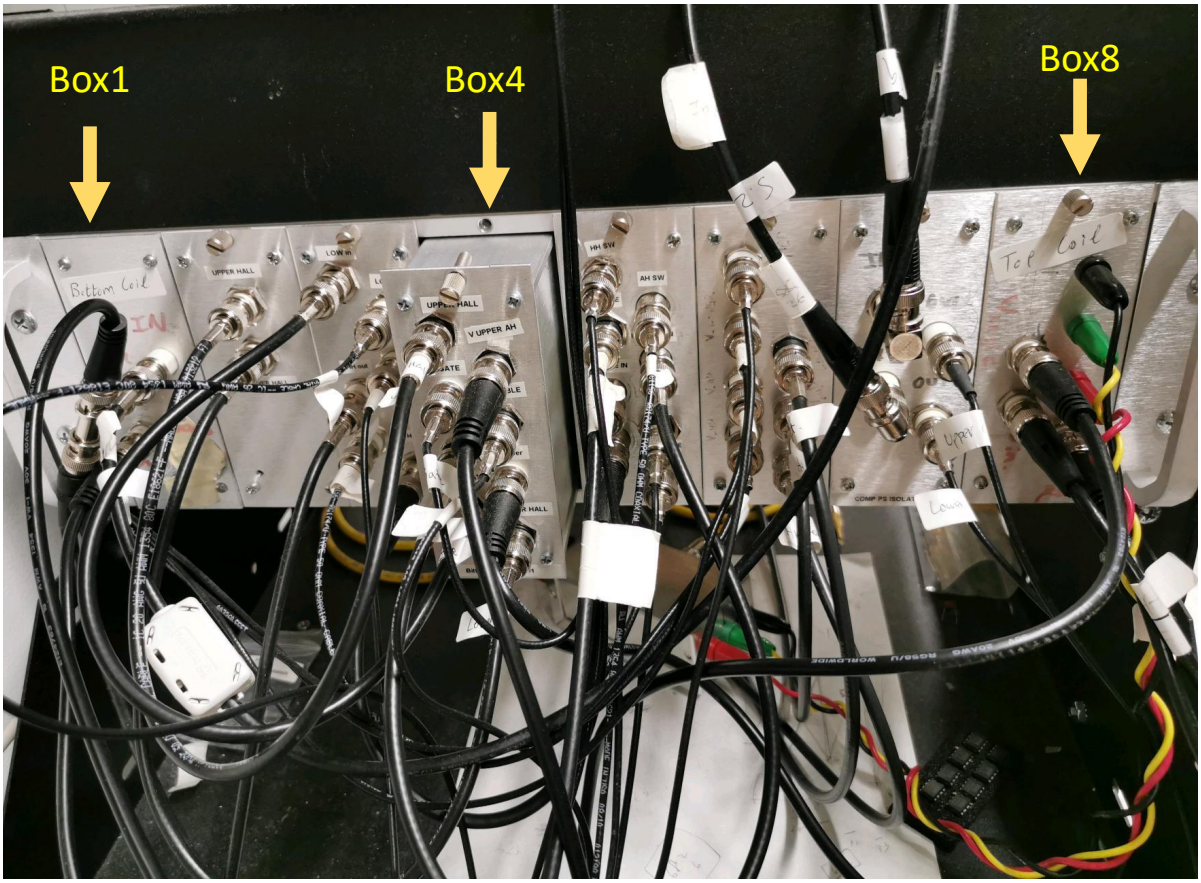

Figure 2.11: The bank of electronic boxes for Bitter coil. The boxes are labeled from left to right.

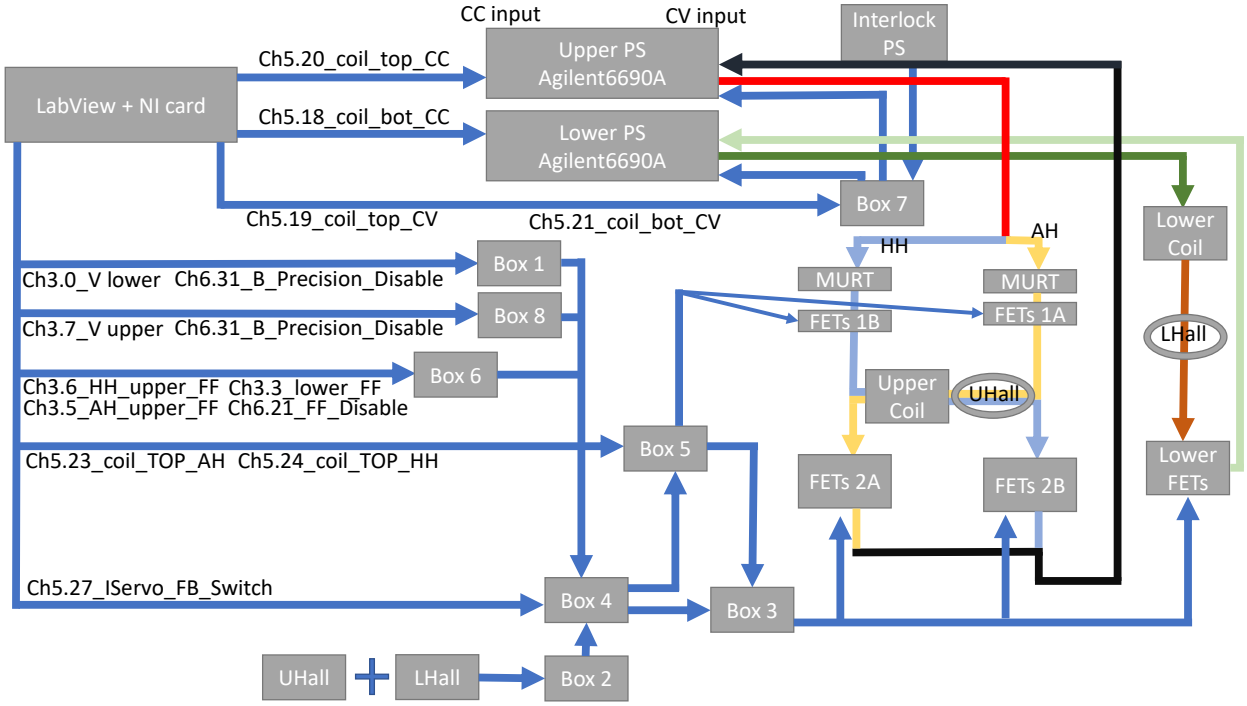

Figure 2.12: Structure of the Bitter coil circuit. The current is measured through the Hall sensor and compare with computer command value to generate the error signal. The control of such high current is achieved by FETs. Such design features a fast switch performance whereas sometims it would be a bit annoying to tune the lock. See chart 2.3 for Abbreviations.

PS	power supply
FF	feed forward
CV	constant voltage
CC	constant current
HH	Helmholtz
AH	Field effect transistor(s)
FET(s)	Anti-Helmholtz
MURT	MURT40040R bridge diode
UHall	Upper Hall sensor(ultrastab)
LHall	Lower Hall sensor(ultrastab)

Table 2.3: Abbrevations in Fig. (2.12)

• Ch5.19/Ch5.21: Control output voltage of power supply. For the purpose of having a stable current feedback, these computer signals are filtered by INA114 op-amp.

• Ch3.0/Ch3.7: Control for the lower and upper coil current. Note this is not the same as Ch3.0/Ch3.7 in the LabVIEW program, since these two channels are two of these special channels followed by some HH/AH configuration algorithm.

• Ch6.31 B precision switch: This is an digital channel which enable the high precision mode at higher current. Since we are pursuing part per million field stability, the National Instrument card does not have enough digits. Therefore we need an offset + a narrowed tuning range to realize current fine tuning. The an experimental sequence involving low/high resolution mode change, B precision switch is turned when the HH value in LabVIEW is same before and after the change, so that a smoother transition could be obtained. Whereas in the meanwhile, the AH value is quenched to new value at that moment.

• Ch3.6 Ch3.3 Ch3.5 Ch6.21: These four channels are responsible for current feed forward purpose. It help a faster reaching of target current with a digital enable switch.

• Ch5.23 Ch5.24: Digital switch for control the AH/HH configuration of the upper coil. Remember to be cautious and never turns on a short circuit. Keep at least one of them off all the time. (Also with some time gap in between a mode switching)

• Ch5.27 IServo FB switch: Current servo feedback switch. It controls if the PID circuit

is enabled or not in box 4. The servo turns off scenarios such as a fast turning on or off of the current. Again due to the FETs has a varying V-I slope depending on applied voltage and current, sometimes it is a better idea to listen to feed forward command instead of causing ringing in the locking circuit.

Understanding the function of different channels, time to explain other components:

• UHall/LHall: Upper and lower Hall sensor, providing a high resolution, out of loop measurement of the current.

• Box 1/8: Receive and clean the computer command signal, depending on whether precision mode is enabled, sending a certain signal to box 4.

• Box 2: Powering and receiving the signal from the upper/lower Hall sensors and send to box 4.

• Box 4: 'Brain' of the coil feedback circuit. The error signal is generated in this box. It takes the computer AH/HH signal processed by box 1 and box 8, as well as the measurement from box 2, and generating the error signal. There are two BNC connectors inside the box which provide a reading for error signal. It also takes in the feed forward signal from box 6. ON the top of that, it takes on a digital command from computer to decide if feedback loop should be on or not. The error signal is combined with feed forward signal and send to next stage. The error signal for lower coil control, which does not need to worry about AH/HH configuration, is sent to box 3 directly. The error signal for up coil, however, need to be processed by box 5 depending on the AH/HH configuration, and then sent to box 3 for output.

• Box 5: This box takes digital input signals from system. It will operate as a digital gate on the FETs1B and FETs1A. The analog signal from box 4 is taken in as well, and send to box 3. The digital command here will also determine if an output is needed from box 3 to the analog FETs.

• Box 3: It is basically a driver for FETs. The reason we have an extra stage aside from

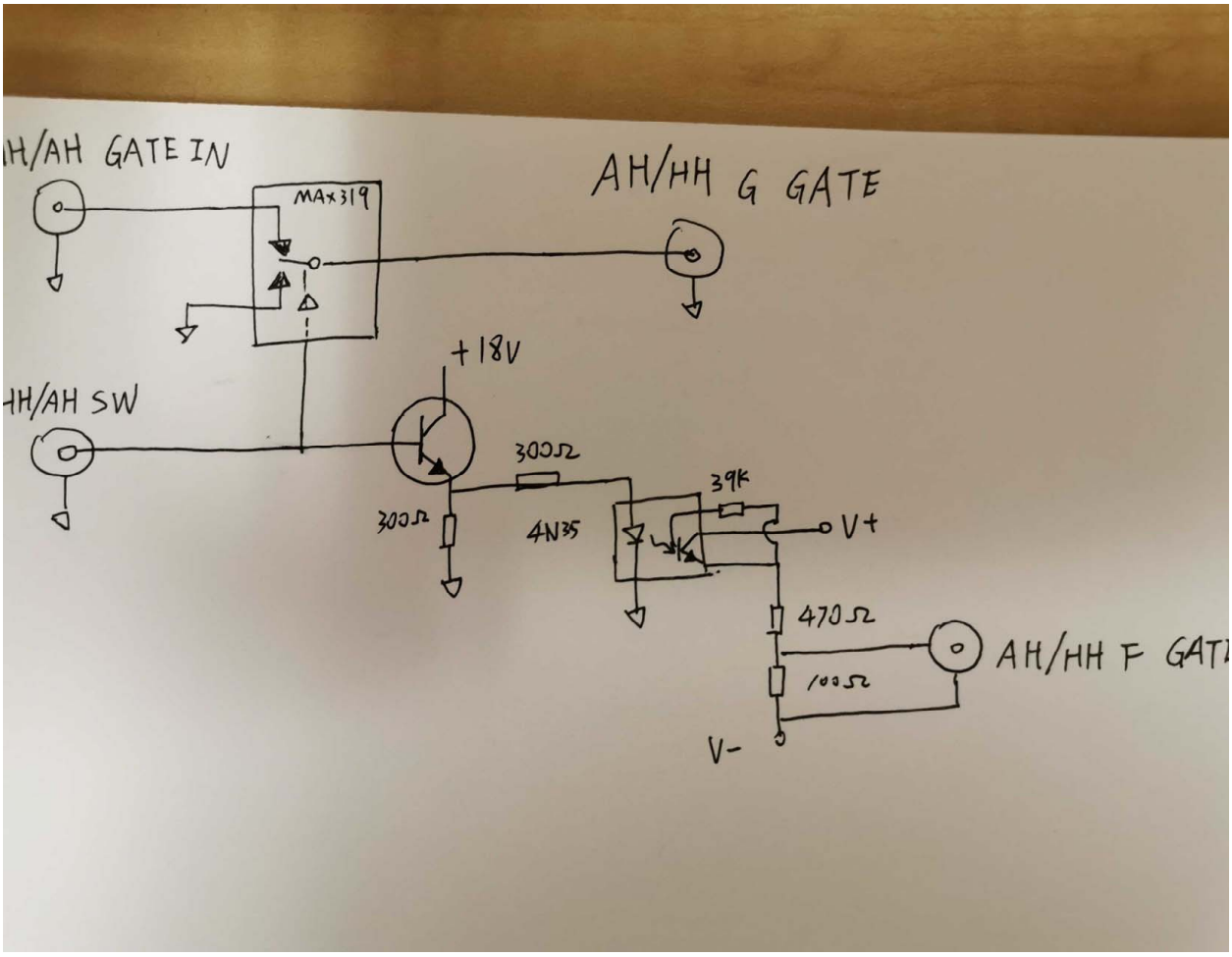

Figure 2.13: Schematic of circuit for box 5. The HH/AH GATE IN has a specific ground which will goes to box 3 for later (the lower FETs group). However, the output to the digital FETs are isolated from the rest of the circuit with a 4N35 optocoupler chip.

the box 4 is that: the current output from op-amp is insufficient to drive the FETs fast enough.

• Box 7: This box has a relative simple function, it takes in CV voltage with INA114, and combined with different interlock signal(a manual interlock for daily use and a cooling water flow interlock)

• FETs: The lower three sets of FETs 'FETs 2A', 'FETs 2B' and 'Lower FETs' are designed analog signal control. Where as the upper two sets of FETs 'FETs 1B' and 'FETs 1A' are for digital control on the current.

One issue worth a specific attention is the grounding configuration of the entire setup: As already indicated by Fig. (2.12), the magnitude of the current is control via the lower three groups of FETs. For the best performance, the grounding point should be close to these spot as much as possible. In fact, the ground of these high current path are done via the tiny grounding traces in these electronic boxes (which is not that smart). On the other hand, we want only one ground for the entire high power circuits, this is why there are multiple power supplies in the controlling electronic circuits. Box 7 has optocoupler inside to isolate the ground of circuit with the ground of the CV input on the Agilent power supply. Likewise, the digital FETs group also has an optocoupler to isolate the circuit ground with the high power loop. The power supply for box 7 and box 5 are also ungrounded, this is done with this purpose. Another often discussed question is: the Agilent power supply has a grounding option on its back, shall we ground it? The answer is no. This is not only due to the reason that adding this extra ground with leads to worse current stability, but also having two grounds in the circuit will causing an unwanted ground loop with very large current flowing through those tiny grounding traces of the controlling circuits. The high current power supply is supposed to operate with floating configuration. This whole circuit works because it has one ground, yet the manner in which the grounding is implemented is not the smartest way given how fragile this grounding option is under high current.

Again, I would like to end this section by few miscellaneous:

(A) As mentioned many times, the FETs do not has a U-I curve as good as an op-amp, sometimes you will need to tune the CV value to optimize the performance of the current trace. If CV is too low, usually the current trace will behave as a slow lock whereas it will ring when CV value is too high. (Sometimes you will hear an acoustic noise).

(B) As mentioned above, since the high current in Bitter coil is grounded via the tiny ground traces in these electronics boxes, according to Lenz's law there could be really high transient current go through those traces when a high current in Bitter coil is quickly switched off.

This is the reason we experienced Bitter coil electronic damage in 2023.

(C) Our current version of Bitter coil relies on a brass current carry screw to conduct high current, which is no longer a good design when high resolution imaging system is integrated. As times goes, the surface in between screw and the underneath cooper block might develop a big surface resistance, causing unwanted heating. In improve the surface resistance, use a cotton stick with methanol to clean the surface inside the Bitter coil, to remove the dirt inside. After this, use acetic acid cotton to clean the surface underneath to remove oxidation cooper layer. This step should quickly followed by another round of methanol cotton stick cleaning to remove the residue acetic acid. This trick usually will bring down the surface resistance around $0.1m\Omega$. Henry Ando and Leon Gold have developed a new generation of Bitter coil, which is designed to solve those problems and make them more compatible with the requirement of high resolution imaging.

2.5.2 Fast field jump

Interesting physics evolves quickly in experiments near the interspecies Feshbach resonance. We have developed a generic way to achieve fast magnetic field switching. Implemented with this method, our system is able to switch magnetic field within 1ms with less than 10mG of swing for any magnetic field switch less than 0.5G.

On our experiment, the shim coil driver itself it fast enough, however the eddy current from nearby metal and Bitter coil greatly slows down the process. Besides, the Bitter coil is actively locked therefore it will generate eddy current which is different from usual eddy current behavior. Though along the gravity direction, the shim coil switching speed is boosted by pre-emphesis circuits, the magnetic field requires at 5ms to stabilize. For this reason, we need extra algorithm from LabVIEW control to optimize it. The two key relevant ideas are inverse Laplace transform and Gaussain filter transformation. In our practice, the Laplace transform will give the major part correct, and combing with the latter will further

improve the magnetic field trajectory.

I will first introduce inverse Laplace transform. Given a step function in the $h(t)$, the change in magnetic field will change according to the response function $r(t)$:

$$b(t) = \int_0^t r(\tau)h(t-\tau)d\tau \tag{2.12}$$

Or more conveniently, in Laplace transformed view it reads:

$$B(s) = R(s)H(s) \tag{2.13}$$

Where $B(s)$ $R(s)$ $H(s)$ are Laplace transforms the function $b(t)$ $r(t)$ $h(t)$ in time domain.

Following these, one would realize that once the inverse Laplace transform of the function is known, an almost step function in magnetic field can be realized. Especially, for induced magnetic field from eddy current, it usually behaves as an exponential decay function $e^{-\alpha th}h(t)$, whose Laplace transform is simply $1/s+\alpha$. This is why the pre-emphesis circuit, which is essentially why a RC circuit is able to speed up the field response with correct parameters. If the major causes of magnetic field slowing down comes from passive elements like eddy current, then with multiple RC circuits, the magnetic field response could be greatly improved. In our experiment, the actively current locking circuit on the Bitter coil makes it complicated. Further more, it should be noted that unlike Fourier transfer, the transform kernel of Laplace function e^{-st} is a redundant basis. In actual practice, people approximate the true Laplace transform function in the form of:

$$\frac{a_0 + a_1 s + ... + a_n s^n}{b_0 + b_1 s + ... + b_n s^n + b_{n+1} s^{n+1}} \tag{2.14}$$

The polynomial in the denominator is at least one order higher than the numerator and most of the time, due to numerical stability consideration, they won't be high order polynomials.

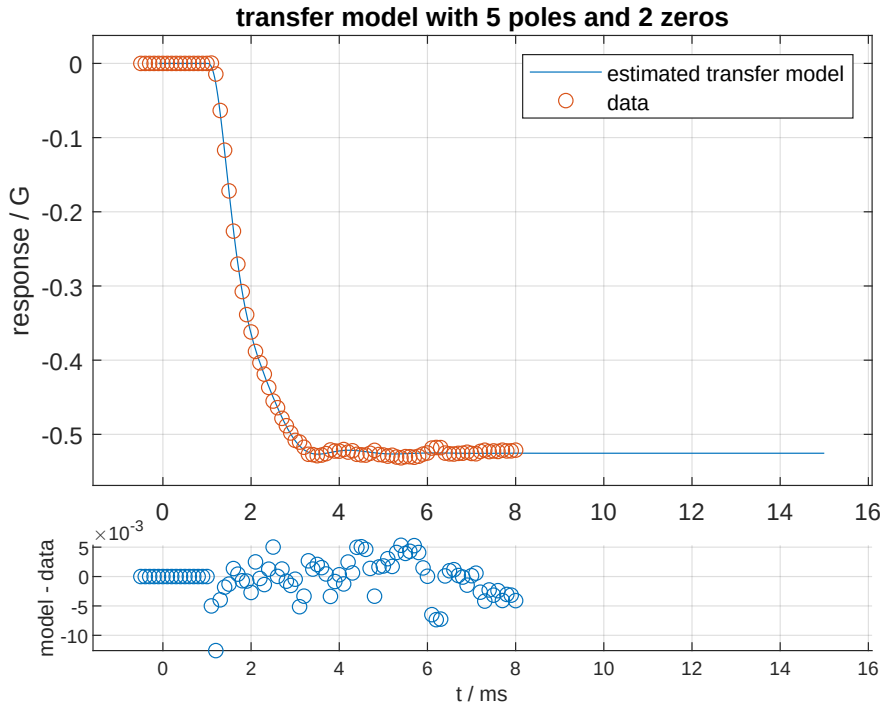

Figure 2.14: Laplace transforms of field response. The model contains 2 zeros and 5 poles. The lower panel shows the deviation in between the model and data. This model is built from Michael Rautenberg.

Fig. (2.15) shows the optimized magnetic field jump. The magnetic field trace shows that magnetic field jump is as fast as within $1ms$. However, it should be noticed that magnetic field oscillates around the target in a irregular way. This is from the active current lock of Bitter coil, whose time scale is on the order of $\sim 10ms$. For further improvement, we apply the Gaussain filter method.

The reason why inverse Laplace transform method create ripples in time domain is that usually those signal processing method generate unwanted side band in frequency domain. In the field of signal processing, many types of moving averaging filters is used to mitigate this issue. The idea is: If the signal output, instead of being the raw signal, is an average of signal in a nearby time interval, then the entire signal will be much smoother. A Gaussian filter is one example, which perform a weighted average of signal in a chosen time interval. Gaussian filter features a smooth cutoff in frequency domain, has a balanced performance

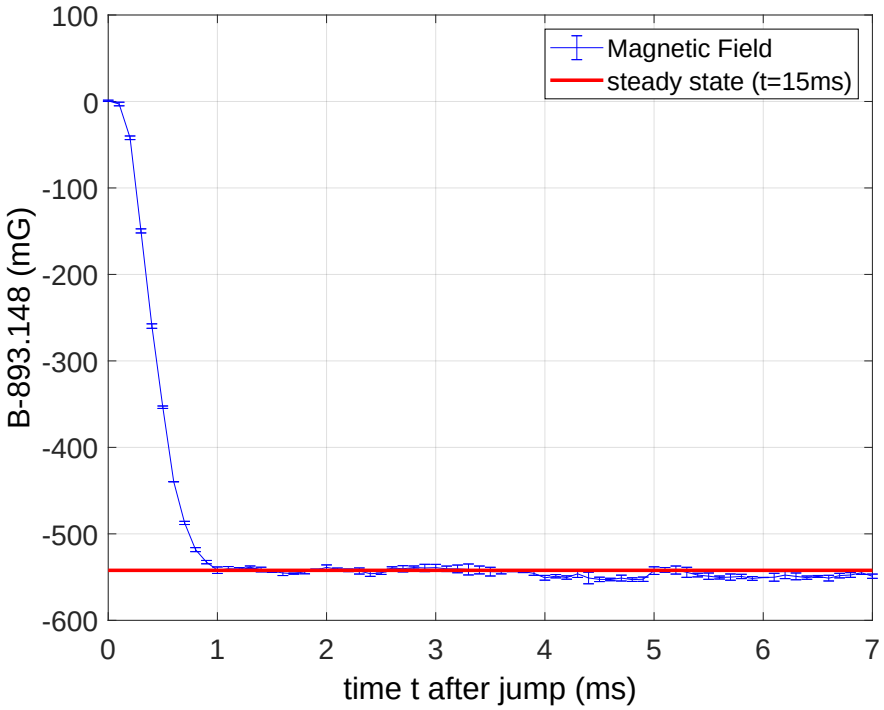

Figure 2.15: Optimized magnetic field jump, after applying the inverse Laplace transfer in LabVIEW output. The field deviation after field reaching target need to be further removed by Gaussian filter method.

in suppressing ripples without hurting the response speed of the system. For a more generic and detailed knowledge, I highly recommend chapter 15 of this book [140].

Atoms never cheat and of course, you can't cheat them by averaging data. What you need to do is introducing a correction signal in the computer output. This value of the signal, is proportional to a Gaussian average deviation data in a time interval, with some delay.

$$V(t_0) = -\alpha \sum_{i=-N}^{N} \delta B(t_0 + t_D + i\Delta t) \cdot e^{-(i\Delta t/\sqrt{2}\sigma_t)^2} \tag{2.15}$$

α is the proportional constant determined by the correspondence between signal and magnetic field, t_D is the delay time of the system, and τ is the time constant of the Gaussian filter. All these quantity could be estimated or measured by introducing a 'blip' in input signal. For our system, the delay is 0.1ms, rise time $t_{rise} = 0.9ms$ corresponding to a 3dB bandwidth of 250Hz. The Gaussian kernel satisfies:

$$\sigma_f \cdot \sigma_t = \pi/2 \tag{2.16}$$

Which gives $\sigma_t \sim 0.6ms$. Fig. (2.16) shows how the Gaussian filter removes ripple in the magnetic field. Overall, we find a combined algorithm which is able to quench magnetic field on by 0.5G within 1ms, and with less than 10mG of swing (2% ripple). Given that this is achieved on the top of Bitter coil holding a field of 890G, I think this is smart and we name it as 'Smart Shim Jump' in our control sequence.

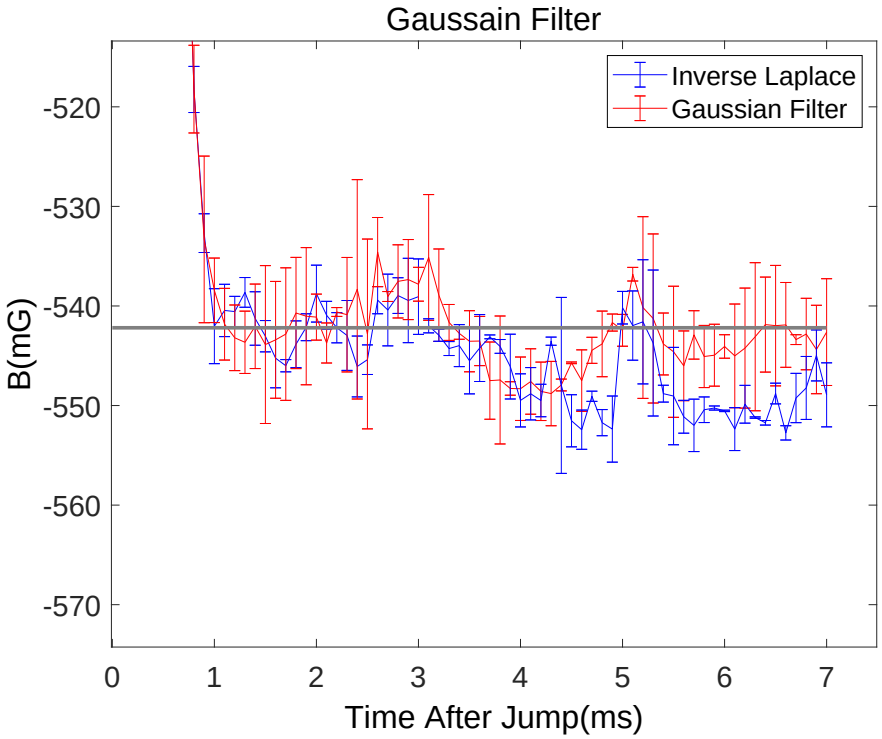

Figure 2.16: Further optimized magnetic field jump using Gaussian filter method Iteration of Gaussian filter will further improve the field response until immersed in field measurement noise. Another comment is, the quench is limited to 0.5G due to the maximum output current of shim driver. The 0.1ms delay comes from driver circuit.

CHAPTER 3

HIGH RESOLUTION IMAGING OF BOSE-FERMI MIXTURES

More advanced tools for detection and control of ultracold atoms are among the most important pursuits in cold atom experiments. Start from time-of-flight method[159][21] in the early days to single site resolution [9][52] and optical tweezer array of atoms [87], detection and manipulation take on more priority in experiments. This chapter describes the commonly used probing and manipulating tools for the Bose-Fermi mixtures. Especially, the design and optimization of a high resolution imaging system will be included.

There is a variety tools to probe the Bose-Fermi mixtures. From horizontal imaging, we can perform either in-situ or time of flight imaging. Around 2019, we upgraded the vertical imaging system with a high resolution microscope. The vertical imaging system is combined with a digital micro-mirror device (DMD), which enables projecting a repulsive optical potential. Aside from having a more versatile Bose-Fermi experimental platform, there is a lot of subtly and caveats in design, installation and optimization of the imaging system. On the other hand, integration of new system brought change of vertical imaging scheme, which involving searching for different imaging state. At the end of the chapter, techniques for dealing with ultra high optical density Cs cloud will be discussed.

3.1 Some Theory of Optics

Before diving into technical details, it's good to introduce some concepts about imaging and optics. Though there is really long history of optics in history, ideas and concepts in modern optics were not introduced until last century. These concepts, pioneered by Ernst Abbe and Lord Rayleigh, emphasize treating the imaging system as a linear system and analyzing their properties in spatial frequency space.

Fig. (3.1) shows a generalization of an optical system. Viewing the whole imaging sys-

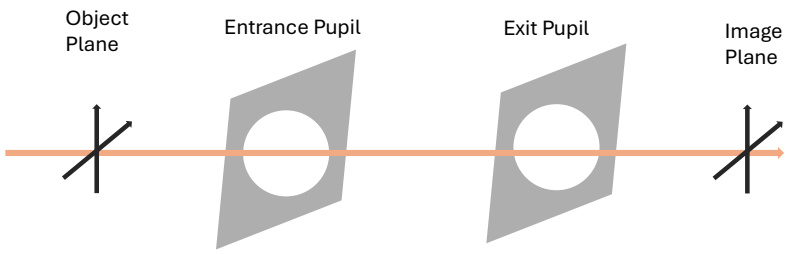

Figure 3.1: Generalization of optical system. Instead of treating the optical system element by element, substituting it with a black box with 5 key gradients is a better treatment. While object plane, image plane and optical axis still being the same concepts in geometrical optics, entrance pupil and exit pupil are newly introduced concepts. These 'pupils' do not necessary corresponds to any physical pupil in the system, but rather they correspond to the same resolution limiting element in the optical system.

tem as a black box with entrance and exit pupils. By analyzing an optical system in spatial frequency space, we study how the imaging system deliver information in each Fourier component from object plane to image plane. This is similar to study an op-amp circuit in bode plot. Given that optical elements have finite physical size, there must be one or a few elements put a limit on the highest spatial frequency which can transmit through the system. In engineering practice, it's better to put a physical cut off on allowed spatial frequency in Fourier space, rather than having a random aperture introducing a cut-off together with unregulated aberrations. Usually introduced apertures correspond to the entrance and exit pupils in Fig. (3.1). Given superposition nature of Maxwell equations, an optical system is a linear system in most cases. For coherent light, it's linear in amplitude of electric field of light whereas it's linear in intensity for incoherent light. However, for cold atoms experiment with absorption or fluorescence imaging, owing to the fact that atom absorption/ emission of light are usual uncorrelated. The imaging process is treated as incoherent imaging system. A more rigorous discussion of coherence topic is presented in Ref. [61].

Given an intensity distribution in object plane, $I_o(\vec{x_o}, \vec{y_o})$, where $\vec{x_o}$, $\vec{y_o}$ is the coordinate in object plan. The corresponding intensity distribution in imaging plane $I_i(\vec{x_i}, \vec{y_i})$ is:

$$I_i(\vec{x_i}, \vec{y_i}) = A \iint |h(\vec{x_i} - M\vec{x_o}, \vec{y_i} - M\vec{y_o})|^2 I_o(\vec{x_o}, \vec{y_o}) d\vec{x_o} d\vec{y_o} \tag{3.1}$$

Where M is the magnification of imaging system. With a Fourier transform of followed by convolution theory, one obtains:

$$G_i(\vec{f_x}, \vec{f_y}) = H(\vec{f_x}, \vec{f_y}) G_o(\vec{f_x}, \vec{f_y}) \tag{3.2}$$

Where $G_i(\vec{f_x}, \vec{f_y})$, $G_o(\vec{f_x}, \vec{f_y})$ and $H(\vec{f_x}, \vec{f_y})$ are the normalized spectra transfer function. Since $H(\vec{f_x}, \vec{f_y})$ is related to the Fourier transform of the point spread function, equation 3.2 demonstrate a concise connection between image and object, connected by transfer function $H(\vec{f_x}, \vec{f_y})$. In engineering practice image contrast, or equivalently, the modulus of above transfer function of more interest. This quantity is named as modulation transfer function (MTF). For a more in detailed derivation of Fourier optics, check out Ref. [60].

In optical engineering, MTF is usually simulated with ray tracing in optical designing software such as Zemax, which uses ray tracing to predict the performance of some design. There is a lot of topics in optical engineering. Ref. [55] is will be a good introductory to Zemax design, and Ref. [141] is a good book for general topics on optical system designing.

3.2 Designing High Resolution Imaging System

The LiCs high resolution imaging system includes a high quantum efficiency camera (Andor Ikon-M CCD), a digital micromirror device (Texas Instruments DLP3000) and a dual wavelengths(852nm, 671nm) diffraction-limited microscope designed by Special Optics (part number 1-26786, project number E4072). The entire system is capable of imaging both species and project a repulsive potential on mixtures with a 635nm laser. Fig. (3.2) shows its layout. In between the objective and the eyepiece, there is a region where the beam propagate almost in parallel. This is the infinite conjugate space, which is common in mod-

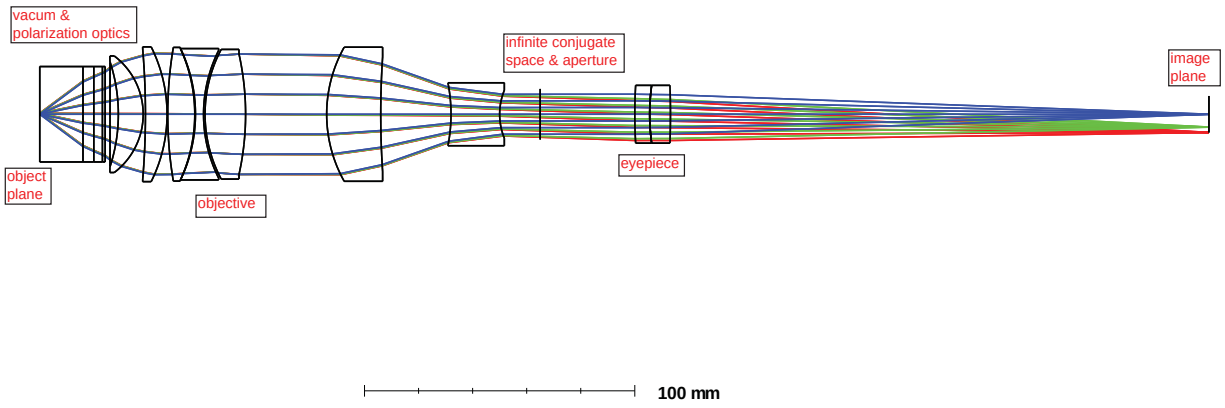

Figure 3.2: Microscope layout. From left to right, starting from atom position, these elements are vacuum, vacuum windows, quarter waveplate and a wire grid polarizer. After which the curves surfaces represent the microscope structure. The beam of different colors shows the beam trajectory initial at different position on the object plane. Again, remember the term 'aperture' is not the same concept as 'numerical aperture'. The microscope has a magnification of 16.75, a geometric depth of focus of $2\mu m$ and a diffraction depth of focus of $2.5\mu m$.

ern optical system design. It grant the user some freedom to adjust according to physical constraints in their application, as well as a place to inset optical elements with an angle. (To understand this: the image is focused at infinite therefore a tilted optical element won't hurt the imaging quality. This is the correct way to insert dichroic mirror.)

The objective is designed to be diffraction-limited with numerical aperture(NA) NA = 0.6, which by Rayleigh criterion $r = 0.61\frac{\lambda}{\mathrm{NA}}$ the resolutions are $0.87\mu m$ for Cs and $0.68\mu m$ for Li. To integrate it with a DMD, we need an extra telescope to couple the optical paths, see Fig. (3.4). For a curved optical surface, the accumulated spherical aberration scales as $(n_{\mathrm{in}} - n_{\mathrm{out}})/R$. Where n_{in} and n_{out} are refraction index before and after the optical surface, and R is the radius of optical surface. An achromat lens is glued by two different type of glasses with different indices of refraction (sometimes one of the material is air gap), which is designed to minimize achromatic shift as well as spherical aberration as mentioned above. For a delicate optical system, even operating at single wavelength, achromat lens is always recommended since it usually has minimum spherical aberration. Fig. (3.5) and

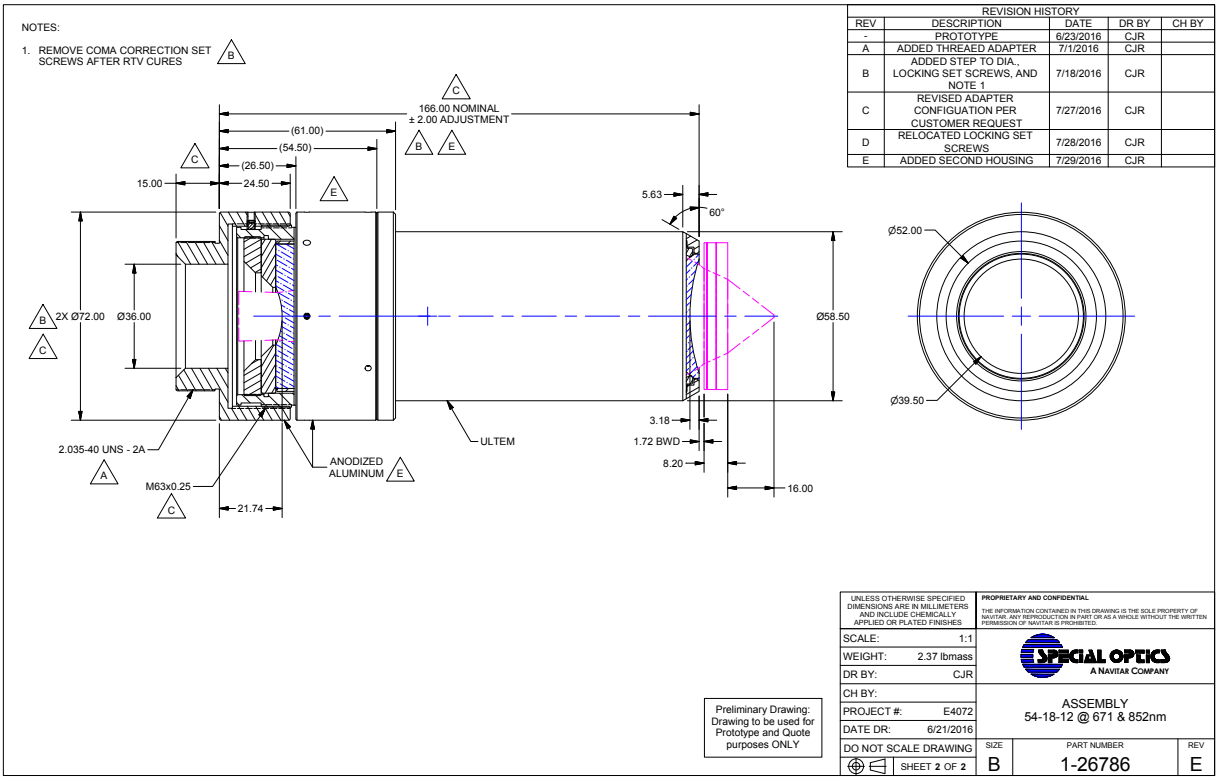

Figure 3.3: Design of microscope objective. The holding structure of the objective which is partially inserted into the recessed view port is made of ultem plastic, in order to minimize eliminate eddy current during field change as the case of metal structure. The thermal expansion rate of the entire objective is estimated to be $\sim 3\mu m/^{\circ}$C, which requires that the temperature stability around it to be within a degree. On the left end, it features a 15mm long threads, which is designed for coarse adjustment on axial direction. This long thread structure is connected with the major structure with 3 'coma correction set screws'. These set screws, are designed for axial direction fine adjustment. The screw threads is M63-0.25(mm), which allows $0.69\mu m$/degree resolution. The Allen key for adjust these set screws are 0.05in diameter.

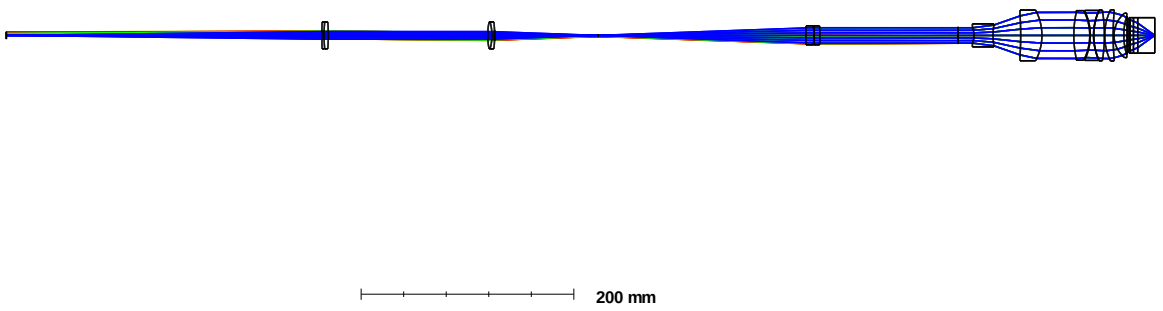

Figure 3.4: Layout of DMD's optical path. A pair achromat lens (f=300mm, f=100mm) forms a telescope which introduce 3x demagnification the DMD imaging before its couple into the telescope part on the right. The simulation is flipped here since we care more about what's the quality of projection on atom plane.

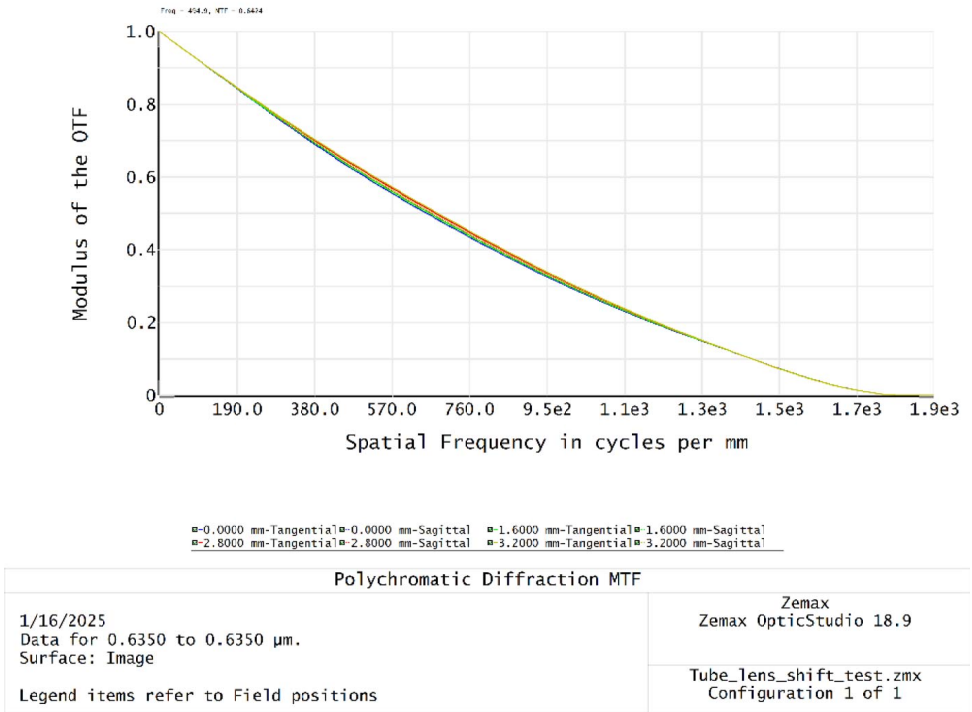

Figure 3.5: MTF curves of the DMD projection system. A well-designed system usually has a smooth decaying MTF curve. This figure also demonstrates that the sagittal and tangential perform, either in the center of edge of the field of view, are closely good.

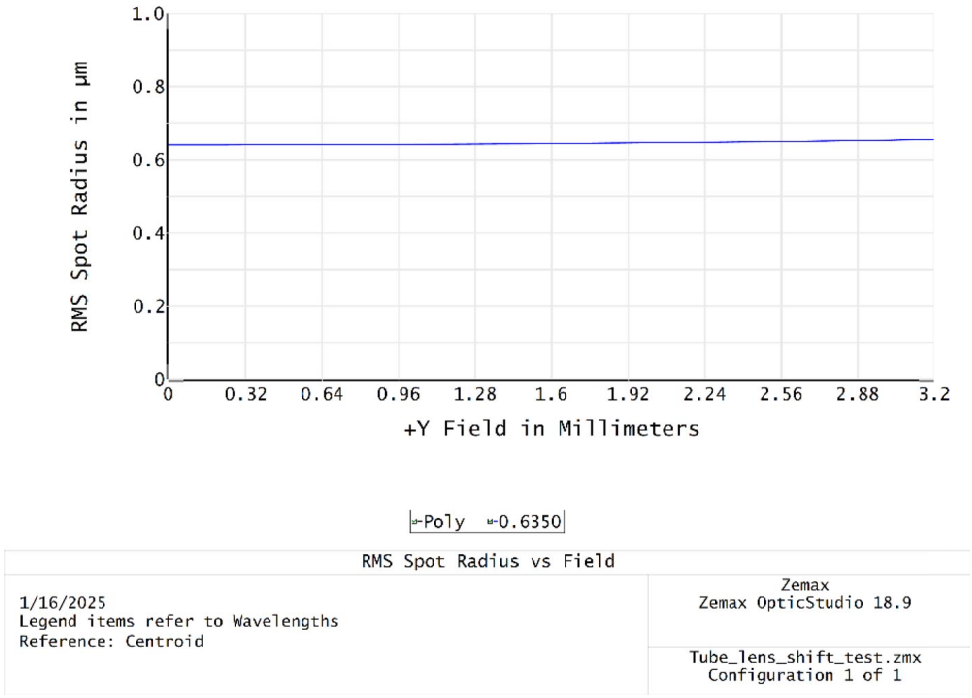

Figure 3.6: Root mean square spot radius of the DMD projection spot. The RMS spot radius is uniform across the entire DMD area.

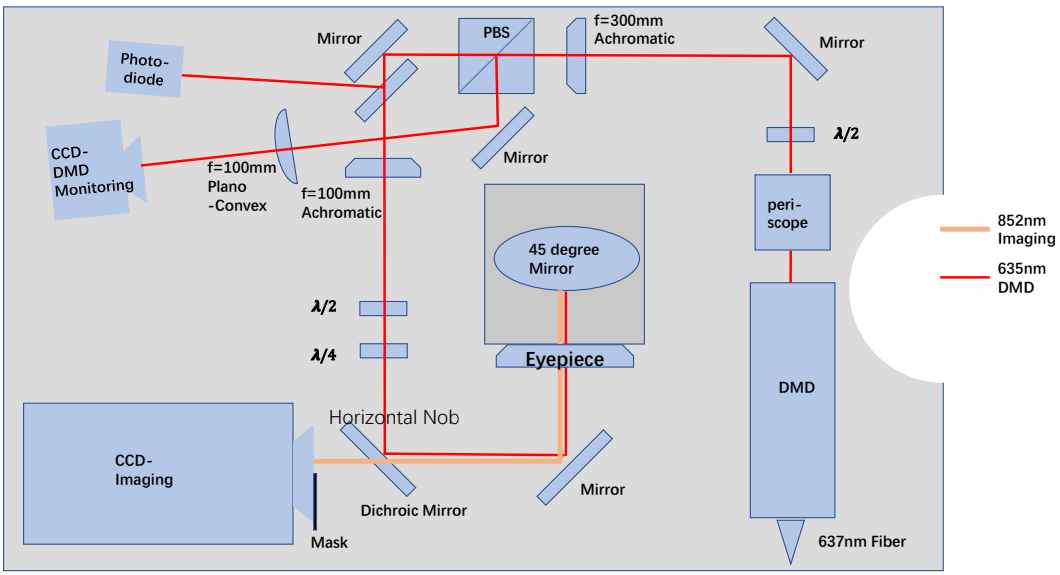

Figure 3.7: Cartoon for the physical setup. The microscope objective is underneath the 2 inch 45 degree mirror, connect to the platform with a structure of breadboard - XY translational micrometer stage (Newport 406 DWG-S) - tilting angle micromirror mount (Thorlabs GM200) - objective.

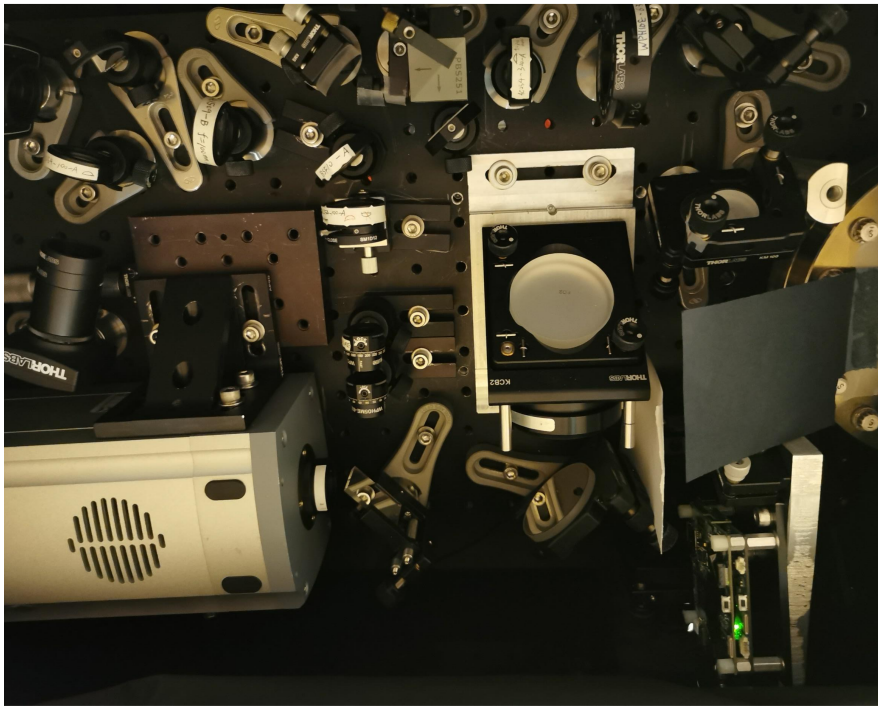

Figure 3.8: A photo of the physical layout of the vertical imaging system. The breadboard is 2 inch thick to mitigate vibration mode. The second achromat f = 100mm is installed on a small translational stage.

Fig. (3.6) show the MTF and root mean square spot radius of the DMD projection system. As indicated by these plots, the design is in principle almost diffraction-limited. Fig. (3.7) and Fig. (3.8) shows the cartoon and a photo of the physical layout.

The entire setup is currently integrated into the experiment. The platform is mounted on the dipole trap level of the breadboard and the C-shape clamp on the Ti-Sub pump. See Fig. (3.9). It worth a mention that, in our current working condition, the microscope's first optical surface is only few tens of μm away from the polarization optics underneath, which is unfortunately configured with almost no design tolerance.

Here we list a few quick facts about DMD. The DMD is capable of projecting $300\mu K$ of optical potential on the fermions. The DMD laser itself is capable of output 138mW at 200mA driving current, at wavelength of 635nm. When all DMD mirror is turned on, around 30mW of power could be diffracted. The DMD device itself, is consists of a system PCB and a driver board PCB, connected by vertical pins for interboard communication. The former is responsible for receiving data input and trigger, while the latter is for actual pattern displaying. Each of them is a textbook Von Neumann architecture of micro-computer.

Here I lists the important bench test alignment procedures.

(1) Mount the breadboard on posts, prepare beams with necessary wavelengths and setup an AOM for CCD imaging purpose.

(2) Setup the 635nm beam with beam shaping prism pair (or lens), an aspect ratio of 2 would be ideal. Make sure the output beam is not clipped.

(3) Mount the DMD on breadboard, turn on all DMD mirrors and maximize diffraction efficiency. The appearance of high order diffraction spots would be a good indication of aliment quality. After that, turn on the only center chunk of pixels and make sure the DMD beam point is not too wrong.

(4) Use the periscope, set the beam height to be 54mm and align the beam to be parallel to breadboard. It is important to make sure the horizontal direction is unaffected, otherwise

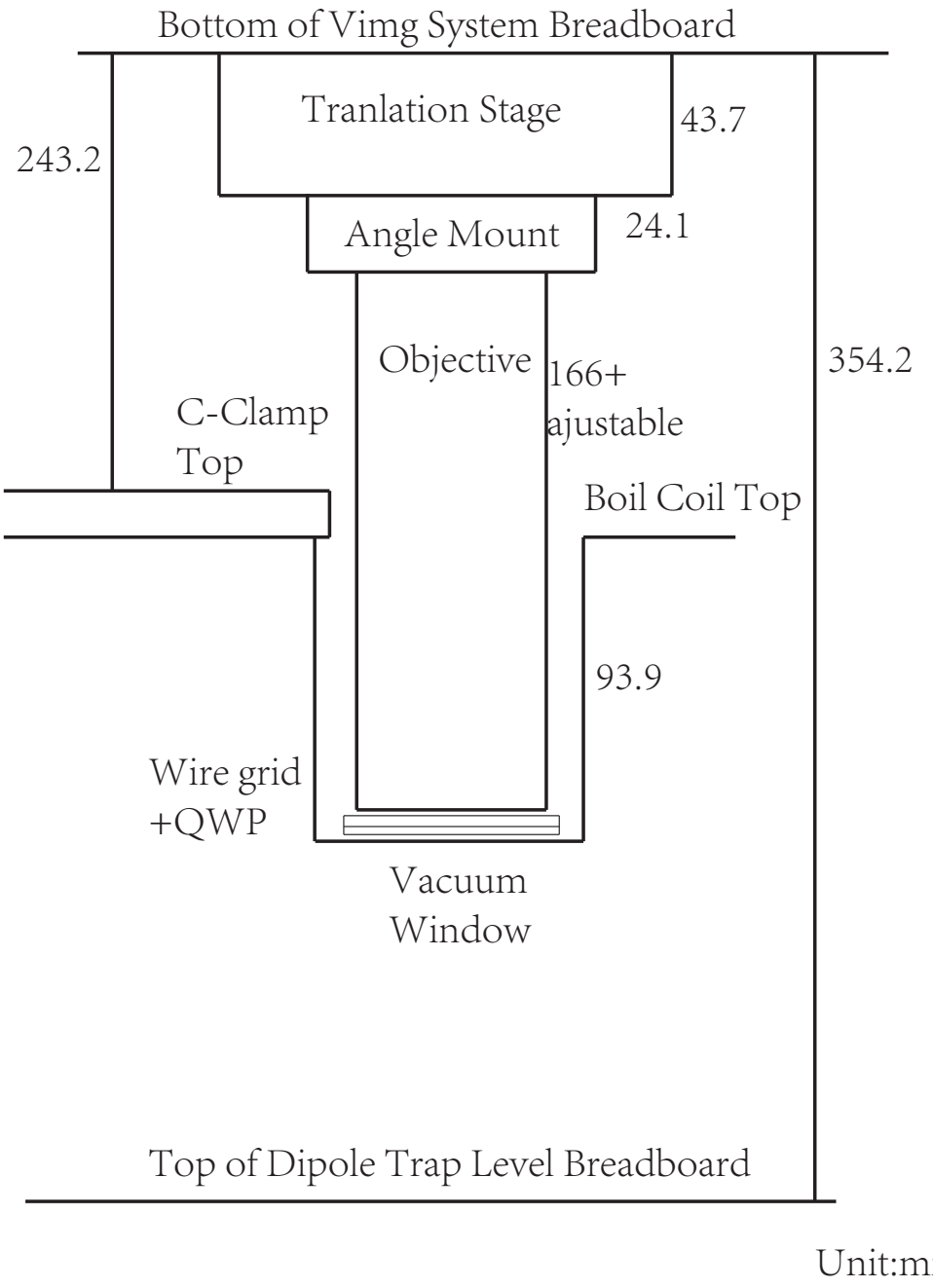

Figure 3.9: Important vertical dimension of imaging system. The breadboard and the 2in thick optical posts are connected by home made machined aluminum adaptor. The wire grid polarizer and half wave plate are held together with 3D printed mount. Krutik Patel and I tried our best to measure these dimensions yet don't take it as absolute.

the DMD image will be distorted. Besides, turn entire DMD on with a lattice of 6 pixels, make sure the desired Fourier component is not clipped.

(5) Time to put in the first half waveplate and PBS and fixed their position, since sometimes they would introduce very slight alignment change. Also put in the 45 degree beam sampler: it is 5mm thick and will deflect beam path quite decent.

(6) Put the 2 inches target on the 45 degree mirror mount, and take away the 45 degree mirror. Adjust the dichroic mirror and the 2 inch mirror before the mount, make sure that the DMD beam go through the center of target and the transmitted beam is still parallel to the breadboard. This is the coarse alignment of the DMD beam.

(7) Before proceed, double check the incident angle beam on dichroic mirror, make sure it is the angle is properly set. Especially, check the reflection and transmission rate.

(8) Put back the 2 inch 45 degree mirror and send the DMD beam downwards optical table. Put a mirror (2in mirror would be better) underneath (on optical table on some mount) and use the 45 degree mirror mount to retro reflect the beam. Most manufacturers make the back surface flat so it is a good flat surface. Or even using water surface, but bear in mind that water surface need to be wide enough so that the surface is not curved by surface tension.

(9) Install a 'fake' microscope on the XY and translation stage. The 'fake' microscope is made with 2 inch diameter lens tube with 2 irises on two end, the entire length should be similar to that of the true microscope. Use the XY-stage to make sure the beam pass through the first iris and use the angle mount so that the beam passes through the second iris.

(10) Take down the 'fake' microscope, place the 1951 USAF target 185mm away from the bottom of angle mount. The target should be placed on an adjustable stage as well (especially vertical translation and tilt correction.) Use tilt correction to make sure the target is placed flat.

(11) Now setup imaging beam. Back-propagating a well-collimated 671nm/852nm beam, adjust its pointing and position such that it perfectly overlap the DMD beam. Use tape or something else to fix the target.

(12) Mount the Andor camera and setup the parameter for imaging. Notice that the beam of the 671nm/852nm beam should be aligned to the center of field of view on real experiment (fast kinetic mode).This is the end of coarse alignment.

(13) Construct the DMD beam path. First put the $f = 300mm$ achromat 30cm away from DMD mirror. Try to make a very big but clean images few meters away. This means that the space after the first achromat is infinite conjugate space and have higher tolerace for beam path variation. In the meanwhile, use an iris and the 2in hanging target to make sure you do not introduce extra beam deflection.

(14) Place the second $f = 100mm$ achromat 30cm (eyepiece focal length) + 10mm away from the eyepiece position. The achromat should be installed on a translational stage for fine adjustment. Especially, you should check that at the two extreme of the stage, this lens does not introduce beam deflection. By now, a rough DMD path is set.

(15) Install the eyepiece (double check direction of optical surface, otherwise you will introduce big chromatic aberration later). Adjust the camera position such that the 671nm/852nm beam (lower down the power) is focused on the CCD. (14) Install the objective. Use XY and tilt mount for optime the resolution on USAF target. When thing are really off, it is a good idea to maximize the photon count until you find the correct focused image. This will be some sort of blind search in the beginning. Try to fine adjust the XY and tilt such that the image of the USAF target looks the best, especially, make sure you have a broad and nice field of view, as what the original Zemax design suggests.. At this point, your DMD and 671nm beam are still copropagating. A good 671nm/852nm image means that this part of the optical path is good for 635nm DMD beam as well.

(15) Fine tune the DMD path. Tune on some DMD pattern, the is nob on dichroic

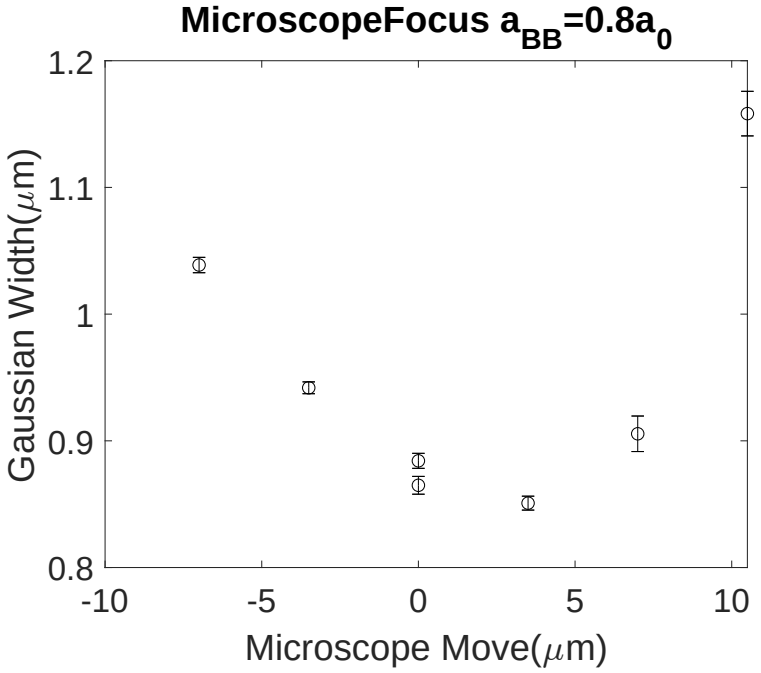

Figure 3.10: Fitted cloud width of BEC with zero scattering length $a_{BB} = 0$ for different vertical microscope objective position. When using a BEC near zero crossing as a target, one should notice that including the thermal wing in the fit will broaden the fit yet it is not a sign that the resolution is bad. In this scan, a BEC with less than $0.9\mu m$ is imaged. Please remember that, while performing such fine tuning focusing, please the allow the entire system to thermalize long enough before taking action.

mirror and the mirror nob in between the two achromat as well as the translational stage. Remember try not to use too much on the mirror mount in between since that's not designed for that. By now, you should have a DMD image.

3.3 Imaging System Optimization

When vertical imaging system is calibrated, it is time to migrate the setup into system during which the process the Andor camera and microscope are taken down for safety precaution. The 2 inches thick aluminum platform is connected with the main experiment with four 2inch diameter optical posts. The translational stage and angle mount are taken down to make enough room for installation maneuver. The microscope is installed with its length set at its minimum to avoid touching the optics near the vacuum window. The initial stage

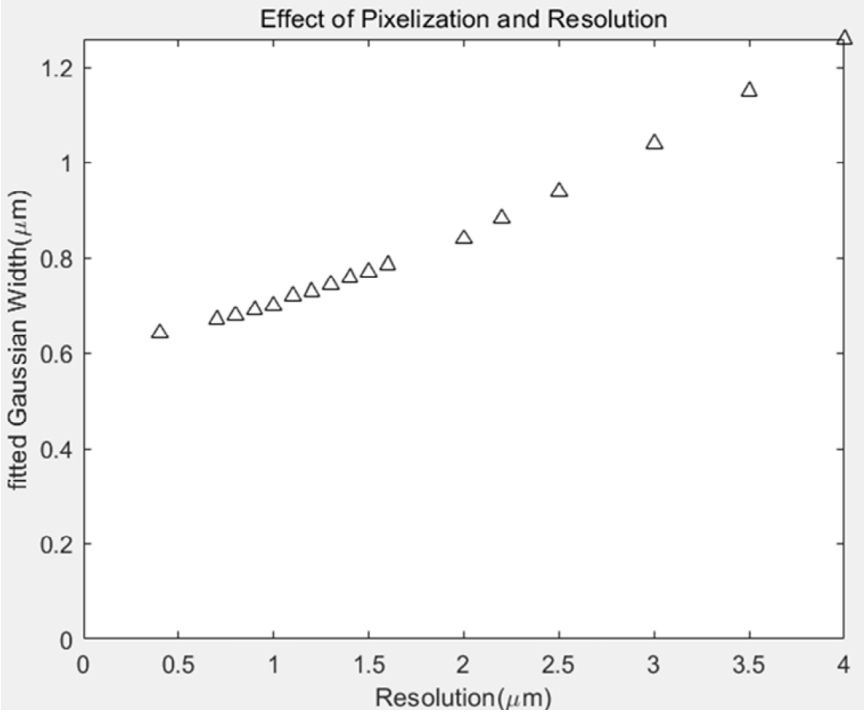

Figure 3.11: Fitted zero Bohr BEC Gaussian width versus optical resolution. Simulation of pixel limited effect on our resolution. The fitted cloud width is getting smaller in a slower way as resolution approaching zero. One could imagine that, even looking at a delta function in atom plane, the fitted Gaussian width would be a few fraction of the pixel size, showing the impact of Nyquist theorem. In practical engineering practice, the pixel size should be 1/3 or even 1/4 of the resolution limit.

microscope focus is tuned by coarse threads trying to get a image of Cs cloud in oTOP. When the microscope focus is really far, the cloud on image has a feature of two strips. This process is continued by focusing on colder and colder cloud. When coarse focus is complete, the microscope connection at coarse thread should be tightened by a 2 inch diameter retaining ring. That retaining ring has too small holes drilled in opposite, so that the retaining ring could be tightened in that limited space. After coarse tuning, the fine focusing is performed by imaging a pure BEC near the Cs-Cs zero crossing, which is the smallest target available target on experiment.

Fig. (3.10) shows the fitted BEC size as a microscope focus scan goes on. With some algebra, one realizes that resolution is 2.9 times of a fitted Gaussian width. Does this means

that our microscope resolution is as terrible as $2.5\mu m$? This is not the entire story. The major limiting factor here is the too large pixel size on the atom plane. Most of the time, CCD pixel which has high quantum efficiency are even slightly larger than CCD pixel of a usual camera. In our system, the Andor camera pixel corresponds to $0.78(2)\mu m$ on atom plane. During our early microscope designing stage (even before I joined the group), the microscope magnification is chosen to be $\times 16.75$ so that it have the ability to image the entire degenerate Fermi gas. This is a good design choice yet with the penalty of being pixel limited on resolution. According to Nyquist frequency theorem, for even size of discrete system, the information the system obtained is cutoff at highest frequency 0.5/pixel size, which could be easily understood that if you receive a signal with one pixel on and the next pixel off. Therefore, the pixel limited resolution is $\sim 1.6\mu m$. On the other hand, a pixel limited system doesn't mean that you can not find a target with fitted Gaussian width below that. Fig. (3.11) shows a simulation of what a fitted Gaussian width is as a the resolution getting better. As shown in the figure, the actual optical resolution getting less and less important as it getting below the Nyquist resolution. In fact, the change in fitted resolution getting smaller and very quickly get immersed in a measurement noise. From Fig. (3.11) and Fig. (3.10), we may only roughly conclude the resolution is around $\sim 1.6\mu m$. Though, from other measurement such as DMD light diffraction or phase imprinting mentioned in later chapters of the thesis, we could conclude it is better than this.

After the microscope is well focused, it is a good idea to focus the DMD in a row. Compared with microscope focus, tweaking DMD focus is relatively easier. It relies on the translational stage under the second achromat. In terms of criterion for optimization, in past years we have tried many ideas and here are the two method works better:
(1) Point spread function method: For coarse alignment, turning on a stripe of DMD potential with a width of a few pixels. By maximizing the depletion it created on a pure BEC, you will get the bulk part right.

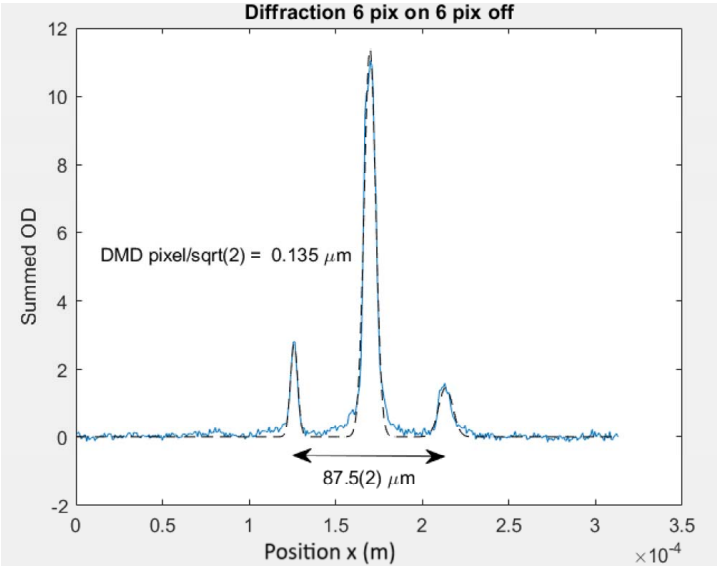

Figure 3.12: DMD diffraction. Measure DMD pixel size and optimize DMD focusing with diffraction method. After DMD diffraction pulse, the boson-boson interaction is turned off. Therefore the Cs atom in excited momentum states travel freely. With a 1/4 trapping period (time of focus), these atom reaches their maximum position in the weak trapping axis. The asymmetry on the two diffracted peak could come from either the DMD projection alignment or the microscope alignment with respect to atom.

(2) Fourier component method: Turing on a periodic pattern on a pure BEC, and maximize the Fourier component on it. This will allow you to do a fine tuning on the top of (1)

(3) DMD diffraction: No longer recommended but an important one: Prepare a pure BEC with a few tens of Bohr (so that it is large enough for diffraction.) Shine a DMD lattice pulse quickly and quench boson-boson scattering length $a_{BB} = 0$, the diffraction will create diffracted order, which serves as a good measurement of projecting strength and DMD pixel size. See Fig. (3.12).

Due to the fact that the whole cloud is cigar shape, we haven't find a very good way to correct tilt and astigmatism on DMD alignment.

To increase the imaging quality better, tilt correction is necessary. For microscope tilt in tight axis, it is simpler. By observing the Airy disk fringes of an averaged images of BEC near zero cross, the direction tilting could be inferred. As shown in Fig. (3.13). For tilt correction

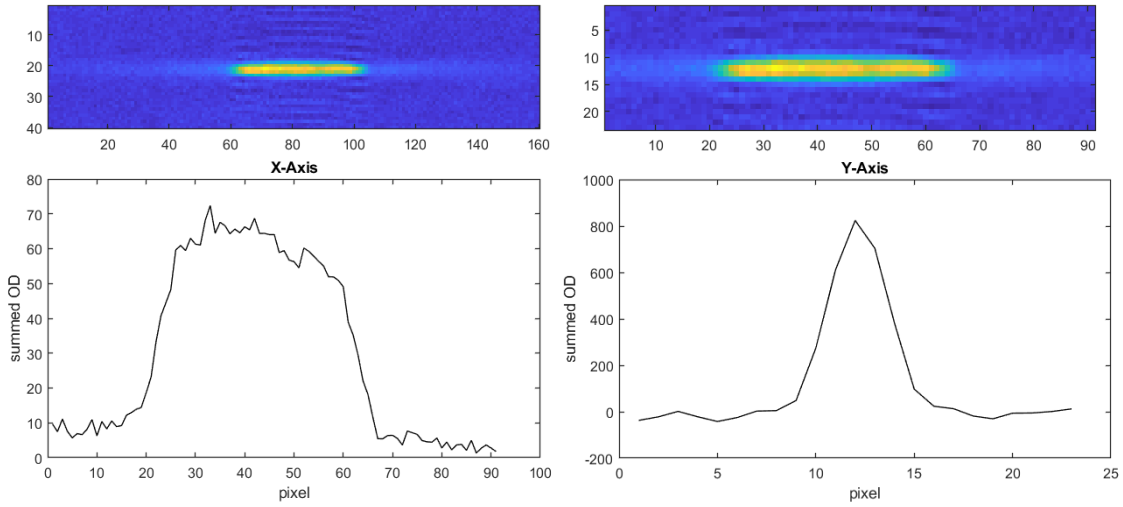

Figure 3.13: Microscope objective tilt correction along tight axis of final trap, based on averaged images of BECs with boson-boson scattering near zero crossing. After correcting tilt in Y-axis, the Airy disk type pattern is more symmetric around the BEC.

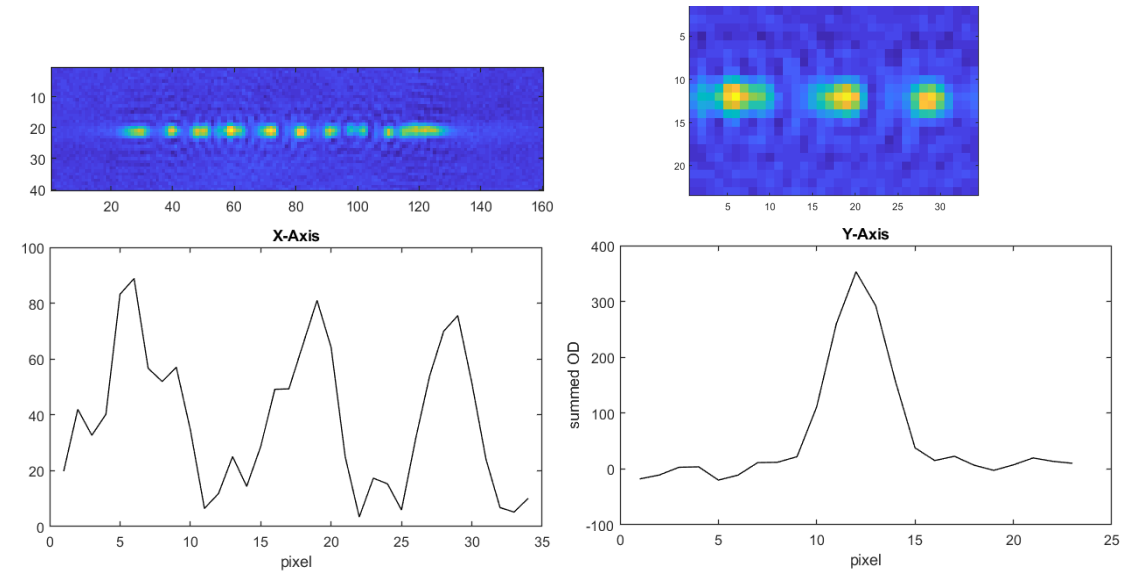

Figure 3.14: Microscope objective tilt correction along shallow axis of final trap. By applying repulsive lattice potential from DMD, BECs near with scattering length near zero crossing are divided into smaller BECs. Among these smaller BECs, it is possible to select some of them such as imaging targets.

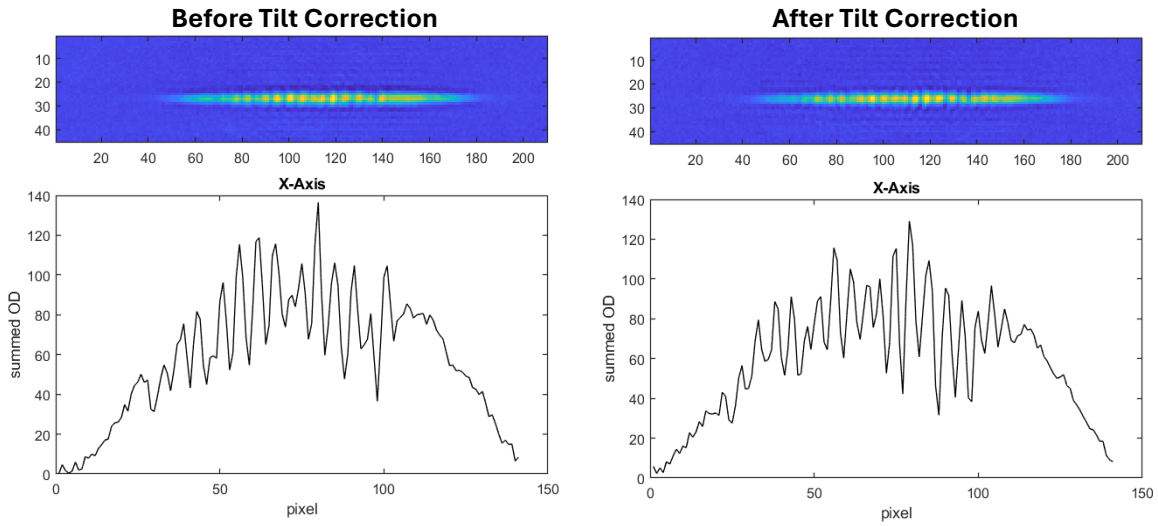

Figure 3.15: Comparison of imaging quality before and after the tilting correction. In the tight trap axis, the uncorrected image shows an obvious asymmetric fringes near the BEC. For the shallow axis, the DMD projection quality is improved as well.

in X-axis, we need to utilize the DMD projection power. By adiabatically turning on static potential, the near zero crossing BEC will be cut into small targets. Again, by correcting Airy disk pattern's asymmetry of averaged images, one could correct the X-axis tilting, see Fig. (3.14). Fig. (3.15) shows a comparison before and after the tilt correction. From my experience over the years, this is the best microscope and DMD alignment one could achieve. Better temperature control and stability is required for further imaging system improvement.

3.4 Camera Setting and Imaging Related State

To acquire a high quality image of Bose Fermi mixture, beside properly setting up an optical system, camera setting, atom states involved and parameters for imaging pulses are important as well. From aspect of the camera, one would like to collect as much photon from atoms as possible and try best to reduce irrelevant counts. Counts on camera from different

sources usually obey Possion distribution, resulting in a noise floor as:

$$\delta N_{tot} = \sqrt{\delta N_{dark}^2 + \delta N_{imaging}^2 + \delta N_{dipoleTrap}^2 + \delta N_{roomlight}^2 + ...} \tag{3.3}$$

The largest contribution of non-related photon comes from two origin: dark current and any other light (dipole trap light, room light, DMD light, even indicator light from equipment). The later could be almost eliminate by search for pollution photon source one by one. To shield these pollution, we take multiple measures: we use a combination of black curtain and plastic to shield room light and stray dipole trap light. The dipole traps and DMD are switched off during imaging (if possible). We also use a multi-line filter (Part number: FF01-441/511/593/684/817-25). Currently the room light contribution in each image is as low as 1 photon per pixel. The biggest stray light contribution comes from BFL light which likely comes from the holes underneath the breadboard of the platforms. Yet the diffraction effect of the mask is actually the largest contribution, see Fig. (3.17).

To suppress dark current, the Andor camera is set at $-25°$C, which is the minimum temperature reachable by fan cooling. This temperature is necessary to suppress dark current noise to achieve low signal to noise ratio (SNR) for Li imaging, see Fig. (3.16).

We also use fast kinetic mode imaging to acquire dual species imaging so that we could minimize effect such as imaging system vibration, less count from dark current or irrelevant light. The fast kinetic mode is also a compromise of CCD itself, as the readout speed is always much slower than pixel shifting speed. For fast kinetic dual imaging, we mask off most of the pixel, leaving less than 200 rows. Each dual species image is consists of four stripes of each image. In most of the configuration, the imaging pulse arriving at CCD is: (1)Li atom shot (2)Cs atom shot (3)Li no atom shot (4)Cs no atom shot. The time elapsed in between Li atom and Cs atom shots are around $0.42ms$, short compared with most of timescales for Cs atom. With this, we could get good images for both Li and Cs in one shot.

There is a lot of consideration while choosing the correct imaging parameters (intensity,

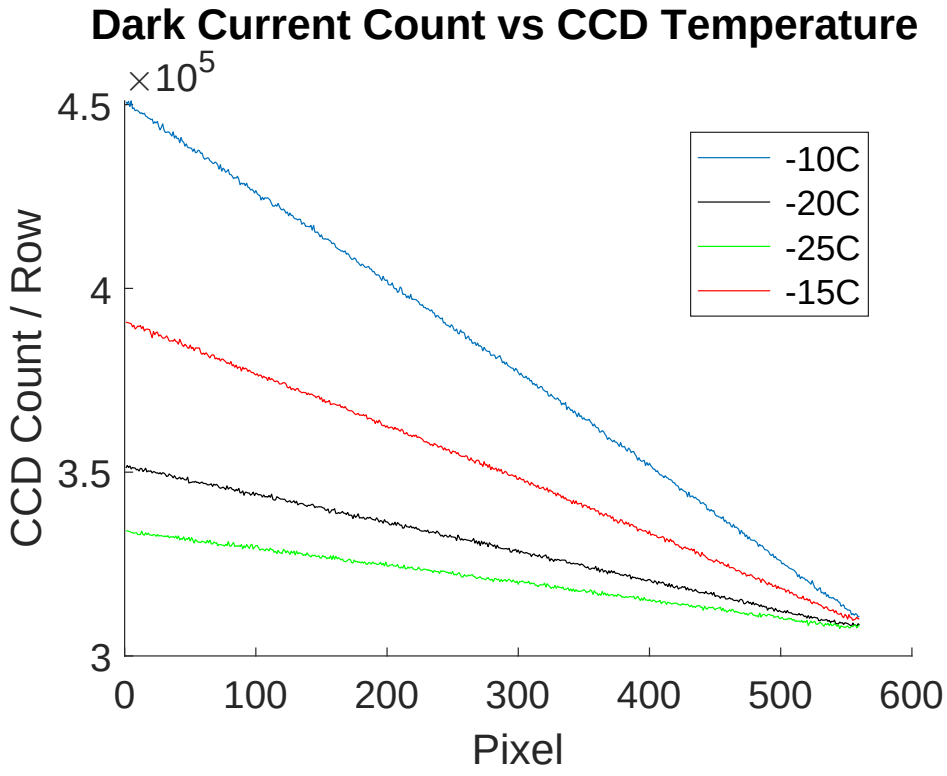

Figure 3.16: Dark Current Count vs. CCD Temperature

pulse duration). For example, the imaging pulse length is chosen to accumulate as much (dark) photon counts before motion due to recoil take effect. The optical pumping pulse, is fired from horizontal direction to avoid photon pollution. It is required that these optical pumping pulses transfer atom to proper stretched states for imaging as fast as possible with large population. Especially for the case of Cs BEC, it needs a strong pulse to penetrate the cloud to avoid density effect. In the case of microwave pumping, the story is different, depending on either if the goal is to get field measurement with power broadening or just for microwave imaging. The relevant pulse length and parameters is listed in table 3.1. The choice of power and how to deal with density effect will be explained in next section.

Another critical problem here is the choice of states for imaging. The MOT optics forbid the use of $\sigma-$ polarization so we have to resort to stretched states with $\sigma+$ transitions. Since our lasers are mostly locked for $\sigma-$ transitions, therefore most of the time it it impractical to use laser lock alone to reach these states. For this purpose, we resort fiber electo-optic mod-

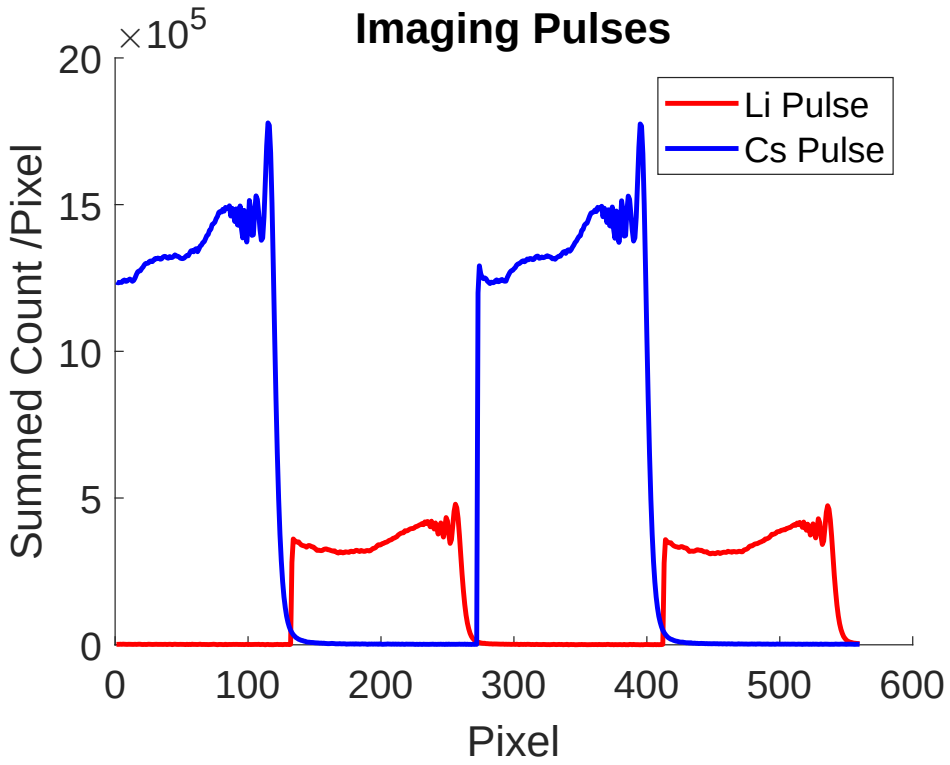

Figure 3.17: The four pulses for dual imaging in fast kinetic mode. The optical density of Cs cloud is usually much higher than the Li cloud, the Cs imaging light has a much higher intensity than the Li. The steep edge (left on each pulse) comes from the edge of CCD surface whereas the smooth edge with ripples comes from the manually inserted mask. Since there is some distance from the mask to actual CCD, the diffraction effect is obvious and currently this is the biggest source of photon pollution, especially for Li imaging.

Li Optical Pumping	$2\mu s$
Li Vertical Imaging	$5\mu s$
Cs Optical Pumping	$2\mu s$
Cs Vertical Imaging	$5/10\mu s$
Cs V-Microwave Pumping	$20\mu s$ with $10dBm$ power
Cs V-Microwave Field calibration	$1ms$ with $-30dBm$ power

Table 3.1: Useful Vertical Imaging Parameters. It's also worth a mention that, since these light are close to resonance, a very extinction ratio on the AOM control is critical. The different microwave parameter is intended for power broadening and interaction shift due to strongly interacting Cs atoms in $|F = 4, m_F = 4>$, see 3.18.

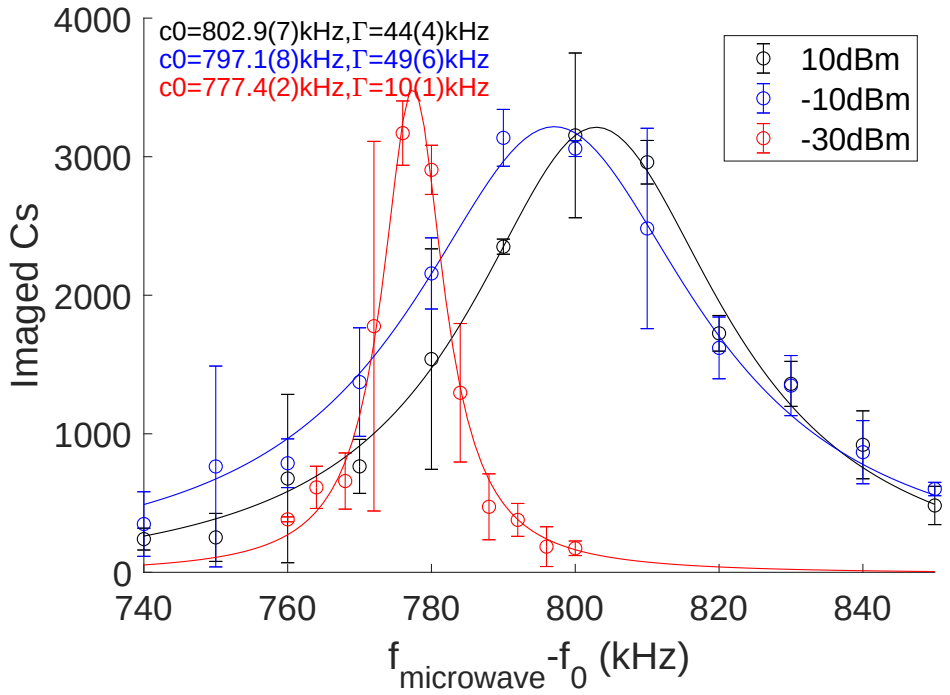

Figure 3.18: Power broadening and interaction shift of microwave pumping. Power broadening and resonance peak shift for microwave pumping of a 1ms long pulse with various power. The $|F = 3, m_F = 3 >$ to $|F = 4, m_F = 4 >$ microwave transition could be RF power broadened. When transferring a large fraction of atom of a high density Cs cloud (BEC), intraspecies repulsion will shift the resonance peak to higher frequency. Here $f_0 = 11439$MHz being the baseline frequency for reference.

ulators (EOM). EOM makes use of electo-optic effect, in which case some specific materials' refraction index varies as a electric voltage is applied. Radio frequency(RF) power is sent into material in which laser light passes through. The phase of the laser light is modulated as:

$$Ae^{iwt+i\beta sin(\Omega t)} = Ae^{i\omega t}(J_0(\beta) + \sum_{k=1}^{\infty} J_k(\beta)e^{ik\Omega t} + (-1)^k \sum_{k=1}^{\infty} J_k(\beta)e^{-ik\Omega t}) \tag{3.4}$$

Where A is the amplitude of the laser, ω is laser carrier frequency, β is the strength of the modulation, and Ω is the modulation frequency of the driving RF power. As equation 3.4 shows, the RF power generates an infinity series of sidebands. The driving RF frequency usually ranges from few hundred MHz to a few GHz. EOM is a fast and convenient tool, though sometimes the high insertion loss and low percentage of optical power in desired sideband could be a headache.

In LiCs system, we use EOM for Li optical pumping while for Cs we found an unexpected transition near where the Cs repumping laser is locked.

• Cs microwave imaging: Microwave pulse pumps Cs in state $|F = 3, m_F = 3 >$ into $|F = 4, m_F = 4 >$ in ground states and the imaging cycling transition is $|F = 4, m_F = 4 >$ to $|F' = 5, m_F = 5 >$. It should be pointed out that the Cs atoms in $|F = 4, m_F = 4 >$ has strong intra-species repulsion, causing interaction shift when too many fraction in BEC is pumped into $|F = 4, m_F = 4 >$, see Fig. (3.18).

• Cs vertical imaging: The Cs in $|F = 3, m_F = 3 >$ ($|m_J = -1/2, m_I = 7/2 >$) is pumped into $|F' = 3, m_F = 3 >$ ($|m'_J = -1/2, m_I = 7/2 >$) with a horizontal repump pulse, and then decay to five possible states. $|F = 3, m_F = 2 >$, $|F = 3, m_F = 3 >$, $|F = 4, m_F = 2 >$, $|F = 4, m_F = 3 >$, $|F = 4, m_F = 4 >$. Here the ground state manifold is in intermediate regime therefore some states are possible with low chance. It seems that the $|F = 4, m_F = 4 >$ ($|m'_J = +1/2, m_I = 7/2 >$) occupy a big amount of population in decaying states. The unexpected transition also has smooth dependence on magnetic field:

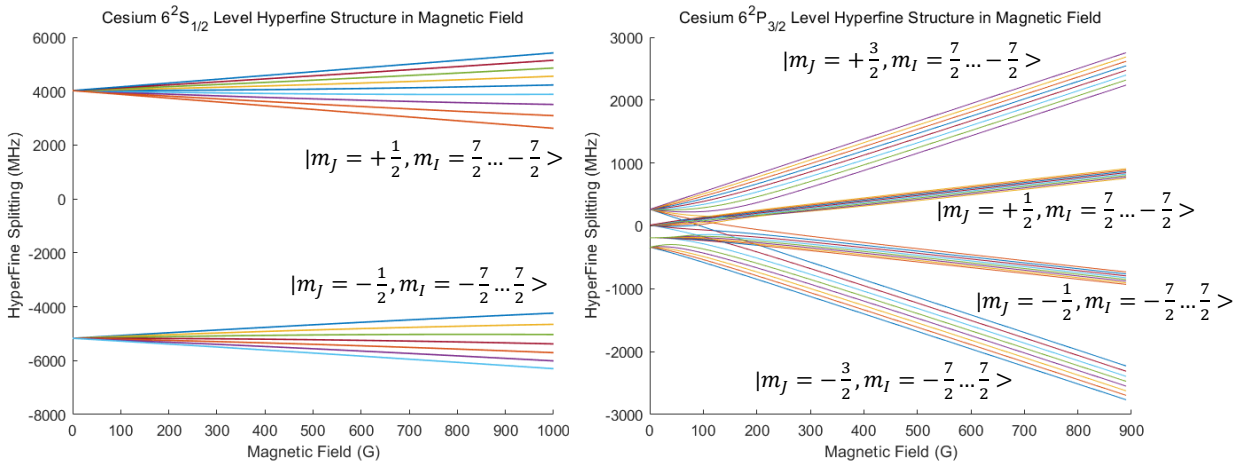

Figure 3.19: Hyperfine structure of Cs ground and excited states. In Paschen-Back regime, the nuclear spin is decoupled from the electron angular momentum (orbital+spin), there energy splitting falls into families labeled by m_J. On the other hand, the nuclear spin g-factor is much smaller than electron g-factor. The fine structure splitting comes from J-I coupling. Therefore the energy ranking is ordered in a way determined by m_J and the slope in each family is determined by the magnitude of $J = L + S$.

which is 0.28MHz/G. PS: one tiny detail might confuse people for a moment: both imaging transition in MOT and imaging seems to has +1 in angular momentum, but please recall that MOT is a retro-reflected beam.

• Li vertical imaging: Li in $|m_J = -1/2, m_I = 1 >$ (Li |a>) is pumped into $|m'_J = 1/2, m_I = 1 >$ in excited state. It decays to back $|m_J = -1/2, m_I = 1 >$ or $|m_J = 1/2, m_I = 1 >$, ie, pumped into Li |e>. The imaging transition is $|m_J = 1/2, m_I = 1 >$ to $|m'_J = 3/2, m_I = 1 >$. Though for our system, though imaging Li has less issue compared with that of Cs, it still comes with the problem that Li atoms suffer a much severe recoil induced imaging frequency detuning. See Refs. [72] [110]

• It is also worth a mention that, both the pumped Cs and Li are low field seeking states, which means the usual magnetic trapping becomes anti-trapping as shown in Fig. (3.19). If there is a too long time gap between pump and imaging, the Li atoms might leak away from trap while for Cs it's usually okay due to its slow timescale.

The RF electronics need to be modified to to reach those frequency. The corresponding

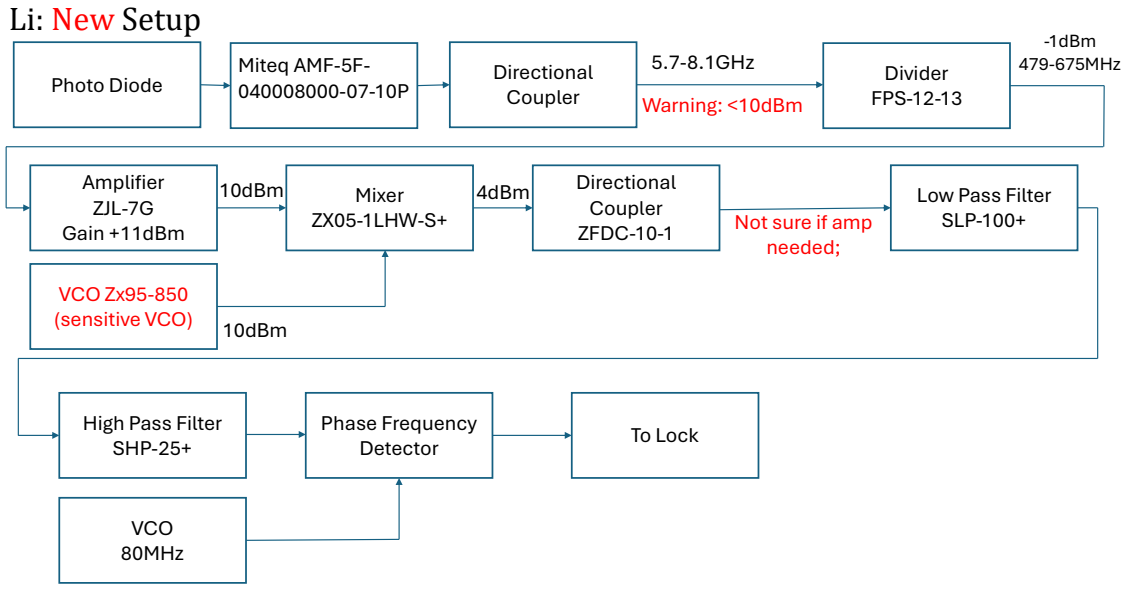

Figure 3.20: Modified Li RF locking circuit. The biggest change happens in the early part of the circuit. For EOM optical pumping, the Li imaging locking frequency need to move by more than 2GHz. Therefore instead of beating with voltage controlled oscillator (VCO) at 9GHz, the beat note is first divided by 12 and beat note with VCO at much lower frequency.

changes are shown in Fig. (3.20) and Fig. (3.21).

3.5 Imaging High Optical Density Cloud

Absorption imaging is applied in our experiment, in which we compare an image with atom cloud shadow with another one without. This method is also well known in application such as determine the concentration of solution in liquid. The optical column density could be inferred as Eq.(3.5):

$$n = \alpha ln \frac{I_{\text{no atom}}}{I_{\text{atom}}} \tag{3.5}$$

where n is the column density alone the imaging beam, α is effective imaging cross section, $I_{\text{no atom}}$ is light intensity without atom cloud, and I_{atom} is light intensity with atom shadow. This can easily understood that the incoming beam intensity decay exponentially as it passes through material layer by layer. However, in case when people want to gather as much

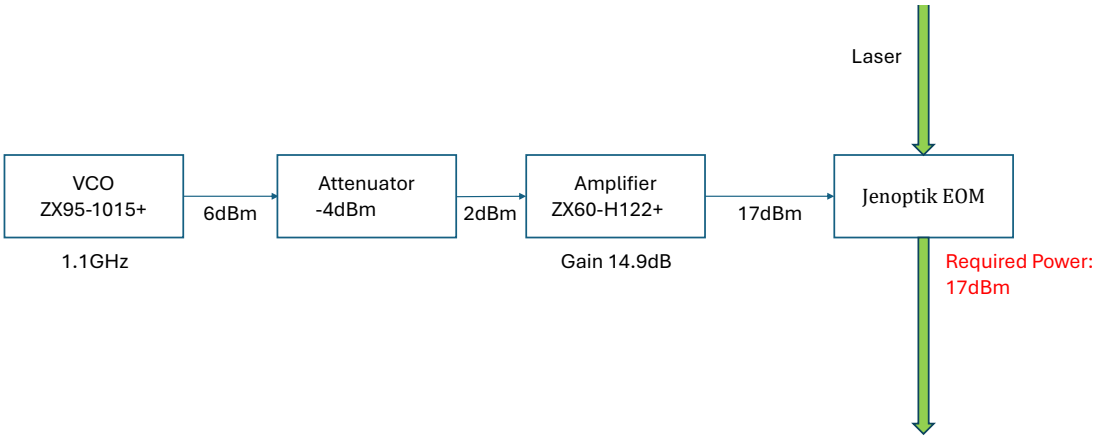

Figure 3.21: Li EOM RF driving circuit. Different from Cs vertical imaging, the Li imaging laser plays both role of repumper and imaging. The EOM beam comes horizontally from a independent fiber launcher. The EOM beam is focused at atom to reach enough intensity for a quickly pumping in $2\mu s$. To avoid resonant light heating, the EOM beam's carrier is deflected in the opposite AOM order compared with imaging beam, so that there is 160MHz (i.e., 30 linewidth) detuning between the carrier frequency and the imaging frequency. The RF driving frequency is a rough number here. Another comment is, this scheme couple the pumping and imaging frequency. In practice, the EOM pumping frequency has bigger tolerance so scanning imaging frequency then EOM frequency will approach the correct setting faster.

information as possible in a limited time (the case for our Li imaging due to photon recoil) or a too thick sample which reduced light intensity by too much such that this method become vulnerable to measurement noise (the situation of Cs BEC imaging), it is better to imaging beam with a few of saturation intensity. One could imagine that in an extreme case of really strong intensity, how fast the intensity decays is determined by how many photons the atom cloud can scatter, which means the saturation intensity plays a role now. Eq.(3.5) should be modified to get the so called modified Beer-Lambert law:

$$n = \alpha \ln \frac{I_{\text{no atom}}}{I_{\text{atom}}} + \frac{I_{\text{no atom}} - I_{\text{atom}}}{I_{\text{sat}}}. \tag{3.6}$$

Here I_{sat} is the saturation intensity of atom being imaged.

Most of the time, the story ends here. However the optical density of our elongated Cs BEC is higher than usual BEC experiment. The high column density makes the reabsorption of scattered photon an important consideration [156]. In a hand waving description, one could imagine that, as the imaging beam travel further across the sample, there is more and more photons originate from atom re-emission, competing with the original photons to excite atoms. Therefore, the atom cross section is deceasing over time, meaning α will grow linearly (at least, as a first order approximation) as optical density increases. Eq.(3.7) need to be further modified:

$$n = [\alpha_0 + a(n\sigma) + b(n\sigma)^2] \ln \frac{I_{\text{no atom}}}{I_{\text{atom}}} + \frac{I_{\text{no atom}} - I_{\text{atom}}}{I_{\text{sat}}} \tag{3.7}$$

Here a and b are linear order and quadratic correction factors. Such correction is no applied in our system, see Fig. (3.22). The power of such modification is apparent: for BEC with high optical density, the fitted Thomas-Fermi radius is no longer changing as imaging intensity changes.

It is also fun to mention why we found this: we were studying the density fluctuation

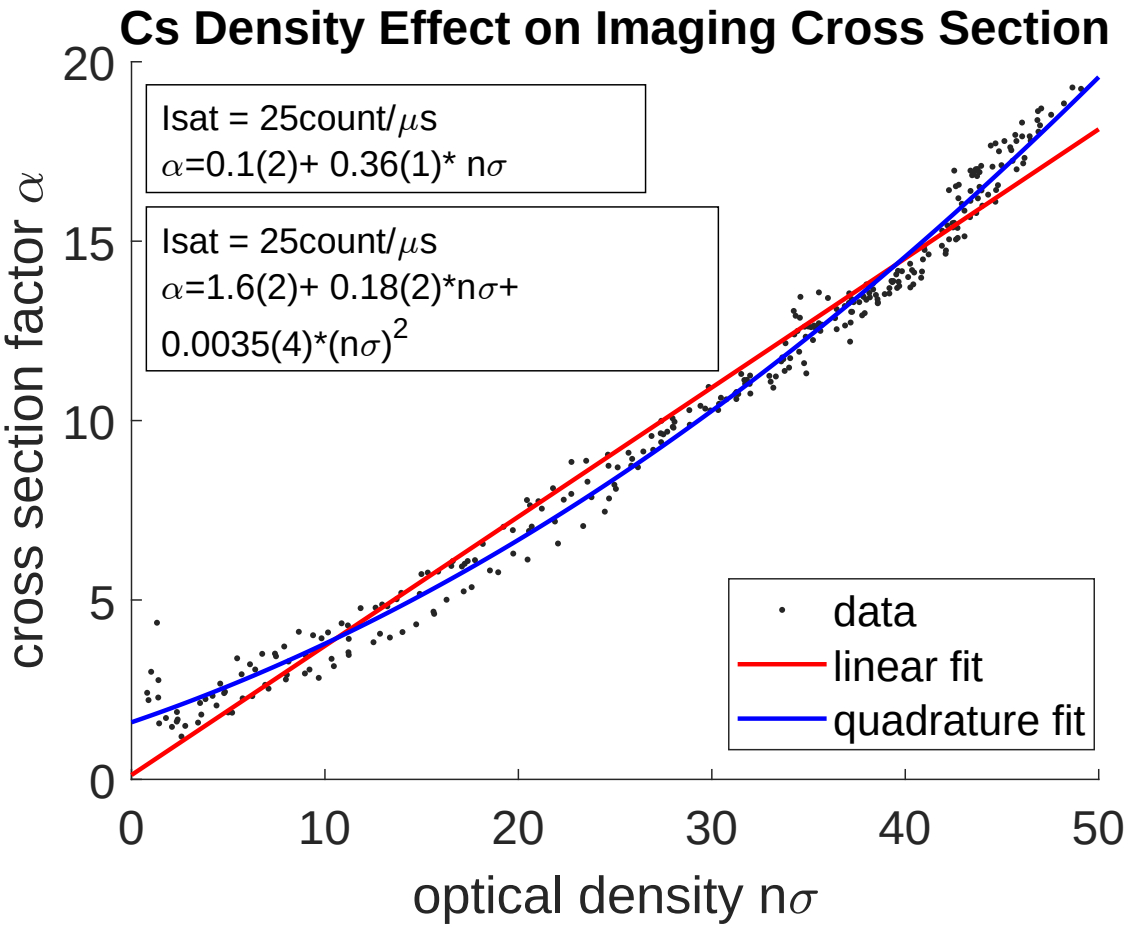

Figure 3.22: High density effect causing a modified-modified Beer-Lambert law. A linear model as well as a quadratic model are fitted. For daily operation, the linear model is numerically more robust in predicting optical density. On the other hand, the data does suggest a measurable quadratic term. The mechanism and its experimental behavior need more investigation.

in our Cs BEC and found that the fluctuation decreases at a really high density. This is indication that the counted number is no longer sensitive to small variation of actual density, which is a direct symptom of counting error.

Finally, there is an overall factor of Cs atom number counting, which comes from polarization and unknown parameters from atom plane to camera, such as transmission rate or polarization. From a very rough comparison of counted Cs BEC number with the Thomas-Fermi radius, this factor is roughly 2.

3.6 Design flaw and ideas for future improvement

At the end of this chapter, I would like to lists design flaw and suggestions for future upgrade.

• It is appealing to re-design the whole system with 3 eyepiece lens and 3 separate beam path for Cs light, Li light and DMD light before they enter the objective, with the dichroic mirrors placed in the infinite conjugate space. While the magnification of Fermi gas is kept the same, the magnification could be changed with a eyepiece lens of twice or three times magnification. An eyepiece with larger magnification will hurt the field of view yet this is not a problem for Cs. Such design will grant the LiCs platform the true ability to do simultaneous imaging, with may lead to new physics [118].

• As you might already noticed during the discussion of infinite conjugate space concept. The dichroic mirror for 653nm light is in placed in an improper place which likely hurts imaging resolution. A design layout mentioned above will eliminate this problem.

• Currently the photon pollution comes from diffraction of the imaging light of the other species. This issue could be eliminated by a true dual imaging design or with a filter designed to be closer to CCD surface.

• Currently, the biggest aberration source comes from day to day temperature instability near the microscope. The resulting focus drift also causes a long waiting time for serious data taking. Henry Ando's new Bitter coil design, or a surround water cooling panel might

help stabilize the temperature and therefore the focus of the imaging system.

• The DMD mirror array chip itself is not well mounted as people took off the optics before it. It is a good idea to design a mount for it (re-alignment on bench is required if decided so). Furthermore, it might not be a bad idea to separate the chip and the DMD circuit with a proper data cable.

• If planned carefully, water cooling of Andor camera may not be a bad idea.

• The current microscope focus nob are useful but painful, if possible, piezo stage or maybe a picomotor setup as in QMS lab are recommended.

• The 3D printed mount has 0.5mm gap in between the two optics, given now the microscope is so close to those optics, it is a good idea to design a mount which have polarization wire grid and quarter wave plate touching.

Some of these suggestions involved a very radical modification, which might worth planning ahead during the Bitter coil upgrade in later years.

CHAPTER 4

FERMION MEDIATED INTERACTION: STATIC LIMIT AND SOUND PROPAGATION

4.1 Static Limit: Introduction

In high energy and condensed matter physics, particle exchange plays an essential role in the understanding of long-range interactions. For example, the exchange of massive bosons leads to the Yukawa potential [165] [166]. Phonon exchange between electrons gives rise to Cooper pairing in superconductors [149]. When a Bose-Einstein condensate (BEC) of Cs is embedded in a degenerate Fermi gas of Li, we show that interspecies interactions can give rise to an effective trapping potential, damping, and attractive boson-boson interactions mediated by fermions. The latter, related to the Ruderman-Kittel-Kasuya-Yosida (RKKY) mechanism [130], results from a coherent three-body scattering process. Such mediated interactions are expected to form novel magnetic phases [32] and supersolids [12]. We show that for suitable conditions, the mediated interactions can convert a stable BEC into a train of "Bose-Fermi solitons" [83] [133]

Interactions between cold neutral atoms are typically well-approximated by contact interactions and are characterized by a single parameter, the scattering length a. Recent experiments utilizing highly magnetic atoms [99], Rydberg atoms [10], and ground-state polar molecules [113], have stimulated great interest to probe novel quantum many-body states with long-range interactions. Examples include quantum droplets[48] [26] and lattice spin phases [66] [63] [168].

Another class of many-body systems that exhibit long range interactions are quantum mixtures in which particle interactions are mediated by interspecies scattering. Here, we consider the case of interactions between bosons mediated by a degenerate Fermi gas. In the regime that the dynamics of the fermions are much faster than those of the bosons, an

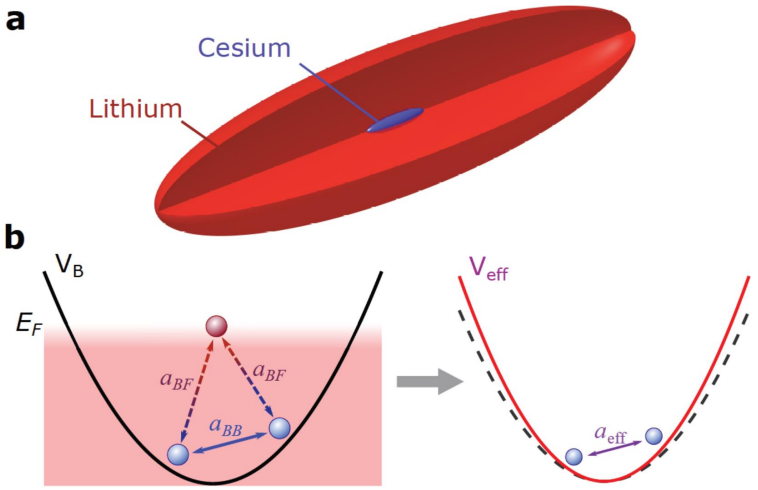

Figure 4.1: Mediated interactions between Cs atoms by exchanging Li atoms near the Fermi surface. **a** A cigar-shaped BEC of heavy Cs bosons (blue) is fully immersed in a degenerate Fermi gas of light Li atoms (red). **b** Two Cs atoms (blue balls) can interact directly with one another with scattering length a_{BB} or via secondary interactions with a Li atom (red ball) near the Fermi surface with energy E_F. By eliminating the fermionic degrees of freedom, the bosons can be described by an effective trapping potential V_{eff} and an effective scattering length a_{eff} (see text).

effective description for the bosons applies. In this case, the mediated interactions are a spinless analog of RKKY interactions [32] [146],

$$U(R) = E_{\text{F}} \frac{8k_{\text{F}}^2 a_{\text{BF}}^2}{\pi} \frac{r\cos r - \sin r}{r^4} + O(\epsilon^3), \tag{4.1}$$

where $r = 2k_F R$, R is the separation between bosons, a_{BF} is the interspecies scattering length,, $m_{B(F)}$ is the boson (fermion) mass, k_F is the Fermi wavevector. The interaction is attractive at short distance regardless of the sign of a_{BF}, and is oscillatory at long-range with the length scale of π/k_F, which corresponds to 1 μm in our experiment.

In this work, we demonstrate the effect of boson-boson interactions mediated by fermions in a degenerate Fermi gas. By using a mixture of fermionic ^{6}Li and bosonic ^{133}Cs, our system offers the tunability needed to observe the effect of such interactions, ultimately leading to the formation of a Bose-Fermi soliton train. In our system, the combination of light fermions and heavy bosons with their associated large Fermi energy E_F and small BEC

chemical potential μ_B ensures a large separation of the relevant timescales ($\sim \hbar/E_F \approx 15\mu s$ for fermions and $\sim \hbar/\mu_B \approx 500\mu s$ for bosons). Furthermore, the large mass imbalance and difference in quantum statistics allows us to prepare a BEC that is fully immersed in the degenerate Fermi gas, as shown schematically in Fig. (4.1). For zero interspecies interactions, the density of the fermions within the BEC is nearly constant. For weak interactions, one may eliminate the fermionic degrees of freedom and obtain an effective energy density functional of the bosonic field $\Psi_B(r)$, given by [151] [28] [132].

$$E = \frac{\hbar^2}{2m_B}|\nabla\psi_B(r)|^2 + V_{eff}(r)|\psi_B(r)|^2 + \frac{g_{eff}}{2}|\psi_B(r)|^4 \tag{4.2}$$

where $V_{eff}(r) = \sum_i \frac{1}{2} m_B w_{eff,i}^2 r_i^2$ is the effective potential and $r_i = x, y, z$. The effective harmonic trapping frequencies $w_{eff,i}$ and effective interaction strength $g_{eff} = 4\pi\hbar^2 a_{eff}/m_B$ satisfy the relations [151] [28]

$$w_{eff,i}^2 = w_{B,i}^2 - \frac{3}{2}\frac{n_F}{E_F}\frac{m_F}{m_B} g_{BF} w_{F,i}^2 \tag{4.3}$$

$$g_{\text{eff}} = g_{BB} - \xi\frac{3}{2}\frac{n_F}{E_F} g_{BF}^2 \tag{4.4}$$

where $w_{B(F),i}$ denote the bare harmonic trapping frequencies of the bosons (fermions) and $g_{BB} = 4\pi\hbar^2 a_{BB}/m_B$ is the boson-boson interaction strength for scattering length a_{BB}. We note that owing to the large mass imbalance and large Fermi energy in our system, Eq. 4.3 is well approximated by a linear dependence of w_{eff} on a_{BF} for all scattering lengths probed in our experiment.

The mediated interaction, described by the second term of Eq. 4.4, is a genuine three-body scattering effect with an energy $E \propto -g_{BF}^2 n_B^2 n_F$. A microscopic picture giving rise to these mediated interactions is sketched in Fig. 4.1 (b). They arise when two bosons exchange a fermion near the Fermi surface via the usual two-body s-wave scattering (dashed

lines). We note here that the mediated interactions are always attractive regardless of the sign of g_{BF}. This can be understood in the mean-field picture as follows: For repulsive interspecies interactions, fermions are repelled from the BEC, and thus the BEC feels an additional attraction towards its center where the fermion density is the lowest. On the other hand, for attractive interspecies interactions, fermions are attracted to the center of the BEC, and as a result the BEC experiences an additional attraction towards its center where the fermion density is the highest.

4.2 Effective Trap Frequencies Measurement

To observe the effective trapping frequency as well as the mediated interactions, we perform measurements at different scattering lengths a_{BB} and a_{BF} near intra- and interspecies Feshbach resonances [16] [152]. In our system, following the procedure outlined in Refs. [78] [38], we prepare quantum degenerate mixtures of 2×10^4 Li and 3×10^4 Cs atoms in their absolute ground state at magnetic field $B \approx 900G$. Both species are radially trapped in a single laser beam and weakly confined magnetically in the x-direction.

To measure the effective harmonic trapping frequency, we excite dipole oscillations of the Cs BEC along the weakly trapped axis [45] [47] [129]. In the absence of Li, we observe long-lived oscillations with a decay time of $\approx 30\mu s$ (see Fig. 4.2). This low background damping rate allows us to precisely determine the trapping frequency of the Cs.

In the presence of Li, we observe small shifts in the oscillation frequency ω_{eff} and enhanced damping Γ as a_{BF} deviates from zero (see Fig. 4.2b). In the range of $-100a_0 < aBF < 500a_0$, we observe a linear dependence of the frequency of the oscillation on the scattering length a_{BF} (see Fig. 4.2 c). A fit to the data in this range shows a negligible shift $< 0.1\%$ at $aBF = 0$ and a slope of $-0.22(2)mHz/a_0$ in fair agreement with prediction of $-0.18mHz/a_0$ from Eq. 4.3 . Outside this range, a non-linear behavior develops. The frequency shifts first reduce toward the bare Cs frequency and then, for very large $|a_{BF}|$,

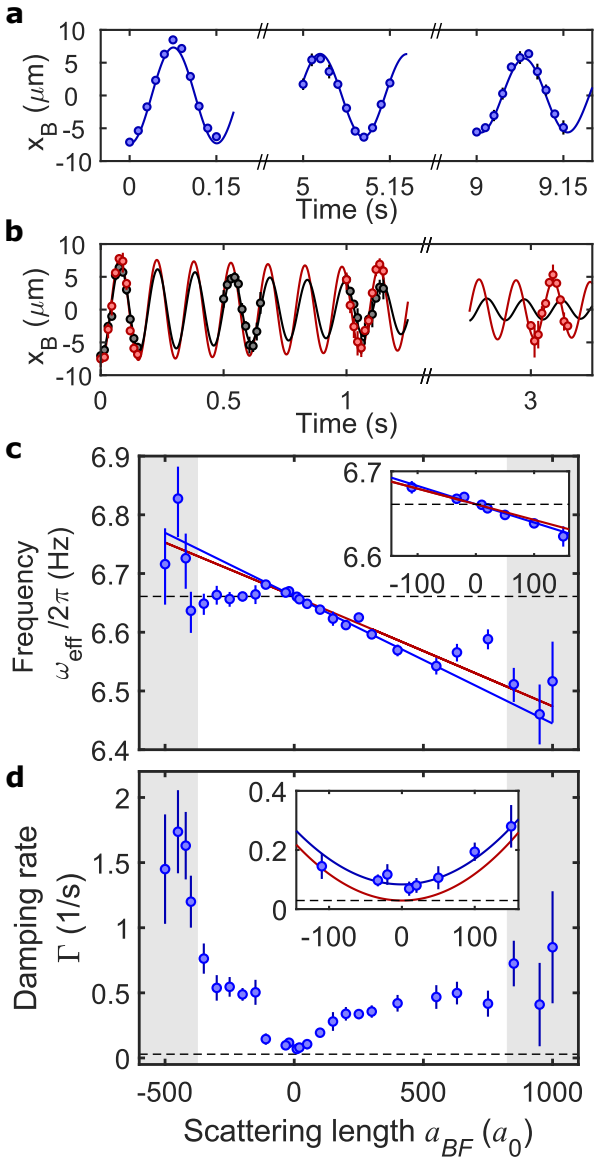

Figure 4.2: Dipole oscillations of a Cs BEC immersed in a Li degenerate Fermi gas. **a** Without Li present, we observe long lived dipole oscillations along the weakly confined x-axis. The data is well described by damped harmonic oscillation with very low damping $\Gamma < 1/30\mu s$ (blue line). **b** When the BEC is embedded in the Fermi gas, a shift in the oscillation frequency as well as an increase of the damping are observed. Example traces are shown for $a_{BF} = 100a0$ (red) and $a_{BF} = 630a0$ (black). **c** Oscillation frequency and **d** damping rate of the BEC. For small $|a_{BF}|$, the data is well fit by linear and quadratic curves (blue lines) and are consistent with the predictions (red lines), see Eq.4.3 and Methods. Shaded areas show the magnetic field ranges with significant heating where the BEC is heated into a normal gas. Frequency and damping of a bare Cs BEC (dashed lines) serve as references for comparison.

the BEC is heated to a normal gas due to recombination loss (see shaded area in Figs. 4.2 c and d), and displays even larger shifts. Such non-linear behavior at large aBF shows the breakdown of the mean-field theory and demands further theoretical investigation.

The damping of dipole oscillations shows interesting behavior as well. For small scattering lengths, collisions between the BEC and the Fermi gas are scarce, and yield a weak friction that damps the oscillation. The damping is expected to be proportional to the collisional crosssection $\approx a_{BF}^2$ [46] [98]. In the range of $-100a_0 < a_{BF} < 100a_0$, our data agree well with the prediction $\Gamma = \kappa a_{BF}^2$ (see inset of Fig. 4.2d and Methods). A fit to the data in this range yields a curvature of $\kappa = 8.5(2.1) \times 10^{-6}/s \cdot a_0^2$, which excellently agrees with the prediction of $\kappa = 9 \times 10^{-6}/s \cdot a_0^2$. At large scattering lengths, the damping appears to saturate and then increases again when the sample is heated to a normal gas. While a more complete model is needed to describe the motion of a BEC strongly interacting with a degenerate Fermi gas, we note that for small scattering lengths ($|a_{BF}| < 100a_0$), the mean-field theory offers very good quantitative predictions.

4.3 Effective Interaction Measurement

To measure the mediated interactions, we first characterize the bare scattering length of the Cs atoms based on the equilibrium Thomas-Fermi radius $R_{TF} \propto \frac{1}{\omega_x}(N_0 a_{BB})^{1/5}$ in the weakly confined axis, where N_0 is the number of atoms in the BEC. In the relevant range of magnetic field the scattering length is approximately linear with a zero crossing at B = 880.29(8) G, as shown in Fig. 4.3. Our result is in good agreement with the calculation in Ref. [16].

Armed with the calibrated scattering length, we next determine the effective scattering length of the BEC embedded in the degenerate Fermi gas. Since the mediated interactions are weak, we perform the measurement in the range of $|a_{BB}| \ll |a_{BF}|$ to enhance the effect. We measure the change in the scattering length by directly comparing the BEC radius R_{TF}

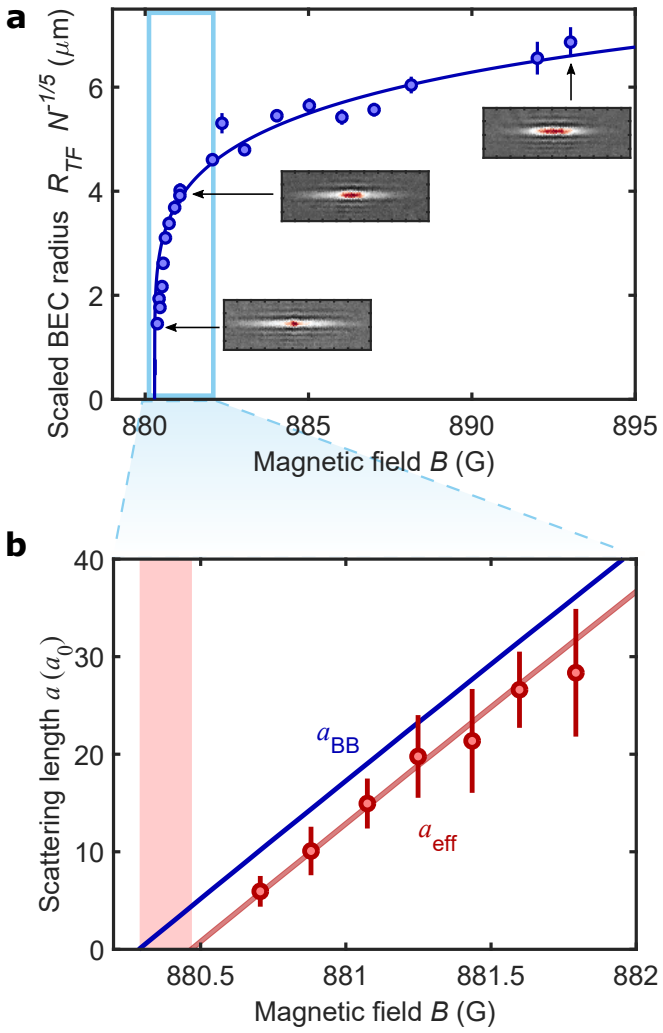

Figure 4.3: Bare and effective Cs-Cs scattering length. (**a**) We measure the in situ Thomas-Fermi radius $R_{TF}$of a Cs BEC in the weakly confined direction. Without Li in the trap (blue circles), we find good agreement with theory when scaled appropriately to the number of atoms in the BEC (blue line). Characteristic images from the measurement are shown as insets. (**b**) At small a_{BB}, we perform a relative measurement of R_{TF} with and without Li present to extract the effective scattering length a_{eff} (red circles). Our result is consistent with a small negative offset from a_{BB} (blue line) indicating attractive mediated interactions. A fit to the data (red line) yields fair agreement with theory (see text).

with and without the degenerate Fermi gas present near the zero crossing $a_{BB} = 0$. We find that the size of the BEC is systematically smaller when Li is present, which is consistent with attractive mediated interactions (see Fig. 6). From our relative measurements, the effective scattering length a_{eff} displays a negative and constant offset from the bare Cs scattering length throughout the measured range (see Fig. 4.3b). The fitted offset is -4.4(3)(1.5)a_0, where the first and second uncertainties are statistical and systematic, respectively. Together with the known constant $a_{BF} = -60a_0$ [152], the measured offset yields a value of $\xi = 1.7(6)$ in Eq. 4.4, in fair agreement with the calculations in Refs. [151] [28] [132]. The large deviation of our result from Ref. [32] is likely because our experiment is not in the dilute limit assumed in the calculation.

4.4 Bose-Fermi Soliton

These mediated interactions look minute, but can have a profound effect on the ground state of the Cs atoms. Labeled as the red shaded area in Fig 4.3b, in particular, when a_{BB} is small and positive, the mediated interactions can cause a_{eff} to become negative. As an harmonically trapped BEC with attractive interactions can experience dynamic instability and collapse [31], one expects that in this regime, the mediated interactions can render the BEC unstable as well. In our highly elongated trap, the BEC enters the quasi-1D regime for scattering lengths $a_{BB} < 4\ a_0$, and Bose-Fermi soliton trains are predicted to form in this regime with sufficiently strong fermion-mediated attraction between bosons [83] [133]. In our slow ramp experiments, we observe very large shot to shot fluctuations of the shape and size of the cloud in this region, indicating the onset of the instability.

To probe the fermion-mediated instability, we perform a dynamic experiment by suddenly jumping the scattering length from a large positive value to values near the zero crossing of a_{BB} (see Fig. 4.4 and Methods). In situ images taken $75ms$ after the quench show a qualitative difference for a bare Cs BEC and for a BEC embedded in the degenerate Fermi

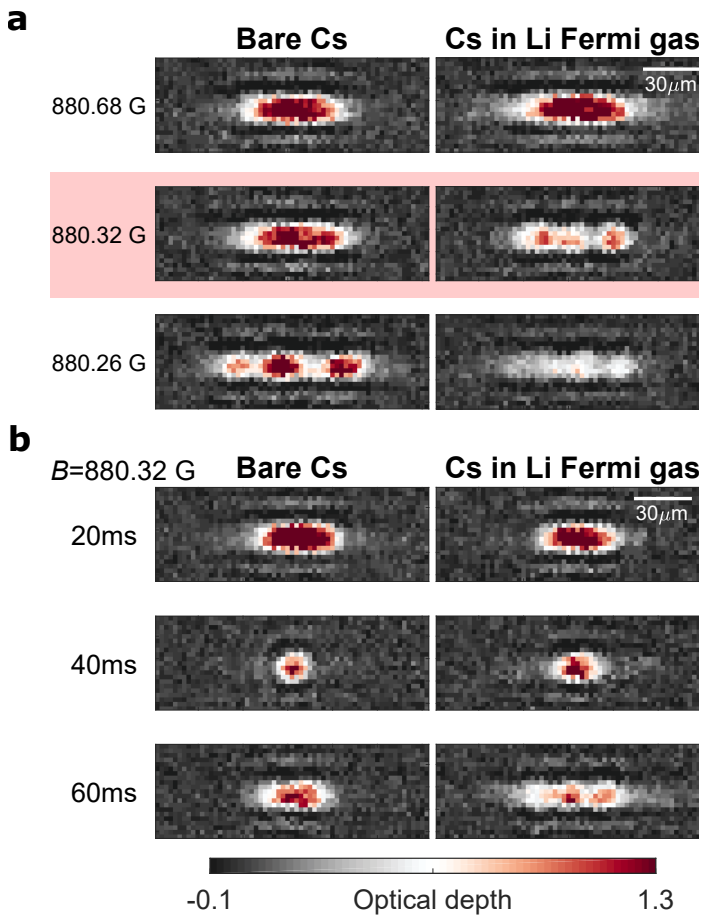

Figure 4.4: Formation of Bose-Fermi solitons. **a** In situ images of a Cs BEC 75 ms after a quench from B = 885.5 G ($a_{BB} = 120a_0$) to lower fields indicated on the left. For positive a_{eff}, there is no qualitative difference when Li is added to the system. When a_{eff} becomes negative, the BEC collapses into a train of solitons with Li present, but remains stable without Li as shown for B = 880.32 G in the shaded red panels. For $a_{BB} < 0$, the BEC collapses with and without Li present. **b** Time sequence of the induced collapse at B = 880.32 G. Without Li present, the BEC undergoes breathing oscillations. With Li, the BEC first shrinks to a small size and afterwards breaks up into a train of solitons.

gas. In the absence of Li, we observe the typical formation of a soliton train for a final magnetic field below $B \approx 880.26G$, where $a_{BB} < 0$.

In the presence of Li, we observe a collapse below $B \approx 880.34G$, where $a_{BB} > 0$. This observation is consistent with the results shown in Fig. (4.3) that at this field the effective scattering length is negative $a_{\text{eff}} < 0$ and thus the stability of the BEC has been compromised. The observed soliton train is likely comprised of correlated bosonic and fermionic density waves [83] [133]. However, we could not see a clear density modulation of the Fermi gas due to limited signal-to-noise of our measurement. The induced collapse in this interesting regime is further supported by the time evolution of the BEC following a quench. After preparing the sample at $B = 885.5$ G where $a_{BB} = 120\ a_0$, we abruptly change the field to 880.32 G, where the effective scattering length is expected to be negative $a_{\text{eff}} < 0$, and monitor the subsequent dynamics of the BEC. Without the Fermi gas $a_{BB} > 0$ the BEC undergoes breathing oscillations without qualitative changes in the structure of the cloud. With Li present, the BEC first contracts as if starting a breathing oscillation, however, upon expansion, the BEC is fractured into a train of of 3 to 4 solitons. This observation clearly indicates that the fermion-mediated interactions can destablize a weakly-interacting BEC. In other words, the ground state of the bosons can be altered by the fermion-mediated interactions.

While the fermion-mediated interactions amount to only an effective change of the scattering length by $-4\ a_0$ in our experiment, the scaling of the mediated interaction $a_{BF}^2 n_B^2 n_F$ suggests strong influence on systems near an interspecies Feshbach resonance as well as in systems with high local density, for example, in an optical lattice. This promises exciting future work exploring the long-range nature of such interactions to ultimately probe novel quantum phases beyond contact interactions.

4.5 Introduction: Sound Propagation in Bose-Fermi Mixture

Particle-like excitations, or quasi-particles, emerging from interacting fermionic and bosonic quantum fields underlie many intriguing quantum phenomena in high energy and condensed matter systems. Computation of the properties of these excitations is frequently intractable in the strong interaction regime. Quantum degenerate Bose-Fermi mixtures offer promising prospects to elucidate the physics of such quasi-particles. In this work, we investigate phonon propagation in an atomic Bose-Einstein condensate immersed in a degenerate Fermi gas with interspecies scattering length a_{BF} tuned by a Feshbach resonance. We observe sound mode softening with moderate attractive interactions. For even greater attraction, surprisingly, stable sound propagation re-emerges and persists across the resonance. The stability of phonons with resonant interactions opens up opportunities to investigate novel Bose-Fermi liquids and fermionic pairing in the strong interaction regime.

Interactions between excitations of bosonic and fermionic quantum fields play an important role in understanding fundamental processes in high energy and condensed matter physics. In quantum electrodynamics, for example, the coupling between the photon and virtual electron-positron pairs polarizes the vacuum, which contributes to Lamb shifts [95] and the anomalous magnetic moments of the electron and the muon [136]. In condensed matter, interactions between phonons and electrons are central to Cooper pairing in conventional superconductors [11], as well as charge ordering and superconductivity in strongly correlated materials [59, 91].

Ultracold mixtures of atomic Bose and Fermi gases offer a complementary experimental platform for elucidating these quantum phenomena. Cold atoms are exceptionally flexible, allowing for the control of interactions between the atomic species using Feshbach resonances [24]. These capabilities have been used to study phase transitions in lattices [64, 117, 147], polarons [163, 51], and superfluid mixtures [34, 129]. Many exciting theoretical predictions for quantum simulation remain to be tested, e.g. Refs. [122, 137, 30].

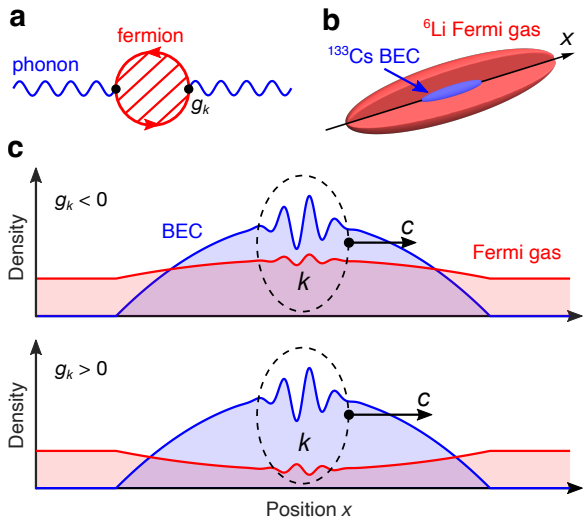

Figure 4.5: Bosonic quasi-particles (phonons) coupled to a fermionic quantum field. (a) Diagrammatic representation of phonons (blue) coupled to excitations of a fermionic field (red). The lowest order diagram contains a single loop and is second order in the phonon-fermion coupling g_k. Higher order corrections are indicated by the hatched area. (b) In our experiment, a cigar-shaped Bose-Einstein condensate (BEC) of cesium-133 is immersed in a much larger degenerate Fermi gas of lithium-6. (c) As a phonon with momentum k (black dashed ellipse) propagates, the coupling results in the density modulation of both species and the modification of the sound speed c.

In this work, we investigate sound propagation in a quantum degenerate Bose-Fermi mixture from the weak to the strong interaction regime. We optically excite density waves in the gases and measure their velocities and damping rates from *in situ* images of the Bose-Einstein condensate (BEC). We see significant changes in the speed of sound for interspecies attraction and negligible shifts for repulsion. This asymmetry indicates strong deviation from the perturbation prediction. Intriguingly, we find stable propagation of sound waves in mixtures with resonant interspecies interactions. This observation offers promising prospects to explore new quantum phases of Bose-Fermi mixtures in the strong interaction regime.

The Hamiltonian for the phonons coupled to a single-component Fermi gas is given by [100, 41]

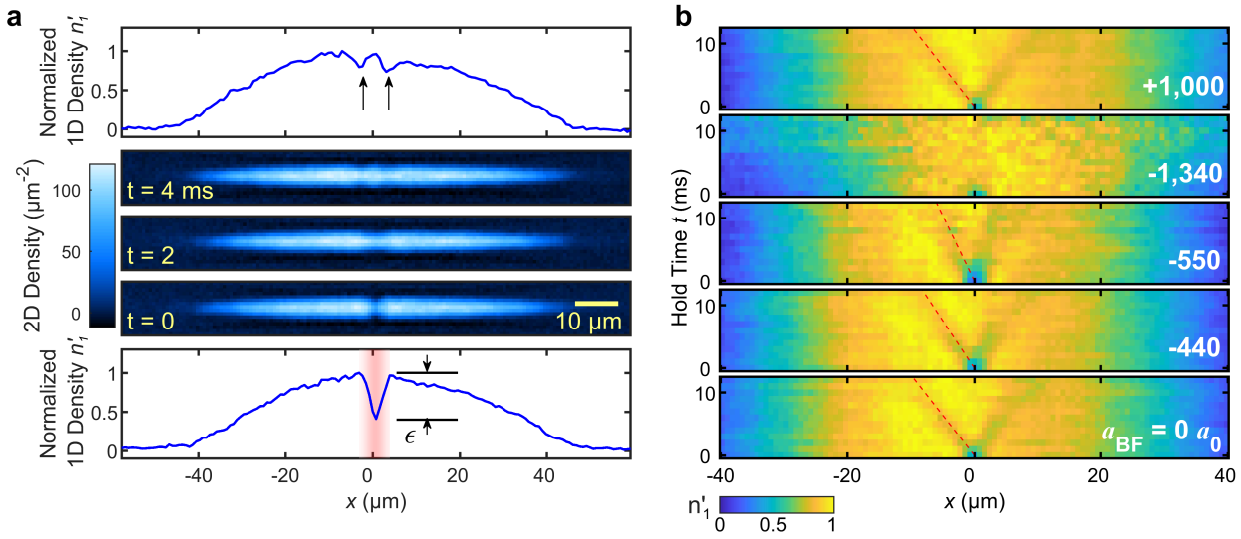

Figure 4.6: *In situ* imaging of the phonon propagation. (a) A local density depletion ϵ is created in the center of the cesium BEC by a projected laser beam (bottom panel, red shaded area). The optical potential is abruptly switched off at $t = 0$ and the density dip splits into density waves propagating in opposite directions (top panel, black arrows). Average column densities are shown for three values of the hold time $t = 0, 2, 4$ ms along with sample normalized one-dimensional (1D) densities n_1' for $t = 0$ ms and $t = 4$ ms. Data is shown for the Cs-Li Bose-Fermi mixture with interspecies scattering length $a_{\mathrm{BF}} = -335\, a_0$. (b) Normalized 1D densities n_1' show density wave dynamics for mixtures prepared at various interspecies scattering lengths. Red dashed lines are a guide to the eye.

$$H = \sum_k \epsilon_k^{\mathrm{F}} c_k^\dagger c_k + \sum_k \hbar\omega_k \alpha_k^\dagger \alpha_k + \sum_{k,q} g_k(\alpha_k + \alpha_{-k}^\dagger) c_q^\dagger c_{q-k}, \tag{4.5}$$

where ϵ_k^{F} is the dispersion of the fermions, $\hbar$ is the reduced Planck's constant, ω_k is the phonon dispersion, g_k is the phonon-fermion coupling constant, c_k and α_k refer to fermion and phonon annihilation operators respectively, and k and q are momenta (see Fig. 1a). In our degenerate Bose-Fermi mixture, the kinetic energy of a bare fermion is $\epsilon_k^{\mathrm{F}} = \hbar^2 k^2/2m_{\mathrm{F}}$, where m_{F} is the fermion mass. The bare phonons are low energy excitations of the BEC with the Bogoliubov dispersion [123] $\omega_k \approx c_0 k$, where the sound velocity $c_0 = \sqrt{g_{\mathrm{BB}} n_{\mathrm{B}}/m_{\mathrm{B}}}$ is determined by the boson-boson coupling constant g_{BB}, condensate density n_{B}, and boson mass m_{B}. The phonon-fermion coupling constant is $g_k = g_{\mathrm{BF}}\sqrt{n_{\mathrm{B}}\hbar k^2/2m_{\mathrm{B}}\omega_k}$ [41**?**], where $g_{\mathrm{BF}} = 2\pi\hbar^2 a_{\mathrm{BF}}/m_r$ is the interspecies coupling constant, a_{BF} is the interspecies scattering length and m_r is the reduced mass of the two unlike atoms. The phonon-fermion coupling g_k can thus be tuned by controlling a_{BF} using an interspecies Feshbach resonance (see Fig. 1c).

Perturbation theory shows that the velocity of phonons is reduced when the BEC interacts weakly with the Fermi gas. This can be understood as a result of a fermion-mediated interaction between bosons analogous to the Ruderman-Kittel-Kasuya-Yosida mechanism [131, 33]. The mediated interaction has been observed in cold atom experiments [36, 39]. To leading order in g_{BF}, the sound velocity is predicted to be [164]

$$c = c_0\sqrt{1 - \frac{3}{2}\frac{g_{\mathrm{BF}}^2}{g_{\mathrm{BB}}}\frac{n_{\mathrm{F0}}}{E_{\mathrm{F0}}}}, \tag{4.6}$$

where n_{F0} and E_{F0} are the density and Fermi energy of the Fermi gas in the absence of the condensate. This correction is quadratic in the coupling strength g_{BF}, and corresponds to the one-loop diagram shown in Fig 1a. The sound speed is expected to be reduced regardless of the sign of the interspecies coupling strength g_{BF}. The perturbation result is valid in the

weak coupling regime $|g_{\mathrm{BF}} n_{\mathrm{B}}| \ll E_{\mathrm{F0}}$.

At stronger interactions, the density profile of each species can be significantly modified by the other species. This effect can be captured in a mean-field model. Under the Thomas-Fermi approximation for both species, the local mean-field chemical potential of the bosons depends on the fermion density as [?]

$$\mu_{\mathrm{TF}} = g_{\mathrm{BB}} n_{\mathrm{B}} + g_{\mathrm{BF}} n_{\mathrm{F0}} \left(1 - \frac{g_{\mathrm{BF}} n_{\mathrm{B}}}{E_{\mathrm{F0}}}\right)^{3/2}, \tag{4.7}$$

where the second term is set to zero when the mean-field interaction energy exceeds the Fermi energy, $g_{\mathrm{BF}} n_{\mathrm{B}} > E_{\mathrm{F0}}$. In our system, it is a good approximation that the light fermions (Li) follow the heavy bosons (Cs) adiabatically. This permits the evaluation of the mean-field sound speed $c = \sqrt{n_{\mathrm{B}}/m_{\mathrm{B}}\kappa}$ in terms of the effective compressibillity $\kappa = \partial n_{\mathrm{B}}/\partial \mu_{\mathrm{TF}}$ as

$$c = c_0 \sqrt{1 - \frac{3}{2} \frac{g_{\mathrm{BF}}^2}{g_{\mathrm{BB}}} \frac{n_{\mathrm{F0}}}{E_{\mathrm{F0}}} \sqrt{1 - \frac{g_{\mathrm{BF}} n_{\mathrm{B}}}{E_{\mathrm{F0}}}}}. \tag{4.8}$$

Compared to Eq. (2), the additional factor in Eq. (4) captures the density changes in the mixture caused by interspecies interactions.

4.6 Measurement of Sound speed Shift

Our experiments begin with mixtures of a pure BEC of 30,000 ^{133}Cs atoms and a degenerate Fermi gas of 8,000 ^{6}Li atoms, each prepared in their lowest internal state [37]. The mixture is trapped in a single beam optical dipole trap at wavelength 1064 nm with trap frequencies $\omega_{\mathrm{Cs}} = 2\pi \times (6.53, 100, 140)$ Hz and $\omega_{\mathrm{Li}} = 2\pi \times (36, 330, 330)$ Hz in the axial and two transverse directions. The bosons and fermions have a temperature of about 30 nK and chemical potentials of about $k_{\mathrm{B}} \times 30$ nK and $k_{\mathrm{B}} \times 300$ nK respectively, where k_{B} is the Boltzmann constant. In the dipole trap, the BEC is fully immersed in the degenerate Fermi gas (see Fig. 1b). We tune the interspecies scattering length near a narrow Feshbach resonance at

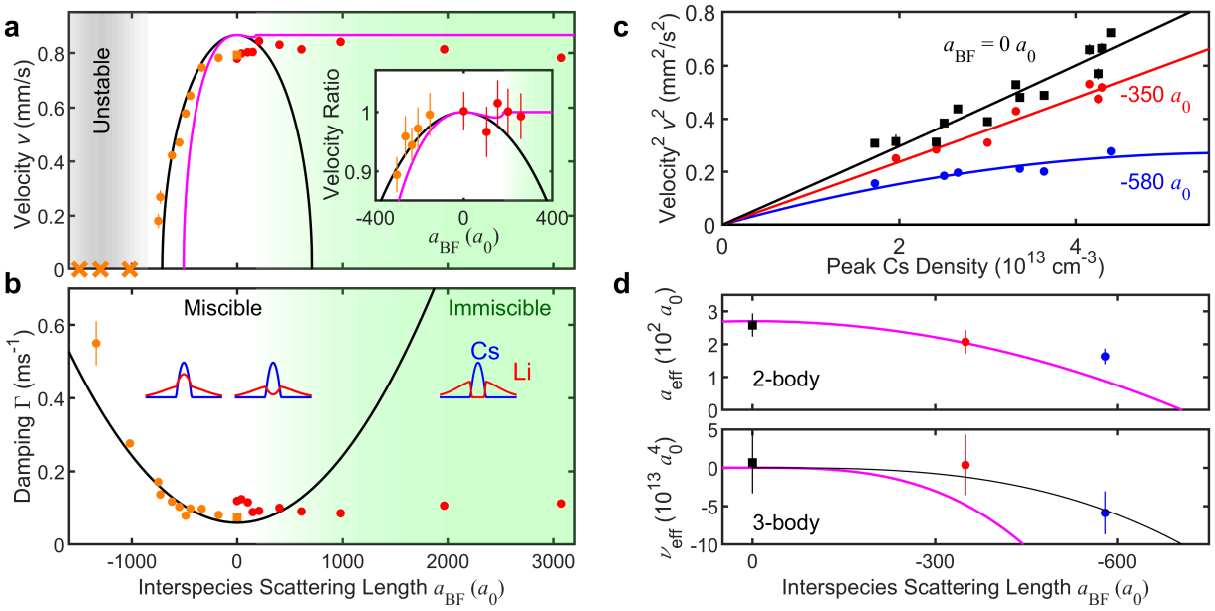

Figure 4.7: Sound wave dynamics in Bose-Fermi mixtures with tunable interspecies scattering length a_{BF}. (a) Orange data points indicate samples prepared on the attractive side of the Feshbach resonance $a_{\mathrm{BF}} < 0$. Measurement for a pure BEC is shown as the orange square. Red data points are prepared on the repulsive side with $a_{\mathrm{BF}} > 0$. The crosses indicate samples with no stable sound propagation. Inset shows the ratio of density wave velocities for samples prepared with and without the fermions. The ratios are obtained from the separation of density waves after 8 ms hold time. Calculations from perturbation (black line) and mean-field (magenta line) theory are shown for comparison. The green shaded area represents the phase separation region. The grey area indicates the region where no stable sound propagation is observed. (b) Damping rates of the density waves are compared with the perturbative prediction (black line) evaluated for momentum $k = 2\pi/(4\mu\mathrm{m})$ [**?**]. Insets: Cartoon representation of the Cs (blue) and Li (red) density profiles in different regimes. (c) Density wave velocity for BECs prepared without the Fermi gas (black squares) and with the Fermi gas at $a_{\mathrm{BF}} = -350\,a_0$ (red circles) and $a_{\mathrm{BF}} = -580\,a_0$ (blue circles). Lines are fits of the data to a model with both two- and three-body effective interactions between bosons (see text). (d) Colored circles are the effective scattering lengths and hypervolumes extracted from panel (c). The magenta lines are the mean-field predictions and the black line is a cubic fit to the data. The error bars in (a)-(c) are standard errors calculated from fits to averaged experimental density profiles. The error bars in (d) are standard errors calculated from fits to the data in panel (c).

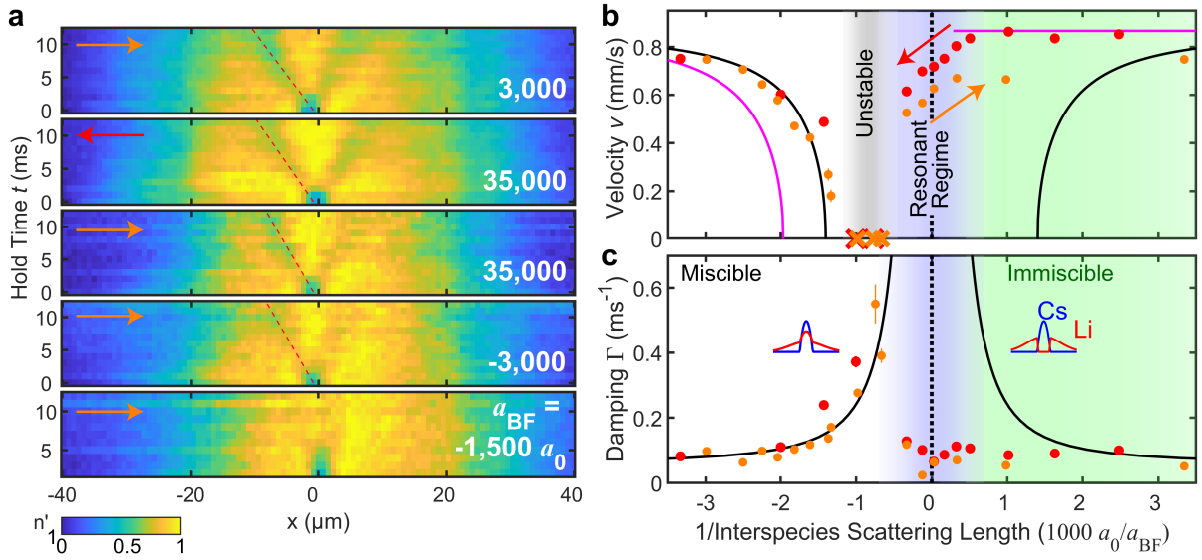

Figure 4.8: Sound propagation across the Feshbach resonance. (a) Normalized 1D densities illustrating the revival of sound propagation at strong interactions. The arrows on each data set indicate whether the system is ramped towards the resonance starting from the attractive side (orange arrow) or repulsive side (red arrow). (b) Density wave velocity of the Li-Cs mixture across the Feshbach resonance. Data taken from samples prepared on the attractive (repulsive) side are orange (red) in color. The arrows indicate the direction of the scattering length ramp. The blue and green regions indicate the resonant and phase separation regimes respectively. The vertical black dotted line indicates the position of the Feshbach resonance. (c) Damping from the same data set. The black and magenta lines are the same perturbation and mean field predictions as shown in Fig. 3. All shown error bars are standard errors calculated from fits to averaged experimental images.

magnetic field 892.65 G [152, 80]. Across the resonance, the boson-boson interactions are moderately repulsive with a nearly constant scattering length $a_{\mathrm{BB}} = 270\ a_0$ [16], where a_0 is the Bohr radius. At these temperatures, the interactions between the single component Li atoms are negligible. In our experiment, the mixture is in the weak coupling regime when the interspecies scattering length is $|a_{\mathrm{BF}}| < 200 a_0$.

To study sound propagation in our system, we optically excite density waves in the mixture [126, 6, 82]. We introduce a narrow repulsive potential barrier of width $\delta = 4\ \mu m$ by projecting blue-detuned light onto the center of the BEC, resulting in a density dip. At

time $t = 0$ we suddenly turn off the repulsive barrier and record the dynamics of the density waves *in situ* [**?**]. We observe that the initial density depletion splits into two density waves that counter-propagate at the same speed along the axial direction (see Fig. 4.6a). From the images, we extract the velocity v and damping rate Γ of the density waves. We repeat the experiment at different interspecies interaction strengths (see Fig. 4.6b).

The density wave velocity v in a bare elongated condensate is given by the sound speed c_0 through [88]

$$v \approx \frac{c_0}{\sqrt{2}}\sqrt{1 - \frac{\epsilon}{2}}, \tag{4.9}$$

where ϵ is the initial density depletion due to the potential barrier (see Fig. 2a) and c_0 is the sound speed at the center of the BEC.

In the presence of fermions, we measure the dependence of the density wave velocity on the initial density depletion ϵ and find agreement with Eq. (5). Thus, we adopt Eq. (5) to link the density wave velocity to the sound speed. In the following experiments, the initial density depletion is set to $\epsilon = 0.5$.

We summarize the measured density wave velocities and damping rates in Figs. 3a and 3b. As we increase the interspecies attraction from zero, the density waves propagate slower and decay faster. The enhanced damping of the density waves is consistent with the perturbation calculation for a zero-temperature Bose-Fermi mixture [100**?**]. When the scattering length exceeds the critical value of $a_c = -790(10)\, a_0$, we no longer observe stable propagation of sound. Our finding is consistent with the sound mode softening in the Bose-Fermi mixture with increasing attraction. Our measured critical value shows clear deviations from the perturbation prediction $-710\, a_0$ and the mean field prediction $-510\, a_0$ for the collapse of the mixture [109].

For repulsive interspecies interactions, on the other hand, the density waves propagate with low damping and no significant change in velocity over the range we explore (see Figs. 3a

and 3b). This is in stark contrast to our observations for attraction. The clear asymmetry with respect to the sign of the interaction goes beyond the perturbation prediction, see Eq. (2), which only depends on the square of the scattering length a_{BF}^2.

The asymmetry can be understood from the mean-field picture. For attractive interactions, fermions are pulled into the BEC, and the higher fermion density further reduces the sound velocity. On the other hand, for repulsion, fermions are expelled from the BEC, reducing their effect on the sound propagation. For strong enough repulsion, the bosons and fermions are expected to phase separate [109, 158, 98]. The observed nearly constant sound velocity for strong repulsion is consistent with the picture that most fermions are expelled from the condensate. For our system, the mean field model predicts phase separation near the scattering length $a_{\mathrm{BF}} \approx 180\, a_0$.

This asymmetry comes fundamentally from effective few-body interactions in the BEC that go beyond the perturbation calculation [14, 42]. The change of the density overlap, described in the mean-field picture, is a consequence of the few-body interactions. The three-body interaction strength can be experimentally characterized by writing the chemical potential in orders of the boson density

$$\mu = g_2 n_{\mathrm{B}} + g_3 n_{\mathrm{B}}^2 + ..., \tag{4.10}$$

where $g_2 = 4\pi\hbar^2 a_{\mathrm{eff}}/m_{\mathrm{B}}$ and $g_3 \equiv \hbar^2 \nu_{\mathrm{eff}}/m_{\mathrm{B}}$ are effective two- and three-body coupling constants between bosons, a_{eff} is the effective scattering length, and ν_{eff} is the effective scattering hypervolume. From the effective chemical potential μ we obtain the sound speed as $c \approx \sqrt{(g_2 n_{\mathrm{B}} + 2 g_3 n_{\mathrm{B}}^2)/m_{\mathrm{B}}}$.

To determine the effective two- and three-body interaction strengths, we measure the density wave velocity at various boson densities and scattering lengths. The results are shown in Fig. 4.7c. From fits to the density wave velocities and Eqs. (5) and (6), we extract the effective scattering length a_{eff} and effective scattering hypervolume ν_{eff} (see Fig. 3d).

As the interspecies attraction increases, we observe a reduction of the effective scattering length, consistent with Ref. [36], and an emerging scattering hypervolume. Mean-field theory predicts $\nu_{\text{eff}} = \lambda a_{\text{BF}}^3$ with $\lambda \approx 159 k_{\text{F}}^{-1}$ set by the Fermi momentum and mass ratio [**?**]. Fitting the data, we determine $\lambda = 35(8) k_{\text{F}}^{-1}$, see Fig. 3d. This value shows clear deviation from the mean field prediction. Notably, the three-body interaction $g_3 n_{\text{B}}^2 \propto a_{\text{BF}}^3$ is the leading order process that breaks the symmetry between positive and negative scattering length.

4.7 Sound Mode Revival

By ramping our magnetic field across the Feshbach resonance, we explore the sound propagation in the strong interaction regime, where the scattering length exceeds all length scales in the system. Surprisingly, we observe stable sound propagation with low damping for all scattering lengths $|a_{\text{BF}}| > 3,000\, a_0$ (see Fig. 4) regardless of which side of the resonance the samples are initially prepared on. We label this range the resonant regime. An example of the sound propagation with $a_{\text{BF}} = 35,000\, a_0$ is shown in Fig. 4.8a. An interesting scenario occurs when we approach the resonance from the attractive side: the sound propagation first becomes unstable beyond the critical value a_{c}, and then recovers its stability at $a_{\text{BF}} = -3,000\, a_0$ as the system enters the resonant regime.

The stable sound propagation we observe across the interspecies Feshbach resonance goes beyond the mean-field picture and offers promising prospects for future discoveries in the strong-coupling regime. At strong interactions, mean-field corrections are predicted to support a novel quantum liquid phase for scattering lengths $a_{BF} < -750\, a_0$ [124]. An Efimov resonance observed at the scattering length $a_{\text{BF}} = -3,330\, a_0$ [80] could also provide three-body interactions that stabilize sound propagation in the resonant regime [**?**]. Finally, at strong coupling, p-wave fermionic superfluidity is conjectured when fermions are paired through the exchange of bosonic excitations [41, 137, 93], which we estimate would occur in

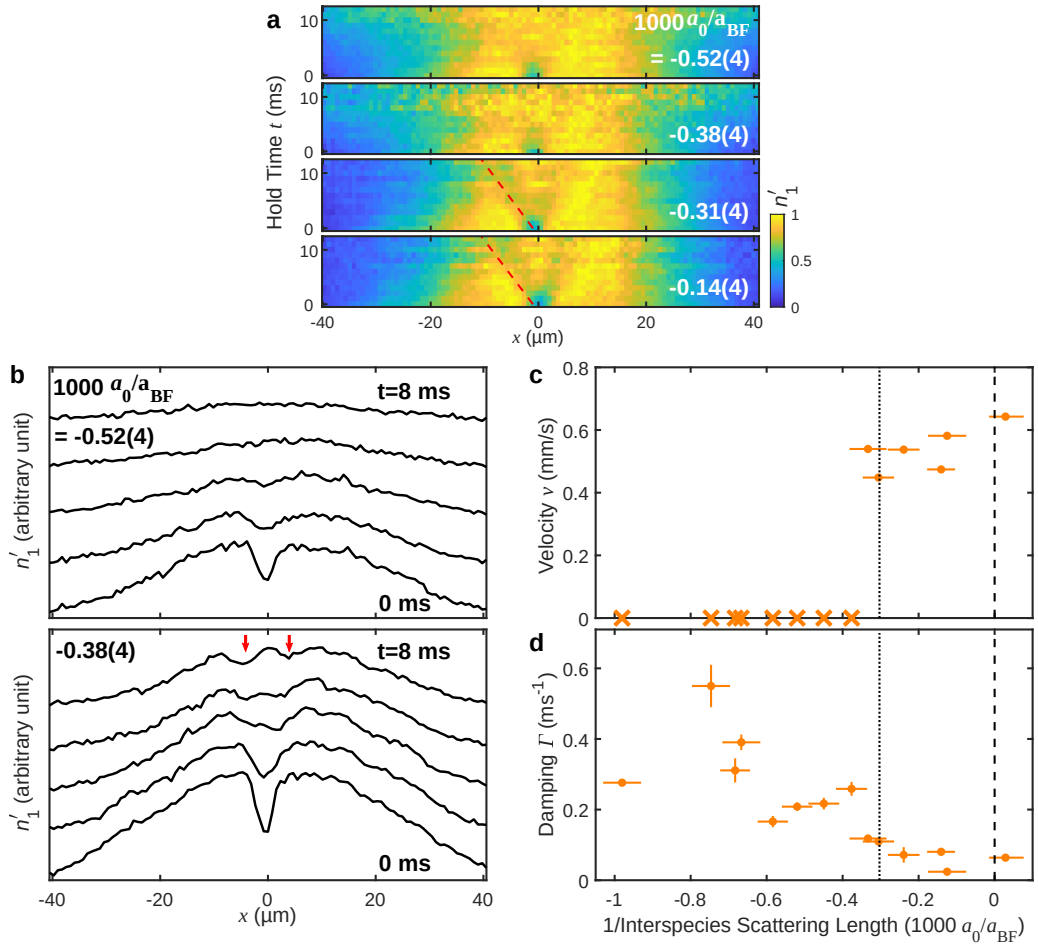

Figure 4.9: Zoomed in fine scanning of the position for sound propagation re-emergence. (a) Normalized 1D densities illustrating the revival of sound propagation between $1000\,a_0/a_{\mathrm{BF}} = -0.38$ and -0.31 based on the same experimental procedure as in Figs. 4.7 and 4.9. For all data, the system is prepared on the attractive side of the Feshbach resonance and switched to the target magnetic field. Red dashed lines are guides to the eye. (b) Normalized 1D densities at $t = 0$, 2, 4, 6, and 8 ms after the onset of density wave dynamics. In the data at $1000\,a_0/a_{\mathrm{BF}} = -0.38$, two clearly separated density depletions are visible at later times (red arrows), whereas no such structure is visible in the data at $1000\,a_0/a_{\mathrm{BF}} = -0.52$. (c) Density wave velocity near the Feshbach resonance. The crosses indicate samples with no stable sound propagation. (d) Damping from the same data set. The vertical error bars in panels (c)-(d) are standard errors from fits to averaged density profiles. The horizontal error bars represent 1-σ uncertainties of the scattering length (see Section A). The vertical dashed line shows the position of the Feshbach resonance. The vertical dotted line shows the position of the Efimov resonance reported in Ref. [78].

our system in the range $a_{\mathrm{BF}} = -2,000\,a_0$ to $-10,000\,a_0$. The stable phonon propagation we observe near the Feshbach resonance offers promising prospects to explore these intriguing physics with strongly interacting Bose-Fermi mixtures.

We perform additional sound speed measurements to determine the precise conditions for the re-emergence of sound propagation. Based on similar experimental conditions as in Fig. 4 and magnetic field control at higher resolution, we observe a stark re-emergence of the sound propagation between $a_{\mathrm{BF}} = 2600\,a_0$ and $3200\,a_0$ ($1000\,a_0/a_{\mathrm{BF}} = -0.38$ and -0.31) based on the criterion described in Sec. C, see Fig. S8. The transition is very close to the position of the Efimov resonance at $a_{\mathrm{BF}} = -3300\,a_0$ ($1000\,a_0/a_{\mathrm{BF}} = -0.30$) [78]. Future investigation is needed to determine the role of the Efimov resonance in the re-emergence of the sound propagation.

CHAPTER 5

BOSE-FERMI MIXTURE WITH STRONG COUPLING

Linear approximation and perturbation theories are the basic building blocks of modern physics. In fact, once the story goes beyond these regimes, the picture immediately becomes rather complicated. Such examples ranges from classical mechanics of Navier-Stokes equation in highly turbulent regime, non-Fermi liquid, high temperature super conductor to the study of strong interaction in the standard model. Owing to the ubiquitousness and unique properties in these problems, as well as their accompanying theoretical difficulty, physics in the strong coupling regime remains one of most focused frontiers of modern physics research.

These theoretical interests applies to the Atomic Molecular Optical physics, or at least, the quantum simulation community as well. For decades, experimentalists have been trying to study unresolved question in other physical systems. Ranging from black hole radiation [69], quantum chemistry [169] to the study of Efimov physics [78]. Cold atom platforms come with its clean and easy to control features, though, sometimes it is hard to study many-body physics in strongly correlated regimes. This difficulty originates from the very basic layer of its interaction: for most cold atom systems, their interaction range is very small compared to their atomic separation, hence the interaction can be regarded as contact interaction or near neighbor interaction. In fact, this feature is necessary for most of the time to ensure the lifetime and feasibility of experimental cold atom systems. On the other hand, it greatly ease theoretical difficulty yet make it hard to engineer a Hamiltonian of a strong correlated system. Despite this being true in LiCs system, we try to explore the strongly interacting regime. As demonstrated in sound speed study, we quench Bose-Fermi mixtures to somewhere near the inter-species Feshbach resonance and observed dramatic change in their sound speed. Especially the revival of sound mode near the Feshbach resonance is a surprise which inspired a lot of speculations in the LiCs team. The BEC immersed in Fermi gas starts to be unstable from $a_{BF} \approx -800a_0$ and suddenly revives right near the Feshbach

resonance, which made us wonder what's the relation between experimental feature, the fermion mediated RKKY interaction and their connection with Efimov physics.

Recently, following more experimental observations from our experiment, the internal connections between these two topics became more clear and offer some possible explanations to those puzzles we had during the sound speed project. Moreover, this project dives deep into the non-trivial strong interaction regime of quantum degenerate Bose-Fermi mixtures which, which offers an unique example of investigation in a regime which is of great theoretical interest. In this work, we investigate the Li-Cs quantum mixture in the RKKY-Efimov transition regime by tuning the interspecies interactions across a Feshbach resonance. We show the interplay between fermion mediated interactions and Efimov physics. Specifically, when the the scattering length approaches the Fermi gas length scale $k_F|a_{BF}| \approx 1$. We observed a resonant structure that manifests in both the dynamical response of collective excitations as well as the decay and heating of the Cs condensate. The resonance position is in qualitative agreement with the theoretical model that incorporates both RKKY and Efimov physics. This observation indicates the rich and unique charm of Bose-Fermi mixture systems and possibly offers a hint for further study of nuclear physics and condensed matter using quantum simulation systems. This chapter will first introduce common and useful theories in a Bose-Fermi mixture, following by a presentation of the experiment.

5.1 Theory of Bose-Fermi Mixtures

5.1.1 Boson Pairing Induced by Fermion Mediated Interaction

In this section, we briefly summarize a portion of the discussion of Refs. [42] [17] [114]. These reference introduce the key theory of fermion mediated interaction between bosons and the resulting boson-boson pairing resonance.

Generally speaking, including important terms and doing the correct calculation is non-

trivial, but the mass imbalance between bosons and fermions ease the theoretical difficulty greatly without losing the rich physics. The large mass ration between Cs and Li sets a clear separation of the time scale of dynamics. Such time scale separation validates the Born-Oppenheimer approximation. The idea behind Born-Oppenheimer approximation is, when the perturbative term (in this context, the light fermions scatter onto heavy bosonic Cs atoms) is not affecting the zeroth order Hamiltonian, the wave function of the original object (Cs atoms) could be approximated by its unperturbed wave function. For an examples, when a high energy particle scatters onto a weak potential, its wave function is marginally perturbed. One can use its unperturbed wave function to compute its effect on the potential and deflection on its trajectory. In our case, the Cs atoms are much heavier than Li atoms, we can treat their motion to be much slower than the Li atoms. This means that, the fermionic degree of freedom could be considered while treating the Cs atoms as static. Eventually, one can integrated out the fermionic degree of freedom so that treating the complicated Bose-Fermi interaction as an effective potential between bosons is possible.

Consider two neighboring Cs atoms immersed in Li atoms with separation R. Under Born-Oppenheimer approximation, the two Cs could be viewed as two delta function forming a double well potential inside the Fermi gas. Such double well potential has a few body and a many body effect on the Fermi gas. The few body aspect comes from the fact that a double well potential is more likely to capture a fermion compared with a single delta function trap of one boson. Here we treat the Cs atoms as two static impurities which we model as two zero-range pseudopotentials, which is a solid assumption as the Van der Waals potential are usually as large as few Bohrs. A more general version of such derivation is presented in Ref. [114]. Near the two impurities, the fermion wave function is subject to the restriction given by Bethe-Peierls boundary condition (a fancy word for the familiar format: $(R\psi(R))'/R\psi(R) = -1/a_{BF}$, which gives $\psi(R)_{R\to 0} \to 1/R - 1/a_{BF}$, the pseudopotential approximation format).

$$\psi(x \to R_i) \propto \frac{1}{|x - R_i|} - \frac{1}{a_{BF}} + \mathcal{O}(|x - R_i|). \tag{5.1}$$

Here a_{BF} denotes the Bose-Fermi scattering length. Such double well potential supports two possible bound states with energy $E_\pm = -\hbar^2\kappa_\pm^2/2m_F < 0$, where $\kappa_\pm$ is the solution to equation 5.2:

$$\kappa = \frac{1}{a_{BF}} + \frac{1}{R}W(e^{-R/a_{BF}}), \tag{5.2}$$

here $W(x)$ is the Lambert W function solves $x = W(x)e^{W(x)}$. The two solutions $\kappa_\pm$ shows up under different conditions. κ_-, it only shows up when $R > a_{BF} > 0$ whereas the κ_+ shows up under for as long as $a_{BF} > 0$ or $a_{BF} < 0$ but $|a_{BF}| > R$. On the positive scattering length side, the two solutions could be understood as the symmetric and anti-symmetric solution under the double well potential. The anti-symmetric solution κ_- is apparently more fragile since it requires the two delta function wells to be far enough such that the trapping potential can overcome the kinetic energy term of the Hamiltonian. On the other hand, the symmetric solution κ_+ is puts loose restrictions on the potential well. For attractive interaction, it requires the two attractive impurities to be close enough so that a bound state is supported. See Fig. (5.1). It should be pointed out though, in actual experiment, phase separation of BEC and degenerate Fermi gas(DFG) and the molecule branch make it complicated so the two bound states story might not be what's really happening in actual experiment, as for example, on positive scattering side the Efimov state is suppressed by molecular branch. One observation is, the negative branch solution requires two bosons and one fermion. In fact, it is directly related to the Efimov state when the mixture is at low density limit.

On the other hand, there is a many body aspect of the problem as well. For a fermion in the continuum with energy $E = \hbar^2k^2/2m_F$, it accumulates an additional phase shift when

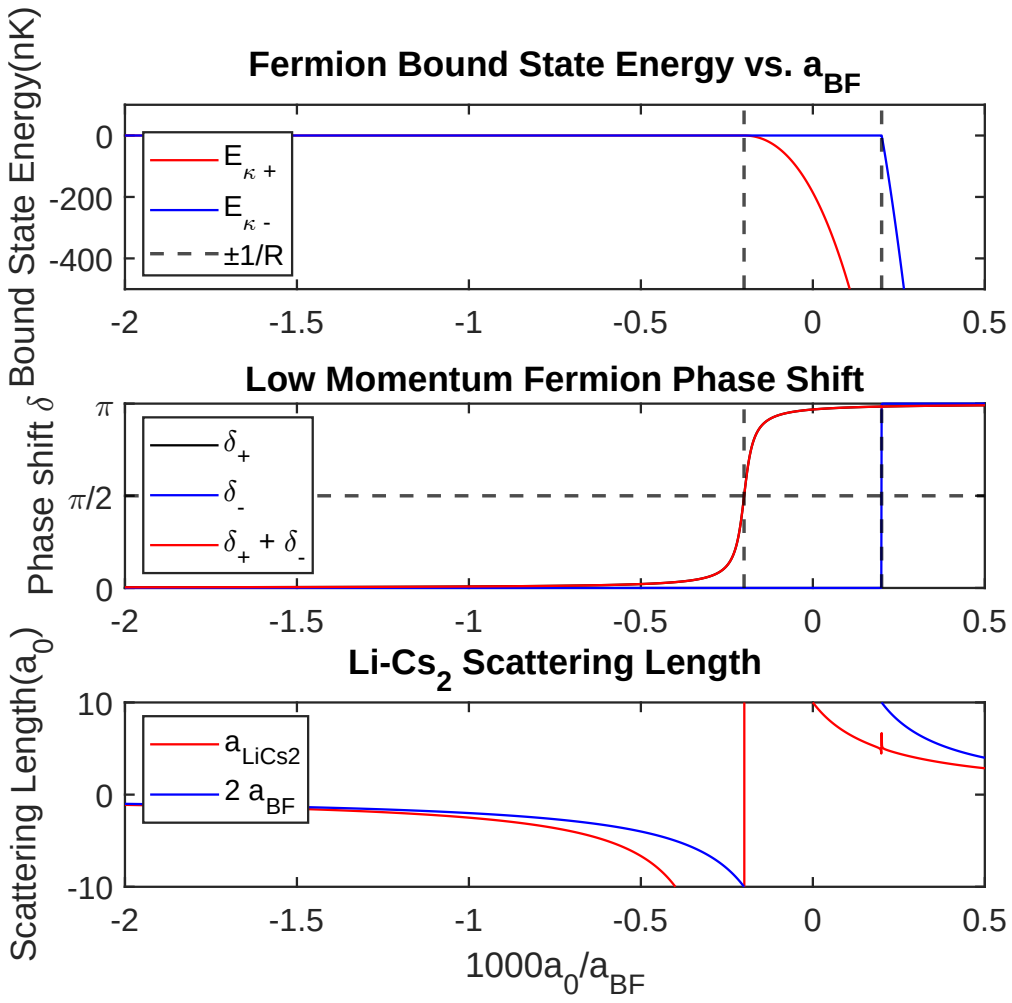

Figure 5.1: Bound State of fermion trapped by the double well potential. The κ_- solution clearly has a much steeper slope in its energy spectrum meaning that it will cause a much narrower resonance with the continuum. The narrow feature is also indicated by the phase shift and scattering length.

scattered onto this double well potential. For each mode $\mathbf{k}$, the accumulated phase shift is:

$$\tan\delta_{\pm}(k) = -\frac{kR \pm \sin(kR)}{R/a_{BF} \pm \cos(kR)}, \tag{5.3}$$

where the $\pm$ sign comes from two different impurities, and $0 \leqslant \delta_{\pm}(k) < \pi$. Taking the limit of $R \to \infty$ of Eq.(5.3) is interesting: $\tan\delta_{\pm}(k) = -ka_{BF}$. This is simply the phase shift a fermion in continuum will acquire being scattered by two independent bosons. In other words, the non-trivial phase shift a fermion acquires is closely related to the fact that the bosonic separation R is comparable with the length scale to fermion wavelength $1/k$. In the presence of a well defined Fermi surface, the only length scale related to many body phenomena is Fermi wavelength $1/k_F$. In our system, the bosonic separation is $R \approx 5000a_0$ whereas the Fermi wavelength of a non-interacting degenerate Fermi gas is $1/k_F \approx 6000a_0$. The Fermi gas has a comparable characteristic length scale with the BEC while its density is a factor of $\sim$100 lower. The additional phase shifts of the entire Fermi gases have a macroscopic effect: it leads to an effective interaction between bosons. In the weak coupling limit, it reproduces the familiar RKKY potential form the previous chapter. It's also worth mentioning that, in the weak interaction regime, the effective interaction between bosons is always attractive, regardless of the sign of the inter species scattering length a_{BF}. A possible explanation is: it depends on the quantum statistic of the impurities, see Ref. [119].

Summing up the few body and the many body contribution, the total energy shift of the entire system is:

$$\Delta E(R) = -\frac{\hbar^2\kappa_+^2 + \hbar^2\kappa_-^2}{2m_F} - \int_0^{k_F} \hbar^2 k \frac{\delta_+(k) + \delta_-(k)}{\pi m_F} dk. \tag{5.4}$$

However, this is the total energy shift due to two impurities: if one places two impurities really far apart, Eq.(5.4) still has non-zero value, in which case it represents the (first order) mean field energy shift due to fermion-impurity interactions (i.e. polaron energy). Therefore,

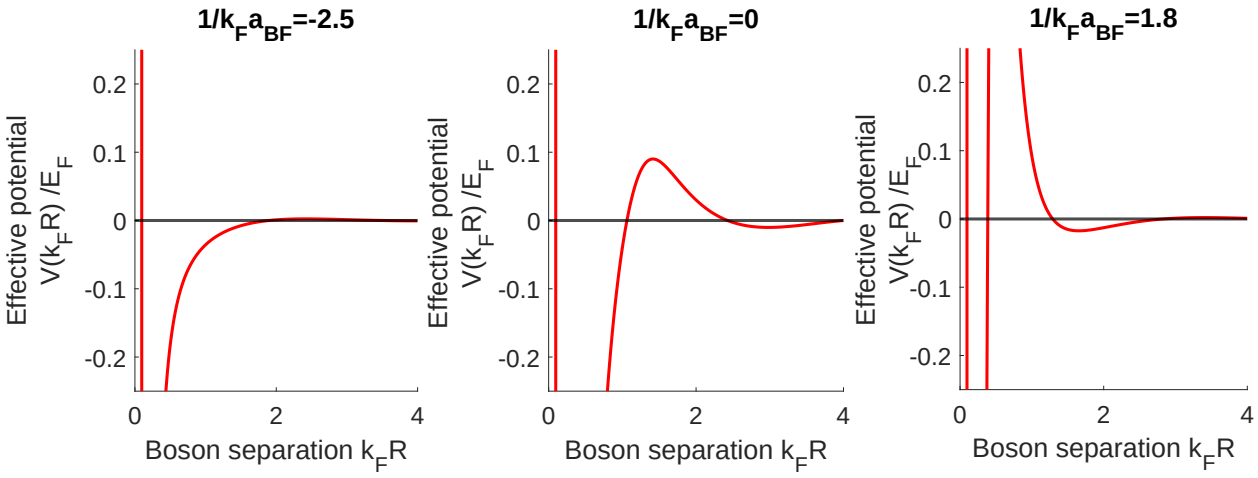

Figure 5.2: Effective potential from mediated interaction. Mediated interaction starting from weakly attractive, resonantly interacting and repulsive interaction. The potential is plotted in dimensionless form. The y-axis and x-axis are in unit of Fermi energy and Fermi momentum, respectively.

we need to deduct the mean field contribution to get the impurtity-impurity binding energy. We define polaron energy as:

$$\Delta E(R \to \infty) \to \mu \tag{5.5}$$

with

$$\mu = -\varepsilon_F \frac{k_F a_{BF} + [1 + (k_F a_{BF})^2][\pi/2 + \arctan(1/k_F a_{BF})]}{\pi (k_F a_{BF})^2} \tag{5.6}$$

here the polaron energy μ is expressed in unit of Fermi energy ε_F. The resulting induced potential $V(R)$ is given by Eq.(5.7). Fig. (5.2) is a the computed potential form agreeing with that from Ref. [42].

$$V(R) = \Delta E(R) - 2\mu \tag{5.7}$$

Given the effective induced potential $V(R)$, Cs-Cs scattering property could be calculated via the Schrödinger equation:

$$[\ -\frac{\bigtriangledown_{\mathbf{R}}^2}{m_B} + V(\mathbf{R}) + 2\mu - E]\ \Psi(\mathbf{R}) = 0 \tag{5.8}$$

To solve the 3D Schrödinger equation, one needs to transfer into center of mass coordinate and rewrite it into a spherical coordinates, as the case for solving the electron wave function in hydrogen atom. The resulting equation is a second order linear equation. Numerically solving such equation could be done via an ODE solver or by discrete variable representations [106]. Fig. (5.3) shows the first few eigenfunction of the Hamiltonian. Therefore, we can further plot the energy of the lowest state at different interaction strengths, see Fig. (5.4). It should be pointed out, that to match the theory with experimental observation at low density, the energy zero crossing should matches the Efimov resonance position. This matching is achieved via tuning the hard shell cutoff a_c. Such tuning is necessary since the few body contribution to potential $V(R)$ will otherwise behave like $-\alpha^2/R^2$ with $\alpha > 1/4$. Such divergence not only causing divergence problem in Born-Oppenheimer approximation but causes an state with energy not bounded from below. For example, for the combination of Li-Cs, it predicts Efimov resonances at $a_{BF} = -3300a_0/c, -3300a_0/c^2, -3300a_0/c^3...$, with $c \approx 5$. Since Efimov states are basically a series of three body bound state with their sizes scaling by c, it should be realized that these trimers can not be infinitesimal: eventually the natural cutoff length scale at range of physical Van der Waals potential should play a role. In fact, cutoff a_c has the physical meaning that the three particles of the trimer can not show up in the same position, and it is also closely connected with three parameter in field theory or study of Efimov physics [160] [161] [23] (PS: these papers are strikingly good on explaining how the pair-wise two body interaction gives rise to the non-trivial universality in three body parameters).

To better compare with experimental observation, it is a good idea to calculate the induced scattering length a_{ind}. For this purpose, it is more convenient to focus the computation on the induced phase shift, instead of the entire wave function. This could be achieved by

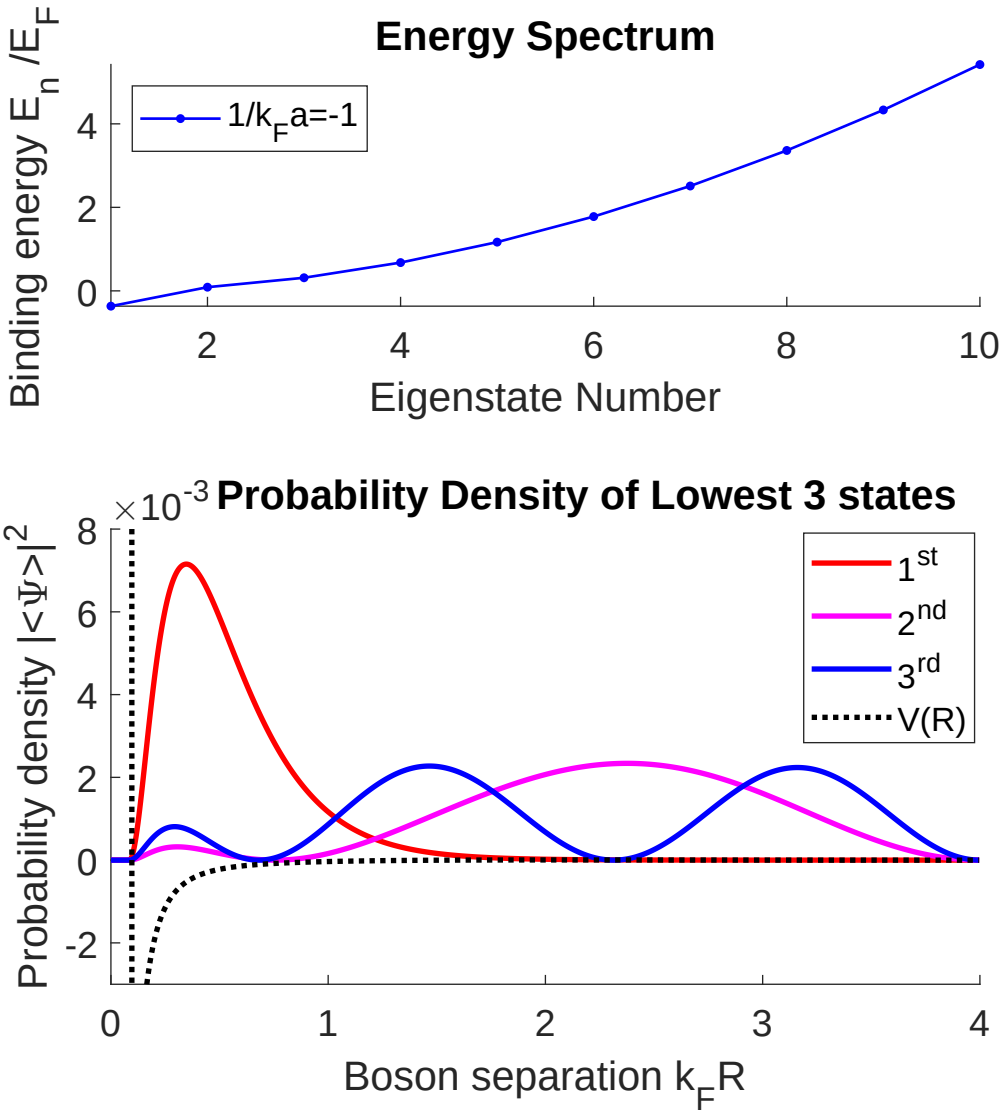

Figure 5.3: Energy spectrum and wave function of Cs atom pair. The energy spectrum in the top figure indicated that there is a Cs-Cs bound state with the rest being in continuum. The bottom figure's solid red, magenta, blue lines are the first, second and third eigenstates, respectively. Eigenstates with higher principle number N are closer to a free particle dispersion curve. The bound state is localized inside the effective potential $V(R)$ with its size being $\sim 1/2k_F$. The black dotted line is the potential $V(R)$ plotted in arbitrary units. The underlying logic of discrete variable method is diagonalizing matrix a matrix with its dimension same as the size of discrete space. It features a clear distinction between different eigenvalues as compared with ODE solver.

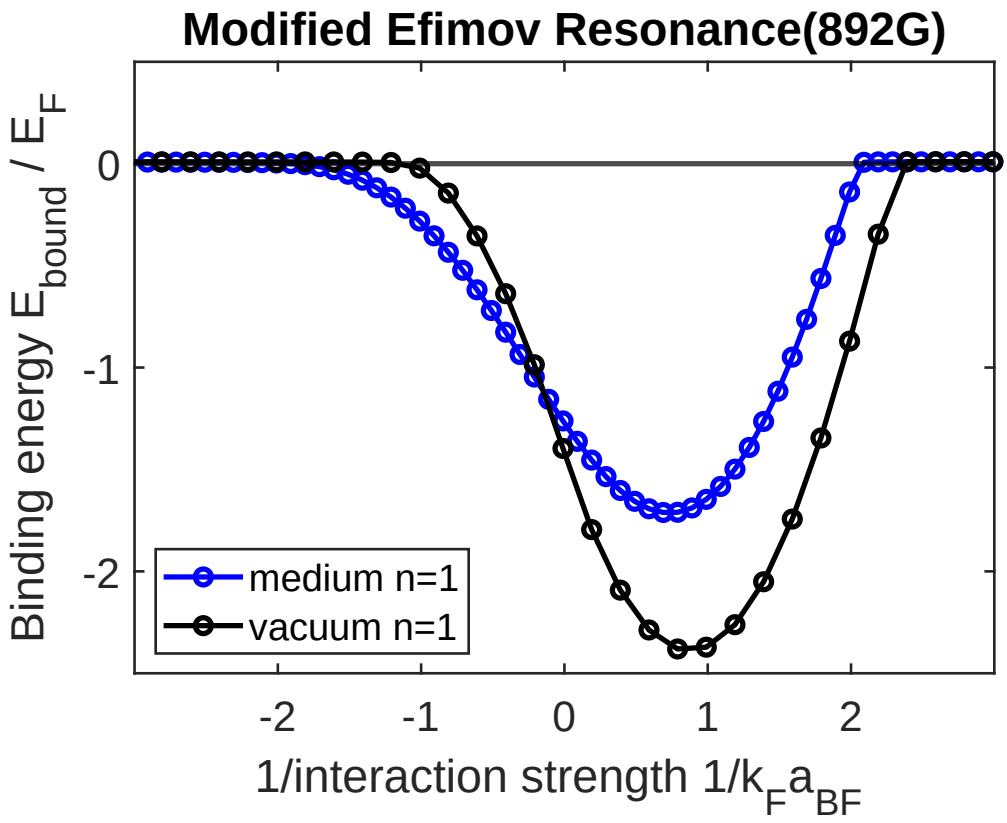

Figure 5.4: Energy spectrum of Efimov resonance. Energy of the lowest state of a function of interaction strength $a_{BF}k_F$. The fermion density set at constant value of $n_{\mathrm{Li}} = 4.7\times10^{17}/\mathrm{m}^3$ for the in medium case (blue solid line). For zero fermion density limit (black solid line 'vacuum'), the position of zero crossing of the energy spectrum is tuned so that it matches with the observed Efimov resonance position at $a_{BF} = -3300a_0$ (see text). Comparing the energy spectra, the effect of degenerate Fermi gas is very obvious. It shifts the Efimov resonance position to weaker attraction regime while shifting the other resonance towards stronger repulsive side.

variable phase method, under which we rewrite the second order differential equation into a first order non-linear differential equation, following Ref. [157] [8] [44]. The idea behind this is, we know that far away from the scattering potential, the wave function is in a form of spherical harmonic as described in chapter 2. This method transform that general solution into a simple non-linear term as:[42] [114]

$$k\partial_R \delta^{ind}(k,R) = -m_B V(R)\sin^2(kR + \delta^{ind}(k,R)) \tag{5.9}$$

Where $\delta^{ind}(k,R)$ is the phase shift with incoming momentum k and separation R. This differential equation has the boundary condition $\delta^{ind} = -ka_c$ at $R = a_c$ (compared with vacuum, the phase is delayed by this hard shell), where the short range cut off $a_c = 340a_0$ in following calculation. In numerical computation, I used an ODE solver to compute the phase shifts δ_{ind} for a number of small momentum values, so that the linear relation holds as Eq.(5.10). Fig. (5.5) shows an example of the simulation of phase shift.

$$\tan\delta_{\text{ind}} \approx \delta_{\text{ind}} = -ka_{\text{ind}} \tag{5.10}$$

To predict the resonance position in our system, there is one extra consideration that needs to be taken into account: given the time scale in the experiment is slow compared with Li. Due to mean field attraction, fermion will pour into where the BEC and thus increases the local fermion density, so as for the local Fermi wave vector k_F. Therefore, we need to consider this mean field effect before the full computation:

$$k_F = (k_{F0}^2 - 4\pi\frac{m_F + m_B}{m_B} n_B a_{BF})^{1/2} \tag{5.11}$$

Where k_{F0} denotes the Fermi wave vector for a non interacting Bose Fermi mixture. Fig. (5.6) shows how the local Fermi vector is enhanced as stronger attraction is tuned. We also compare it with one of our early data set where we quench the magnetic field and observe the

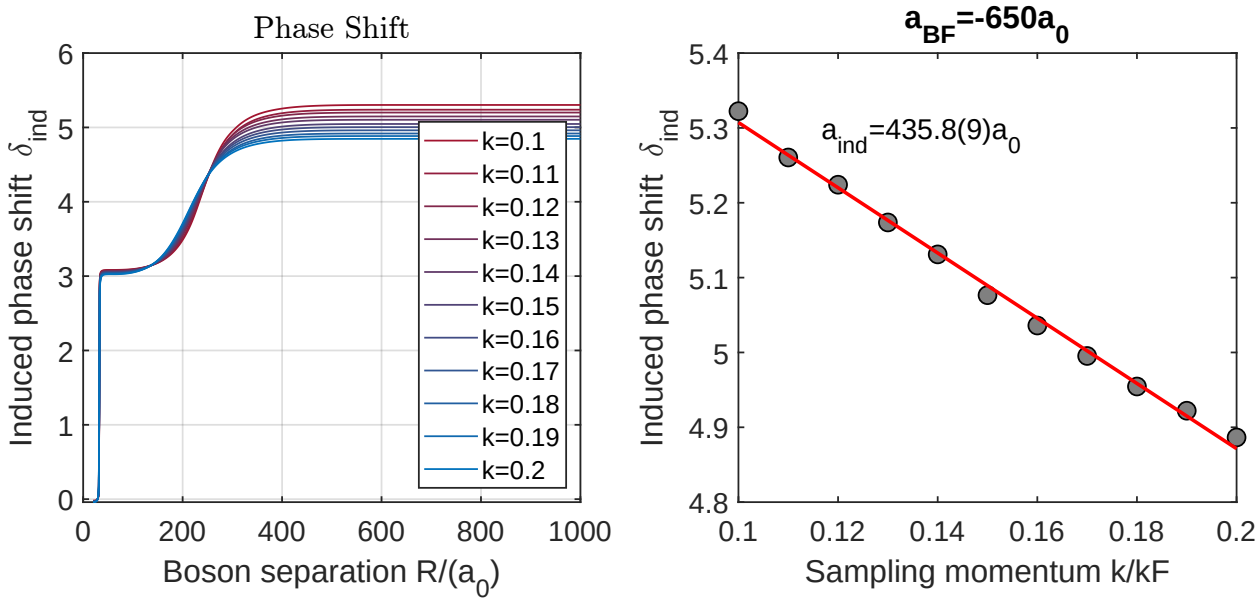

Figure 5.5: Example of phase shift computation. With a number of small k value input, the resulting phase shift is computed as it travels further away from potential center. Right figure is a linear fit to deduce the value for scattering length. The presence of error bars could help indicating possible numerical error.

density evolution of Fermi gas. From fitting with double Gaussian function we estimate how much the fermion density is enhanced at 0.5ms after fast field quench, see Fig. (5.7).

Finally, we reach at the prediction for resonance position, see Fig. (5.9). It should be noted that, though the introduction of the hard shell potential barrier is necessary to regularize the few body potential, it has screening effect on the many-body RKKY potential which shifts the true resonance towards strong interaction. In fact, our theory predicts no bound state near $a_{BF} \approx -1000a_0$, therefore a Cs-Cs two-body resonance at $a_{BF} = -1300a_0$ might be more valid. A purely many body RKKY model without the few body potential will instead predict a resonance at $a_{BF} = -1300a_0$, closer to experimental observation. This two-body resonance prediction is also consistent with the observation that the Li atom loss feature does not have the same peak as that of Cs. The ultimate solution to such theoretical subtlety is too find a better short range cutoff ansatz such that it reproduces the Efimov resonance and does not have screening effect on the many body RKKY potential. During

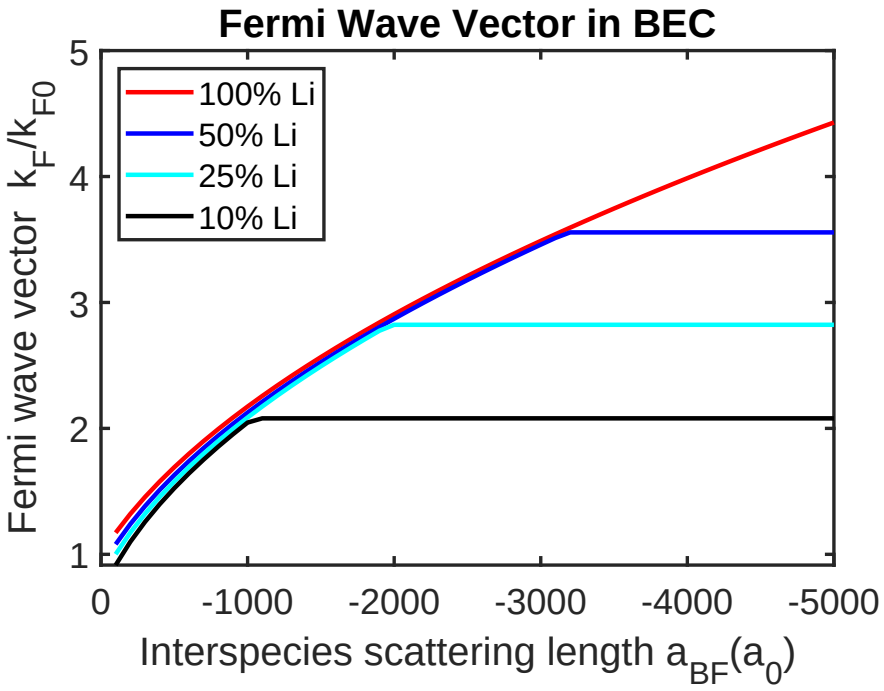

Figure 5.6: Local Fermi wave vector k_F vs. inter species scattering length a_{BF}. Due to mean field attraction, a_{BF} has a much stronger effect than fermion number in the mixture. Unless sample of really low fermions number is prepared, k_F values are enhanced by similar amount. Especially for our experiment observed resonance around $a_{BF} = -1100a_0$, initial fermion number has a very weak effect on local k_F which offer an explanation why the observed resonance shows up at roughly same interaction strength. Besides, since we have finite Li atoms in our sample with maximum number of around 20k (100%), eventually fermion density will stop increasing due to depletion of background fermions. Such effect is considered here with varying fermion number fraction in the sample, labeled by 100%, 50%, 25% and 10%.

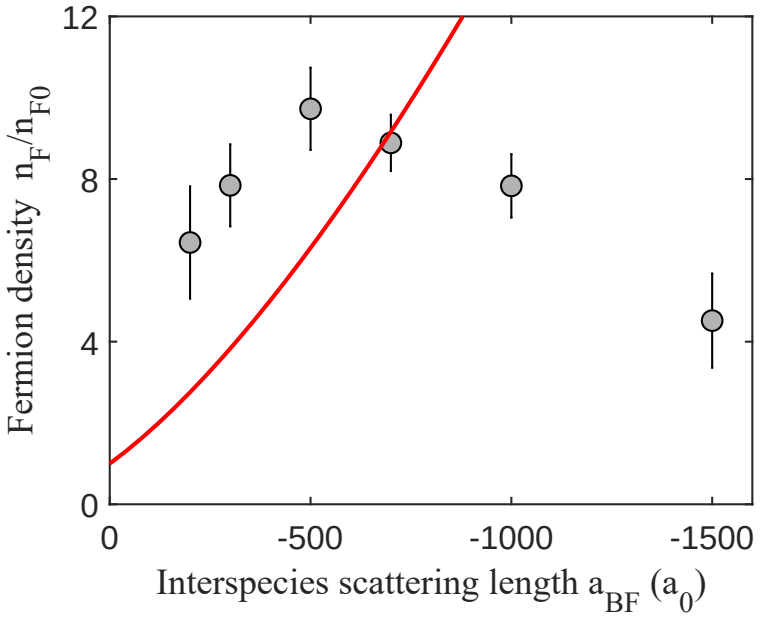

Figure 5.7: Estimation of fermion density enhancement inside BEC. We prepare weakly interacting Bose-Fermi mixtures and quench to target interaction strength. Dual species *in situ* imaging is taken 0.5ms after the quench. We found the fermion density inside BEC is enhanced by almost a factor of ten, in qualitative agreement with the mean field model prediction.

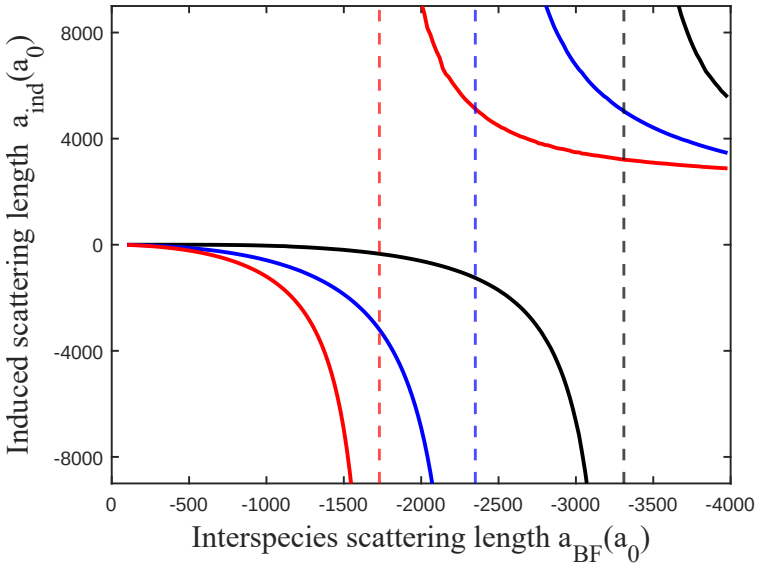

Figure 5.8: Tilmann Enss Model [42] prediction with Increasing Fermion Density. The effective scattering length induced by mediated interactions a_{eff} with fermion density $n_{\text{F}} = 0, 0.1, 1, 10\ n_{\text{F0}}$(black, blue, magenta, red solid lines), where $n_{\text{F0}} = 4.7 \times 10^{17}/\text{m}^3$ is the background fermion density of non-interacting Bose-Fermi mixtures. The algorithm's numerical stability is improved so they looks a bit more smoother.

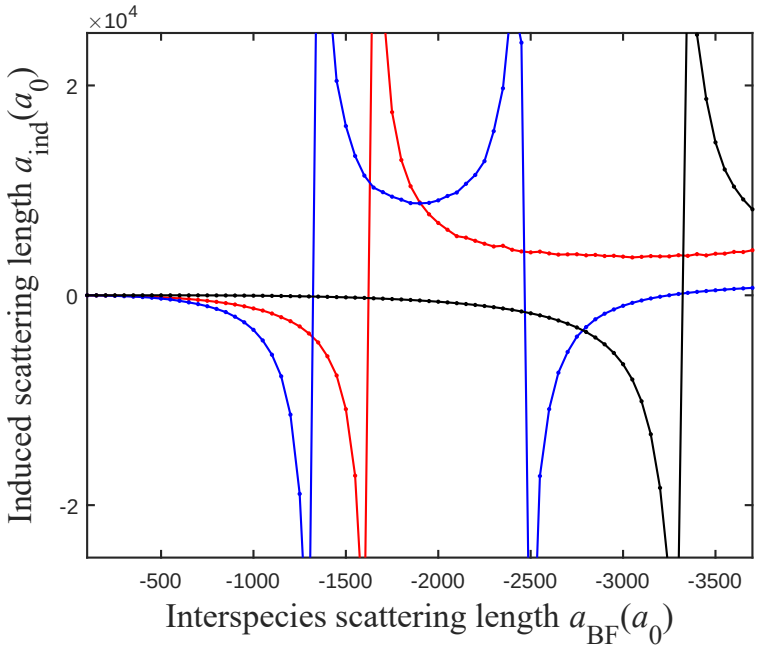

Figure 5.9: Predicted resonance position with different models. A full model containing both many-body and few-body potential (red) predicts a resonances at $a_{BF} = -1600a_0$. When only considering the many body RKKY interaction (blue), the theory predicts a resonace at $a_{BF} = -1300a_0$. In the few body limit (black), the theory reproduce the Efimov resonance.

the project, I have been trying various formats yet no really good answer is found. The best but still problematic solution is replacing the few body Efimov potential with $V_{\mathrm{Efi}}(R) = 0$ under certain cutoff, shown in Fig. (5.10). I have to leave this question to people who are interested.

It's worth a mention that, the potential model from Eq.(5.4) could still be approximated by the perturbative format of RKKY interaction potential near around $a_{BF} \approx -1000a_0$, see Fig. (5.11). The equation for induced effective scattering length between Cs atoms can be written in a concise dimensionless form:

$$k_F \frac{da_{\mathrm{ind}}(R)}{dR} = (a_{\mathrm{BF}}k_F)^2 \frac{2Rk_F\cos(2Rk_F) - \sin(2k_FR)}{(k_FR)^4}(k_FR - k_Fa_{\mathrm{ind}}(R))^2 \qquad (5.12)$$

Eq.(5.12) predicts the resonance position at $a_{\mathrm{BF}} = -0.51/k_F$, which predicts a resonance

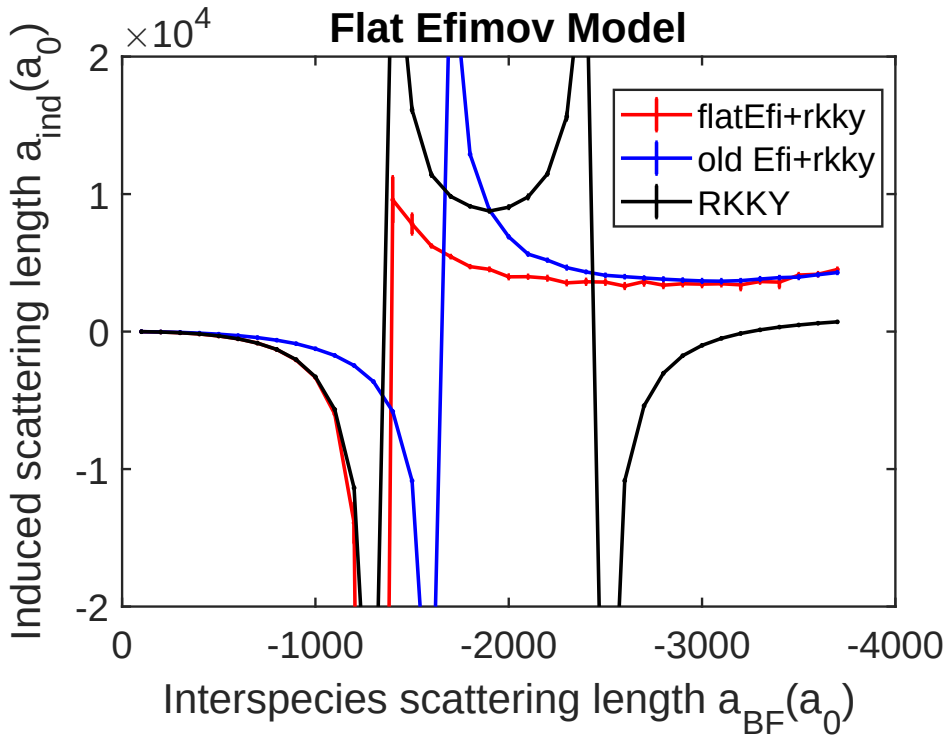

Figure 5.10: Comparing cutoff models. The red solid line of 'flatEfi' is the one replacing the hard shell cutoff with a vanishing few body potential inside certian range. This improves the issue of screening effect therefore it predicts a resonance position which is similar to the one from a purely many body effect potential (black solid 'RKKY'). Yet this still comes with price, the abrupt change in potential causes numerical instability as well as declined performance near where resonance happens. On the other hand, the 'RKKY' theory has its own problem: it seems that the bound state vanishes as $k_F a_{BF}$ becomes larger which might indicates that the short range few-body Efimov interaction is critical near resonance.

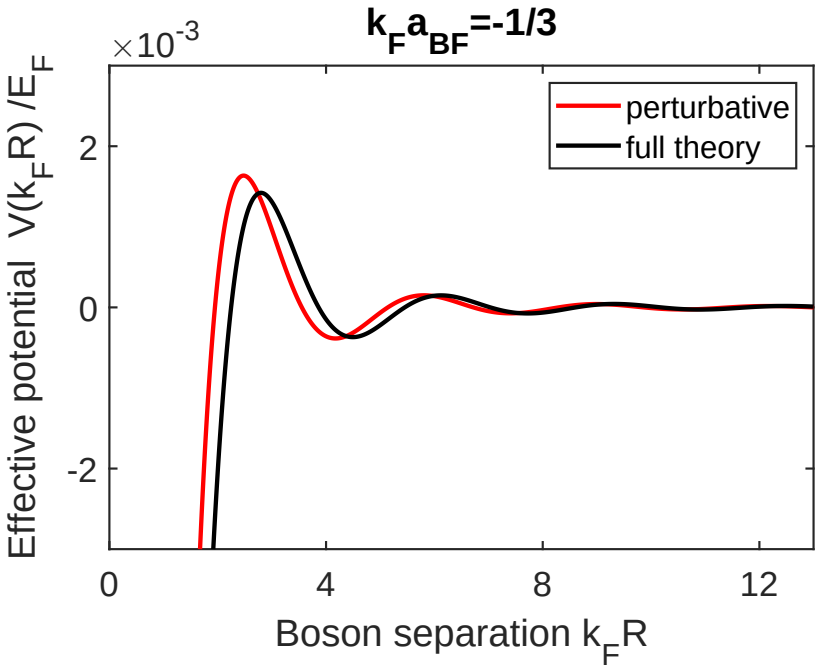

Figure 5.11: The full model could be approximated by the perturbative RKKY model without a qualitative loss in prediction power, but it leads to a nice dimensionless format

position near $a_{BF} = -1300a_0$ as well.

5.2 Phase Imprinting Measurement

Dispersion spectrum is one of the upmost important properties in condensed matter and cold atom research and it is directly comparable with theoretical predictions [57]. In previous work we measured the sound speed which is the long wavelength and static limit of the dispersion spectrum. On the other hand, Bragg spectroscopy type measurement, either by optical lattice or DMD is a very common method for measuring the dispersion relation [138] [145]. As it is described in Chapter 3, our DMD and high resolution *in-situ* dual species imaging makes it appealing to measure the dispersion properties of Bose-Fermi mixture. Below I will first describe the experimental procedure and then show our observation.

We first prepare a degenerate sample Bose-Fermi mixture with mildly attractive interaction. Our experiments begin with a pure BEC of 30,000 ^{133}Cs atoms immersed in a single

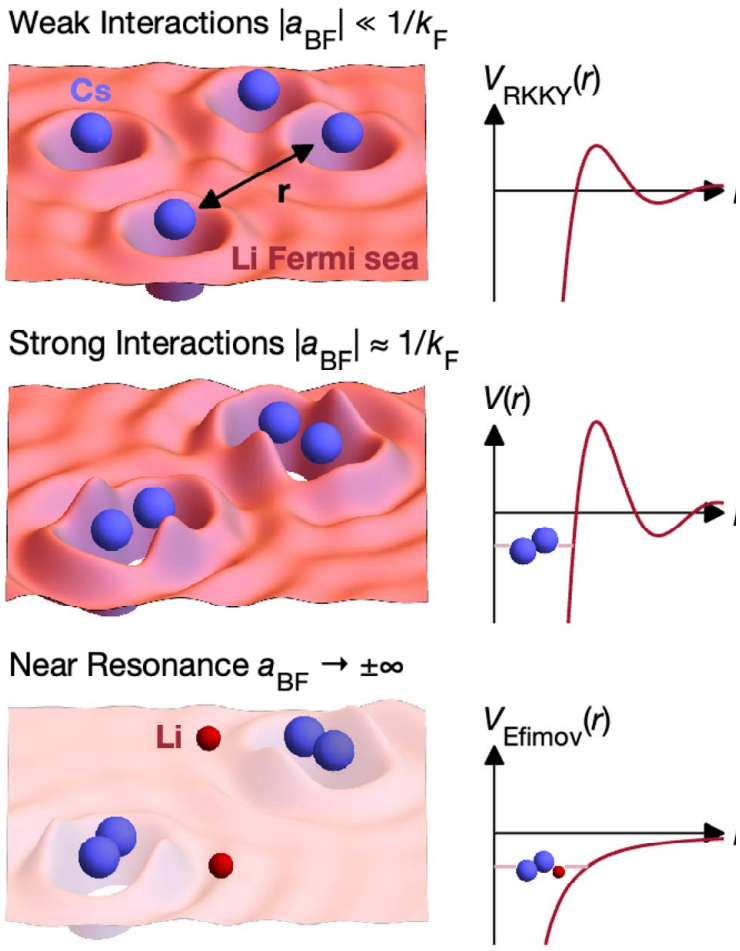

Figure 5.12: Quantum mixtures of heavy bosonic ^{133}Cs atoms and light fermionic ^{6}Li atoms in different regimes. In the weak coupling regime $|k_F a_{BF}| \ll 1$ (top panel), fermionic scattering leads to correlations between Cs atoms through the Ruderman–Kittel–Kasuya–Yosida (RKKY) mechanism. The RKKY potential $V_{RKKY}(r)$ is long-ranged and oscillatory due to the Friedel oscillations of the Fermi surface (ripples depicted in the Fermi sea). In the strong coupling regime $|k_F a_{BF}| \sim 1$ (middle panel), we report in this work pairing of Cs atoms due to enhanced mediated interactions $V(r)$ with the fermions. The length scale of the mediated potential is $1/k_F \sim 1\mu m$ in our system. As the boson-fermion interaction nears resonance $a_{BF} \to \pm\infty$ (bottom panel), boson-boson-fermion bound states known as Efimov states emerge. Because of the large mass ratio, Born-Oppenheimer approximation gives effective potentials $V(r)$ in different regimes as a function of the separation r between Cs atoms

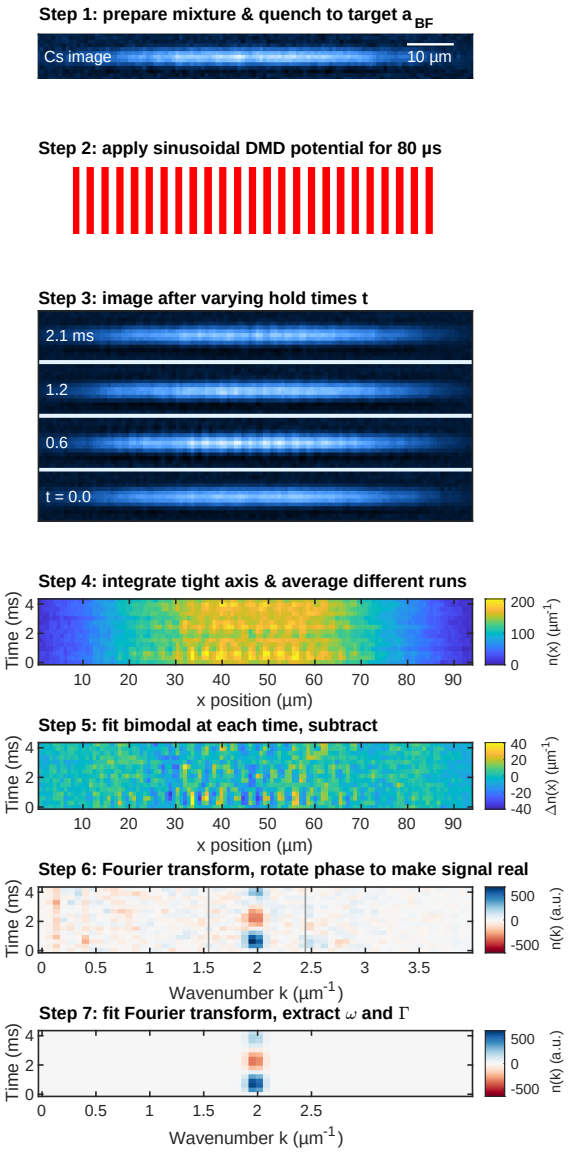

Figure 5.13: Our analysis procedure for phase imprinting experiments. In Step 1, we prepare a degenerate ^{133}Cs-^{6}Li Bose-Fermi mixture at weak attractive interactions ($a_{\mathrm{BF}} = 300a_0$, before quenching in 0.8ms to a target interactions strength. We then apply an $80\mu s$ repulsive DMD potential with spatial frequency k to the sample. In Step 3, we then image after varying hold times. In Step 4, we integrate along the radial direction and average the three rounds of data together to get the 1D axial density $n(x)$. In Step 5, we fit a bimodal at each time and subtract off the fit to get a background-free view of the density waves, $\Delta n(x)$. In Step 6, we Fourier transform $\Delta n(x)$, then rotate the phase of the resulting Fourier transform to make the density wave signal real. The vertical gray lines in Step 6 show the extent of the fit region that we use in Step 7, where we perform a fit as described in Eq. 5.13 to extract the frequency ω and damping Γ of the density wave oscillations.

component degenerate Fermi gas of up to 20,000 ^{6}Li atoms. The mixture is prepared in a single beam dipole trap with a weak axial and tight transverse confinement. The trap frequencies are $\omega_{\mathrm{Cs}} = 2\pi \times (6.53, 114, 153)$ Hz for Cs and $\omega_{\mathrm{Li}} = 2\pi \times (36, 330, 330)$ Hz for Li. Both species are spin-polarized in their lowest hyperfine ground state, where the inter-species scattering length a_{BF} can be tuned near a Feshbach resonance at 892.65G. Over this range, a bare Cs BEC is stable with a near constant boson-boson scattering length $a_{\mathrm{BB}} = 270\ a_0$ [16], where a_0 is the Bohr radius. A bare fermi gas is also stable and non-interacting. After preparing a degenerate mixture, we ramp the magnetic field from $a_{\mathrm{BF}} = -150\ a_0$ to $-300\ a_0$ in 10ms and then allows 5ms for the magnetic field to settle. The mixture is initially prepared with weak attractive interactions at a temperature 30 nK. The BEC chemical potential is $\mu_{\mathrm{B}} = k_{\mathrm{B}} \times 35\,\mathrm{nK}$, where k_{B} is the Boltzmann constant, and the Fermi energy up to $E_{\mathrm{F}} = k_{\mathrm{B}} \times \mathrm{t} = 370\,\mathrm{nK}$. To probe the mixture in the transition regime, we apply a carefully engineered field jump sequence which achieves the target magnetic field within 0.8ms, after which the field is stable within 10ms. This field fast switching technique is described in chapter 2.

We define the beginning of the field jump $t = -1\,\mathrm{ms}$. We apply an 80 µs repulsive DMD pulse at $t = -0.08\,\mathrm{ms}$, 0.92 ms after initiating the field jump. The DMD pattern we apply is a simple N pixel on N pixel off vertical stripe pattern as shown in 5.13, although for longer wavelength patterns, we use a pattern that approximates a sinusoidal intensity using the error diffusion halftoning algorithm, as the simple binary pattern produces noticeable higher spatial harmonics at long wavelengths. By varying the DMD pulse length, we verified that the measured density wave amplitude is linear in the DMD pulse length, showing that we are not exciting too large a fraction of the condensate into the $\pm k$ modes.

After applying the DMD pulse, we wait a varying hold time t before taking a Cs-first dual-species *in situ* image instead of imaging Li then Cs as our common practice (The reason being: since there is still near 0.5ms in between the two imaging pulses, imaging the Li will

hurt the fine detail signals of the Cs pattern). We perform three rounds of the experiment at each scattering length and each value of t for averaging.

To analyze the quasiparticle dispersion, we proceed by integrating along the tight axis of each image to produce a 1D density profile (Fig. (5.13) continued). We then fit and subtract off a bimodal background distribution separately at each time t to produce a background-free view of the density wave evolution. Next, we Fourier transform the data at each time step, and rotate the phase of the resulting Fourier spectrum $n(k,t)$ so that the datum with the largest amplitude is real and positive (typically, this datum is expected to be at $k = k_{\text{applied}}$ and t slightly greater than 0). Finally, we perform a 2D fit to the real part of this resulting Fourier transform. The fit function we use is Gaussian in k and an underdamped oscillator in t,

$$n_{\text{fit}}(k,t) = Ae^{-(k-k_0)^2/2\sigma_k^2} e^{-\Gamma t} \sin \omega t, \tag{5.13}$$

where A, k_0, σ_k, Γ, and ω are fit parameters, and we only use the data from a small region around k_{applied} for the fit. This model fits the most of the $k = 2.5/\mu m$ data reasonably well, as the density wave appears underdamped in all but the most rapidly decaying condensates (around $a_{\text{BF}} \sim -1100\ a_0$). The measurement results are presented in 5.14.

As shown in Fig. (5.14), after phase imprinting from the DMD pulse, density evolution starts to appear. The Fourier transformed signal is shown in Fig. (5.14)(b). At certain interaction strength, with various periodic patterns, the dispersion of the BEC inside Fermi gas is measured as 5.14 shows, which validates the phase imprinting measurements. To speed up the measurement, we choose the highest momentum mode we could excite, such that the whole measurement process takes 2.8ms.

In the weak interaction regime $|a_{\text{BF}}| < 500\ a_0$, the density wave oscillation is underdamped. The measured $\omega(k)$ can be described by the Bogoliubov dispersion of the BEC with an effective interactions between cesium atoms a_{eff} [35], see Fig.5.14d. Here the ex-

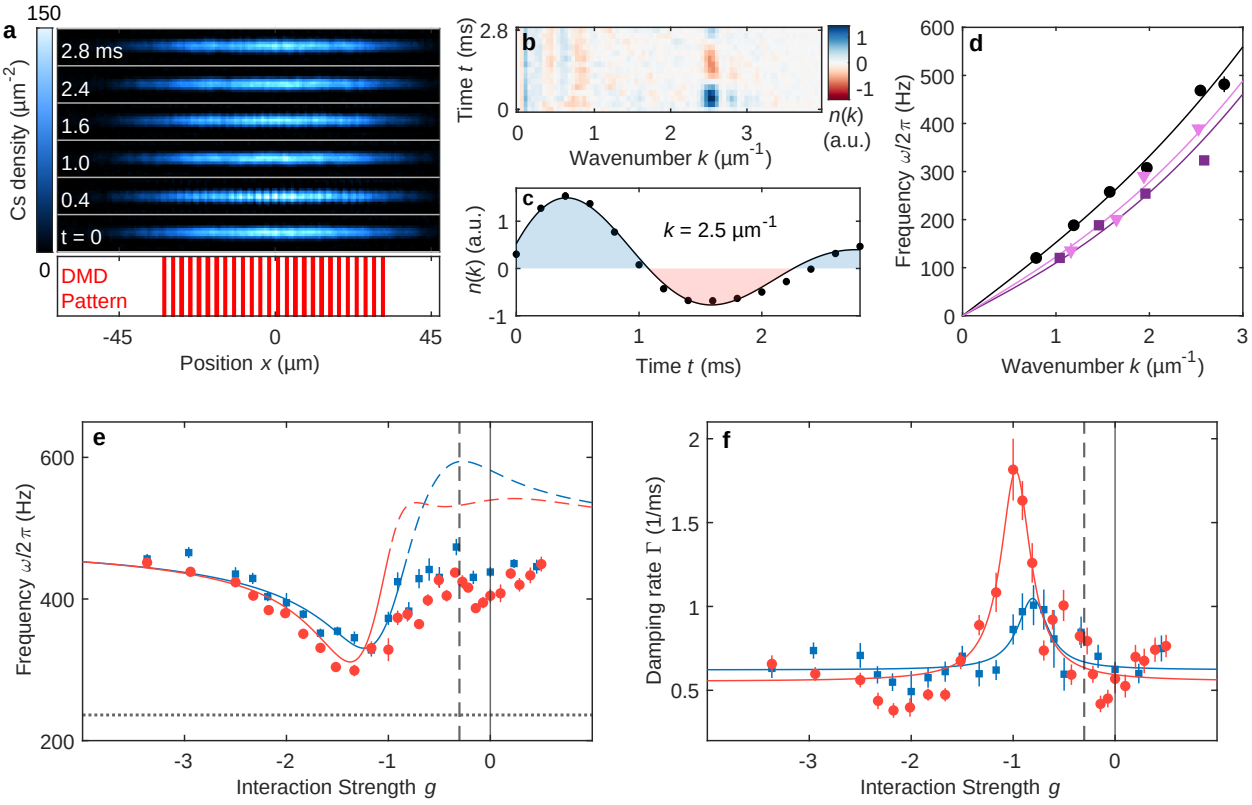

Figure 5.14: Dispersion of Cs BEC embedded in a Li degenerate Fermi gas. (a) We imprint a periodic phase on the Cs condensate with a short 80 μs pulse of a periodic optical potential, generated by a digital micromirror device (lower panel). The phase modulation at wavenumber $k = 2.5\,\mu\text{m}^{-1}$ leads to an oscillating density wave order, shown in *in situ* images of the BECs (upper panel) at an example interspecies scattering length $a_{\text{BF}} = -400\ a_0$. (b) Fourier transform of the density profiles $n(k)$. (c) Real part of $n(k)$ is fit to $n = Ae^{-\Gamma t}\sin\omega t$ (solid line), from which we extract the damping Γ, and frequency ω. (d) Measured frequencies ω for $a_{\text{BF}} = -400\,a_0$ (black circles), $-688\,a_0$ (purple squares), and $a_{\text{BF}} \approx \pm\infty$ (pink triangles). Solid lines are fits to the data based on the Bogoliubov model. (e) Excitation frequency ω and (f) damping Γ at $k = 2.5\,\mu\text{m}^{-1}$ show a resonant dispersive and absorptive behavior for samples with 20,000 (red circles) and 10,000 Li atoms (blue squares). Fits based on an empirical model (solid lines), yield resonance positions at $a_{\text{BF}} = -1030(20)\,a_0$ for 20,000 Li atoms and $-1230(50)\,a_0$ for 10,000 Li atoms. Dashed colored lines in panel (e) indicate the extension of the fit prediction beyond the fitting region, see [**?**] for more data and analysis. In all panels, error bars are 1-σ standard deviations of the mean. In panels (e-f), the black solid line and dashed line indicate the Feshbach resonance and Efimov resonance, respectively. In panel (e), the black dotted line indicates the Cs free particle energy at $k = 2.5\,\mu\text{m}^{-1}$.

tracted a_{eff} is consistent with the RKKY prediction and sound speed measurements [121], see Fig.5.14e. Note here we also observed a decrease of damping rate in $a_{BF} \approx -500a_0$, this is inconsistent with measurement in sound paper[121]. We attribute this to a possible 3D-to-1D transition on our mixture. The BEC experiencing a weaker repulsion as attractive inter-species interaction is tuned, which would reduced the healing length and makes BEC part behaves as an 1D system. Compared with 3D BEC, Bogoliubov phonon has less decay channel thus boosting up its lifetime.

For greater attractions $|a_{\text{BF}}| > 500\ a_0$, damping becomes significant. The extracted frequencies and damping rates can be described by the dispersive and absorptive response of a resonance: the frequency first increases and then returns to the background value after passing a resonance at $-1,060(100)\ a_0$, where the damping peaks. Near and beyond the Feshbach resonance, the measured frequency deviates from our dispersive model, which we attribute to collision loss and the phase separation in the presence of interspecies repulsion [121]. When we reduce the fermion number, the resonance strength weakens.

When interaction is tuned further into resonant regime, we observed reduction on damping rates of the quasi-particle dispersion measurement and the frequency is closer to that of a weakly interacting Bose-Fermi mixture. This agrees with the picture that the resonance feature is shifted towards weaker attractive interaction. This is also consistent with the observation in Ref. [121].

5.3 Excitation and Loss from Mediated Pairing

The observed feature in dispersion behavior indicates a dramatic change of the quasi-particle excitation properties near the resonance. To further understand the nature of the resonance, we investigate closely the loss and heating dynamics of Cs BECs embedded in the Fermi gas. The dipole trap has a strong confinement on the radial axis, leading to a faster dynamics. Immediately after the magnetic field quench, we monitor the condensed and excited fractions

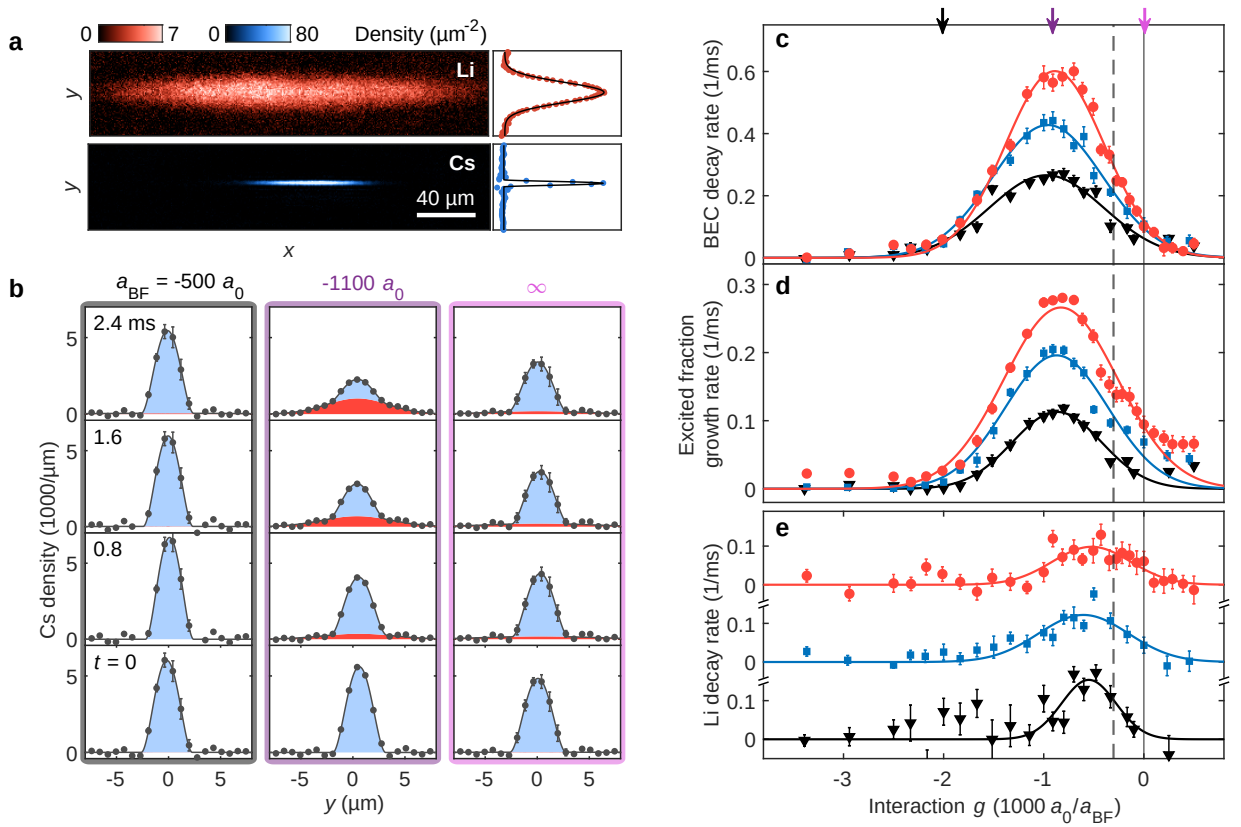

Figure 5.15: Resonant decay and excitation Cs BECs induced by the Li degenerate Fermi gas. (a) Example in situ images of Li and Cs. Right panels show axially integrated density profiles. (b) Evolution of Cs density profile below (left), at (middle) and above (right) the mediated resonance at $a_{\mathrm{BF}} = -1,100\ a_0$. Bimodal fits to the density profile show the condensed (blue) and Gaussian (red) parts of the sample. The Gaussian fraction has an effective temperature of 130 nK to 180 nK. (c) Cs BEC number decay rate, (d) Cs excited fraction growth rate, and (e) Li number decay rate show resonances for samples with 20,000 (red circles), 10,000 (blue squares), and 5,000 (black triangles) Li atoms. Gaussian fits yield average resonance positions at $a_{\mathrm{BF}} = -1090(50)\,a_0$ for the BEC decay, $-1170(30)\,a_0$ for the excitation growth, and $-1800(100)\,a_0$ for the Li decay. In all panels, error bars are 1-σ standard deviations of the mean. In panels (c-e), the Feshbach resonance (vertical solid line) and Efimov resonance (vertical dashed line) are shown for comparison.

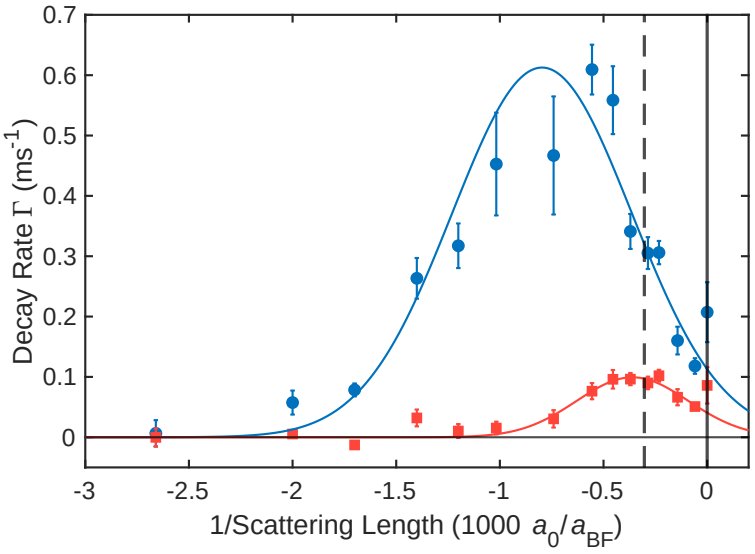

Figure 5.16: Time-of-flight measurement of heating and loss feature. In this experiment, we prepare a weakly interacting Bose-Fermi mixtures at $-300a_{\mathrm{BF}}$ as the procedures for the *in-situ* measurement. After fast magnetic field quench, the mixture is held for varying time $t = 0$ms to $t = 8$ms. A time of flight measurement is taken and Cs atoms are imaged. Yet in the sequence a Li blow-away is not initiated making it a not persuasive enough evidence. The Cs bimodal fitting has been processed with a dedicated algorithm, see Fig. (5.17)

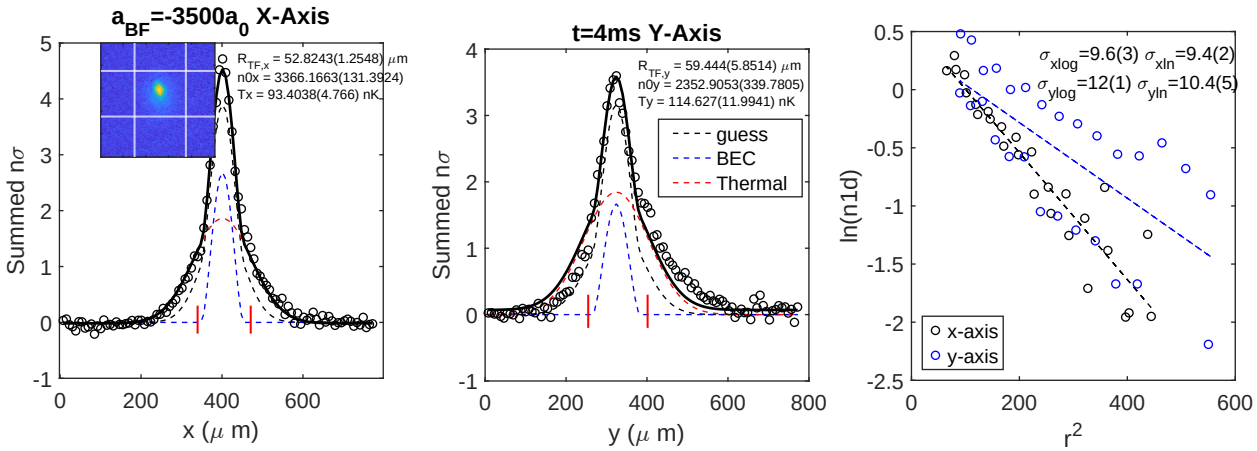

Figure 5.17: Improved bimodal fitting algorithm. A more careful fitting algorithm is applied here, based result from an initial fitting, the Cs cloud's outskirt is then separately fitted in logarithmic scale as the thermal part of Cs cloud has Gaussian tail following Maxwell distribution. The algorithm gives a more reliable fitting in temperature around phase transition. For more details, see Ref. [148].

from the transverse density distribution, see Figs. 5.15a and 5.15b. In the weak coupling regime $|a_{\rm BF}| < 500\ a_0$, the BEC remains pure for the entire measurement windows and demonstrates a lifetime up to more than $\sim 10ms$. Near the mediated resonance, however, BEC decays in a few ms, and the fast decay is accompanied with fast generation of excited atoms, which can be modeled by a Gaussian distribution with an effective temperature $T = 130-180$ nK. Beyond the mediated resonance, both decay and heating rates rapidly decrease. No discernible resonance features are observed at the positions of Efimov and Feshbach resonances. The fitted resonance position at $-1,100(100)\ a_0$ is consistent with the dispersion measurement. These evidences indicate that the instability of the BEC is induced by a fermion-mediated resonance. Though the *in-situ* measurement has the limitation of Cs atoms being in the non-equilibrium states, it reveals quite surprising information combined with observation on the dispersion measurement. Moreover, we measure the Cs BEC decay rate and loss rate with a time-of-flight measurement to search for resonance [105], see Fig. (5.16). This measurement is not perfect as it is an experiment performed in the early phase of the project. Yet it still reveals interesting information. Overall, the Cs BEC decay rate is much slower than the Cs atom loss rate. Besides, it shows that the Cs atom loss and Cs decay rate have different peaks. The fitted center of BEC decay is also around where the resonance feature.

We compare our measured resonance position with the theoretical model. Calculation based on the RRKY potential in the perturbative regime yields a Cs_2 bound state at:

$$a_{\rm th} \approx -2.40\sqrt{\frac{m_F}{m_B}}k_F^{*-1} = -1,440\ a_0, \tag{5.14}$$

which is in fair agreement with our measurement of of $a_{ex} = -1,100(100)\ a_0$. Here the wavenumber of the fermi gas $k_F^* = \eta k_F$ is greater than that of an ideal Fermi gas k_F because of the interspecies attraction. We estimate the enhancement factor $\eta = (1 - g_{BF}n_B/E_F)^{1/2} \approx 2.2$ from the mean-field model and our independent measurement. Full

calculation that includes both RKKY and Efimov potential gives $a_{th} = -1,700\ a_0$ [42]. An independent confirmation of the fermi gas density enhancement comes from *in situ* images of Li degenerate Fermi gas. Enhanced Li density within the Cs BEC is observed with large interspecies attraction. A strong enhancement of the fermion density on the Cs BEC of $8 \sim 10$ for $-500\ a_0 < a_{\rm BF} < -1000\, a_0$ is observed, which corresponds to $\eta = 2.0 \sim 2.1$.

Contrasting the Cs BEC, Li degenerate Fermi gas behaves differently. Near the mediated resonance, Li trap loss is negligible, >10 times slower than the BEC decay rate. This supports the picture that Li atoms only 'catalyze' the collision resonance between Cs atoms. Pushing to even even stronger interspecies attraction, a distinct loss peak appears in the Fermi gas at $a_{\rm BF} = -1,800(200)\ a_0$. The resonance is persistent for different Fermion densities, and is clearly different from the Efimov resonance at $a_{\rm BF} = -3,300\ a_0$ [78] and the Fehsbach resonance at $a_{\rm BF} = \pm\infty$, both were precisely measured based on thermal mixtures of Cs and Li atoms. The observation of different resonance peaks are consistent with the physics picture indicated by Ref. 5.12.

5.4 RKKY-Efimov Transition across Critical Temperature

The theory section explores the transition of RKKY-Efimov crossover and it is appealing to obtain more experimental evidence to study the nature of this resonance. Especially, its relation with the Efimov resonance in the zero density regime. Yet as what mean field model on Fermi gas has shown, the fermion density is largely controlled by a_{BF} instead of initial fermion number. To further investigate the resonance processes, we track their evolution as the mixture transitions from the classical to the quantum regime. Starting with the mixture at the lowest temperature $T < 30\,$nK, we quickly step up the dipole trap intensity from 20% to 160% and wait for the mixture to reach the new equilibrium. This process provides precise heating of the sample without discernible trap loss. We then perform the trap loss measurement across the resonances, see Fig. (5.18).

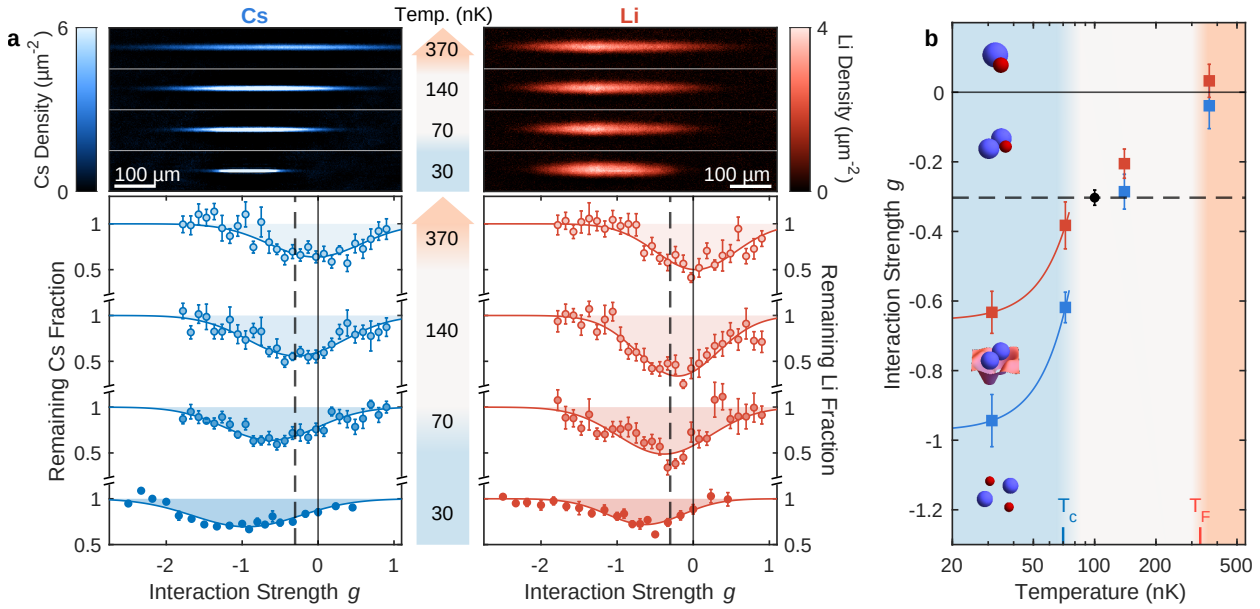

Figure 5.18: Fermion mediated resonances in the thermal and quantum regimes. (a) Sample images with 30,000 Cs atoms and 20,000 Li atoms are prepared at 30, 70, 140, and 370 nK. Lower panels show the Cs and Li surviving fraction after hold time $t_h = 2.8$, 3, 6, and 10 ms for the 30, 70, 140, and 370 nK samples, respectively. We determine the positions of the loss peaks from Gaussian fits (solid lines). (b) Summary of loss centers in the classical and quantum regime. Here $T_c = 75$ nK is the BEC critical temperature, and $T_F = 360$ nK is the Fermi temperature. Li loss centers are shown in red, Cs in blue. The black circle is the measurement from Ref. [78]. Red and blue solid lines are guides to the eye. Cartoons show the hypothesized many-body ground state: free Li (red balls) and Cs atoms (blue balls) for weak attractions $g < -0.9$, fermion-mediated Cs_2 pairs for $-0.9 < g < -0.6$ and Cs_2Li trimers for $-0.6 < g < 0$. Finally CsLi dimers form above the Feshbach resonance $g > 0$. In all plots, error bars are 1-σ standard deviations of the mean. The solid and dashed lines indicate the Feshbach and the Efimov resonance, respectively.

We observe drastic difference of the resonance positions when a thermal mixture enters the quantum degeneracy regime. At temperatures slightly above the Cs BEC critical temperature $T_c = 75$ nK, both species show the same Efimov resonance at $a_{\mathrm{BF}} = -3,300\ a_0$ and Feshbach resonance at even higher temperatures, in full agreement with previous works. Below the critical temperature $T_c = 75$ nK, on the other hand, the resonances start shifting toward weaker attraction and the difference of the resonances in Cs BEC and Li Fermi gas widens. The result is summarized in Fig. (5.18b). Linear extrapolation of the measurement in quantum degenerate regime suggests the resonances are shifted to to $a_{\mathrm{BF}} = -1,000\ a_0$ for Cs and to $a_{\mathrm{BF}} = -1,550\ a_0$ for Li at zerto temperature $T = 0$.

We propose a physical picture to elucidate the impact of quantum degeneracy to the Cs-Li mixture in the RKKY-Efimov transition regime. As we increase the interspecies attraction from zero, the Fermi gas first mediates bosonic attraction in the weak coupling regime through the RKKY mechanism. When the attraction reaches the first critical value ($a_1 = -1,000\ a_0$ in our system), the mediated potential is strong enough to pair two bosons, which we denote as

$$\mathrm{Cs} + \mathrm{Cs} \xrightarrow{\text{Li DFG}} \mathrm{Cs}_2. \tag{5.15}$$

Further increase of the attraction hits the second critical value ($a_2 = -1,800\ a_0$ in our system), where lithium atoms are bound to the boson pairs, which we denote as

$$\mathrm{Li} + \mathrm{Cs}_2 \xrightarrow{\text{Li DFG}} \mathrm{Cs}_2\mathrm{Li}. \tag{5.16}$$

Both of the processes are many-body in nature. In a thermal gas, on the other hand, the two processes occur simultaneously and become one: Cs+Cs+Li$\rightarrow$Cs$_2$+Li, which is precisely the physical picture of an Efimov resonance. Our picture offers a consistent explanation of previous works on Li-Cs mixtures, and highlights the new fermion-mediated pairing of the Bose-Fermi mixture in the strong coupling regime. In Fig. (5.19) I propose an understanding

of the physics happening in different regimes of a Bose-Fermi mixture.

We use the temperature as a tuning parameter to study the Efimov-RKKY transition. Yet here I would like to emphasize that changing of temperature has at least two important effects on the mixtures: first, a BEC with highly thermal fraction is less able to attract more fermions in its center, thus losing the local fermion density enhancement. This is more in line with the consideration of fermion density. On the other hand, the temperature will indeed have a strong effect on the mean bosonic separation R as well as the 'sharpness' of Fermi surface. The topic of temperature is important here and the related theories are a bit away from my scope of knowledge [102] [167]. To have a rough physics picture, as the temperature increases from 30 nK to around 100 nK, the Cs cloud reduces in density and loses the density enhancement effect, shifting the resonance back to stronger interaction. In the meanwhile, this temperature is not high enough to destroy the Fermi surface. Therefore we still observe a separation of loss feature peaks of Li and Cs. Eventually, things decay back to Efimov resonance and the two peaks overlaps, few body physics overcome many body physics. At even higher temperature, the Fermi surface is not 'sharp' and the behavior of the mixtures returns to thermal gas limit. The temperature also washes out the Efimov resonance signal and leaving only the Feshbach resonance feature. Yet I would like to claim that besides two body pairing, there are many other theory proposals in this regimes, such as Bose-Fermi droplet [89] [124] [84] [90], three body braiding state [49], I would not argue the pairing theory must be the ultimate correct picture.

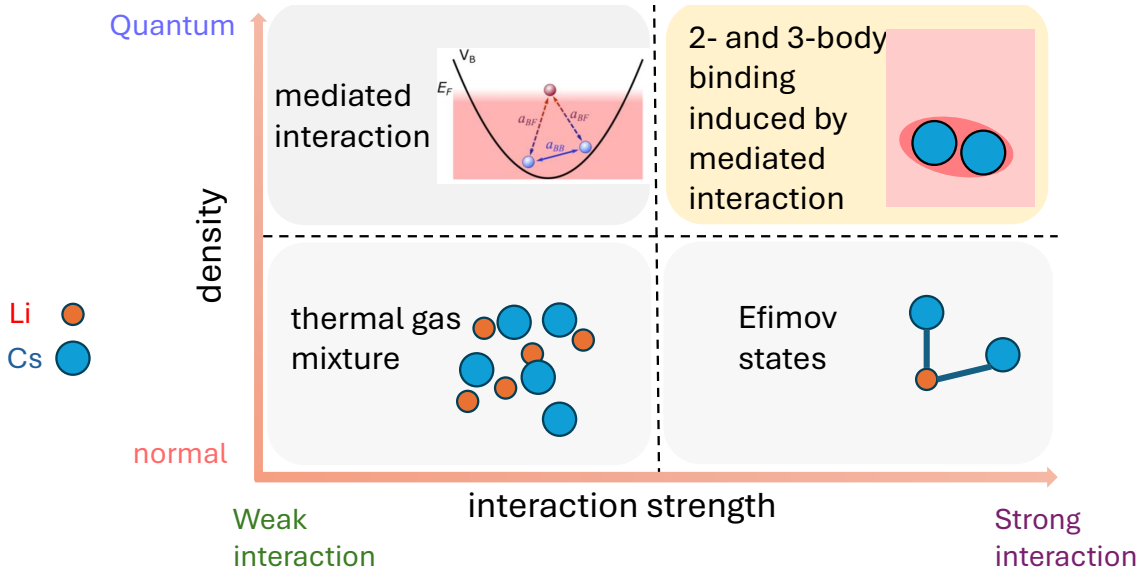

Figure 5.19: A general summary of Bose-Fermi mixtures in different regimes. At weakly interacting, low density normal regimes, the Bose-Fermi mixtures are well described by ideal thermal mixture gases. Starting from normal and weakly interacting, the Li-Cs experimental system has explored many different aspects of Bose-Fermi mixture. At parameter regime where the Bose-Fermi mixtures are still dilute but strongly interacting, heteronuclear Efimov states emerges. Instead, when Bose-Fermi mixtures are in weakly interacting quantum regime, we firstly observe fermion mediated interaction in quantum gases. After studying sound excitations, we finally went to where the Bose-Fermi mixtures are quantum and strongly interacting. Here we observed a novel two-body and three-body resonances from many body effect of fermion mediated interaction, along with a detailed study on how such transition relies on density. I believe, there still will be numerous theories and discussions about Bose-Fermi mixtures in future.

CHAPTER 6

OUTLOOK

6.1 BCS-BEC Mixtures and 80MHz RF Coil

Though Bose-Fermi mixture systems are relatively less explored in compared with other cold atom platforms, research in this field has been ongoing for more than two decades. On the other hand, a two-components Fermi gases with BEC are far less explored. At this point, there are many successful example yet awaiting further investigation due to the lack of interaction tunability of existing example. The earliest success realization being two components ^{6}Li with ^{7}Li BEC by Salomon group [73]. Later examples are followed by ^{6}Li and ^{174}Yb from Subhadeep Gupta group [125] and ^{41}K and ^{6}Li from Jianwei Pan group [162]. A similar BCS-BEC combination could be realized in our setup as well. With an addition of a anisotropic RF coil [43] operating at 80MHz, we can address the Li $|a>$ into other states with at Rabi frequency which is even faster than our carefully engineered magnetic field jump. Compared with already realized systems mentioned above, one key advantage of ^{6}Li and ^{133}Cs is that it has tunability in interaction strength, see Fig. (6.1).

The last paragraph is about methodology to realize Li-Cs BCS-BEC mixtures as well as sharing unsuccessful experience. There are multiple paths to achieve two component Fermi gases, including a direct trap mixing of two components BCS Li mixing with thermal Cs and do further evaporation, 80 MHz RF transfer and two photon Rabi process. Among them, I would firmly recommend using 80MHz RF coil instead of trying to do trap transfer and mixing. As the RF Landau-Zener sweep method is being verified by above mentioned groups, do sympathetic cooling is more challenging. On the one hand it requires a much longer sample lifetime whereas additional atom loss channels come from on more fermion component could lead to the exact opposite. On the other hand, at the magnetic field where Cs are not strongly interacting with both Li species, its own scattering length is small

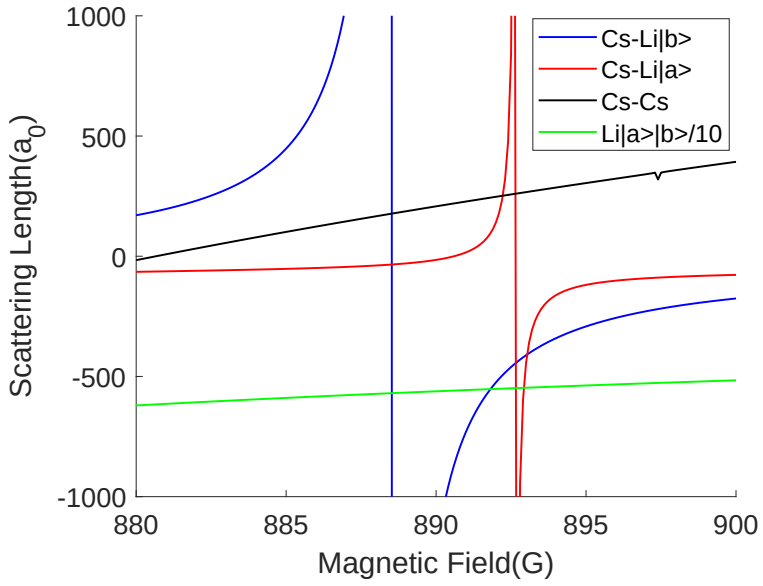

Figure 6.1: Relevant scattering lengths around a stable Bose-Fermi mixtures are possible.

therefore hurting its own evaporation cooling process. Lastly, since trap transfer and mixing Cs and Li are already a quite challenging process, philosophically it is a not a good idea to build in a fragile steps into experimental sequence. Both I and Krutik Patel haven't got a successful realization of BCS-BEC mixture during our PhD career. At least, I tried for two weeks without any sign that would work. I am not discouraging people in future give a try as but one should bare in mind the potential risk from this seems easier path. Instead, even if Li-Cs BCS-BEC mixtures have very short lifetime, a 80MHz RF coil still enables many spectroscopy measurement as well as possibility to explore other states.

6.2 Bose-Fermi vortex and Pancake trap

Our current dipole trap configuration is in a quasi-1D cigar shape. Though it brings with advantage of ease in implmentation and trap mixing of bosons and fermions, it comes with the price of limiting possible science we could study. Implementing a pancake trap as the Cs lab does could be a good idea. A 2D pancake trap formed by optical lattice could provide enough trapping potential to confine fermions, producing a 2D Bose-Fermi mixtures. This

will largely increase the effect of mediated interaction (see next section). On the other hand, vortex in Bose-Fermi mixtures is an interesting thought. Especially, how BEC vortex inside a Fermi gas dissipates. Besides, this system attracts many interests from the theorists community [13] [77].

It also worth a mention that with my continuous optimization over the years, the maximum fermion number has reached 25 000 from 6000. Though further optimization is possible, currently the greatest limitation being the lack of sub-Doppler cooling in the early stage. The above and some other proposals might requires a much higher fermion number in the mixtures. Since now we have abundant spare laser power at 671nm, it is not a bad idea to schedule for long term Li gray molasses[62] updates. With gray molasses cooling, one can cool the Li down to about $60\mu k$ instead of current $300\mu k$, this would allow us to increase the BFL trap capture volume and easily increase our final number by a few factor.

6.3 Dimensionality of Fermi Gas and Optical Lattice

Coupling between BEC excitations and particle-hole excitations near the Fermi surface is the basic building block of most of phenomena we have studied so far. In this context, the 'sharpness' of the Fermi surface is critical. In fact, 2D or even 1D Fermi surface offers a much prominent effect from the fermions [104]. Implementing optical lattice could also alert the property of Fermi gas and enable such research [75]. Before we further dive into possible research topics, I provides some estimates about what will happen if we retro our current final 1064nm dipole trap. Assuming we reflect 40% of the beam power, we will get a lattice depth of 40 recoil energy. The mean field energy shift coming from BEC itself $nU/\hbar$ is about 300Hz for a BEC with chemical potential of $50nK$. The finite size effect causes signal broadening

$$\Delta v_R = \sqrt{21/8}\ q/2\pi m_B R_{TF} \tag{6.1}$$

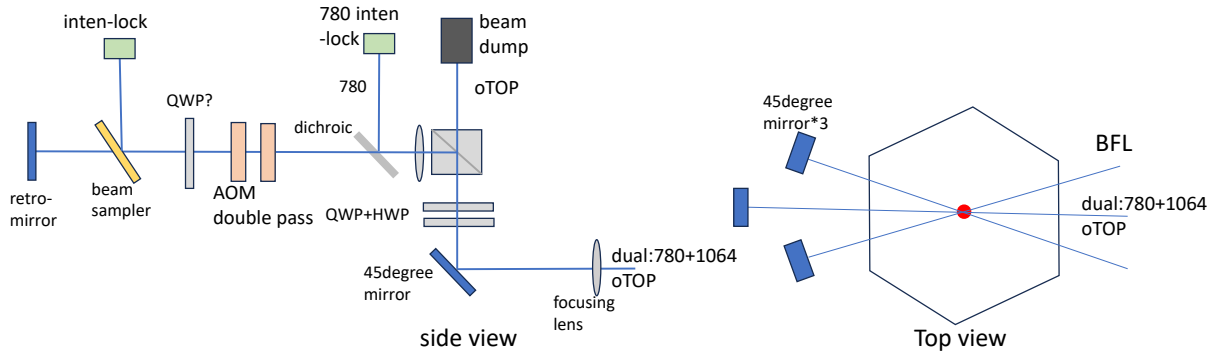

Figure 6.2: A possible schematic of optical lattice layout

here q is twice the lattice momentum, m_B being boson mass and R_{TF} being the Thomas-Fermi radii. On the other hand, inhomogeneity of BEC is another source of broadening:

$$\Delta v_n = \sqrt{8/147}\, g_{BB} n_B/\hbar \tag{6.2}$$

Here g_{BB} is boson-boson interaction strength and n_B is boson density. Density inhomogeneity contributes a frequency broadening of about 80Hz, see Ref. [145] for more details. Fig. (6.2) shows a possible layout for this future optical lattice, yet actual engineering such lattice involves in decent technical challenges, ranging from lattice beam stability, retro beam wavefront aberration to limited space and the need to separate beams from different dipoles traps.

6.4 Further Questions from Fermion Mediated Pairing Project

• Ultra high fermion density Bose-Fermi mixtures

Both from Tilman Enss model [42] and other theory proposals, Ref. [101] for example, suggest that the Efimov Cs-Cs mediated pairing as well as the Efimov resonance will be blocked by a Fermi gas which is 100 times denser than the fermion density of a non-interacting Fermi gas. Apparently such density is not possible with current setup, but could be under consideration if in future 2D Fermi gas or even 1D Fermi gas system are realized.

• Effective three-body repulsion on Fermi gas and Fermi gas momentum halo:

Let's consider a Li-Cs bose-fermi quantum degenerate mixture with strong attractive interaction. The BEC is embedded in a reservoir of degenerate fermi gas. The attractive interaction $a_{BF} < 0$ is chosen such that it causes a strong repulsion in between two bosons. If we consider the total energy of the system, there two competing processes: I. Fermions from the reservoir move into the BEC, due to mean field attraction. II. The BEC prefers less fermions inside it, since the fermion-mediated interaction causes a sharp rise in a_{eff}, therefore increasing the mean field energy of the BEC $E = g_{\text{eff}} n_B N_B$. The question is: If the induced a_{eff} is strongly repulsive, then would the system choose to lower the fermion density inside BEC, in order to lower the energy of the system? i.e., the BEC repels fermions with strong attractive interaction? It implies there is a possible effective repulsion between bosons and fermions due to this 3-body interaction. Further more, if one check the effective scattering for fermion in the continuum, one can find strong repulsion on fermion with near zero momentum. It can be understood as Pauli exclusion from the fermion in bound state. In other words, in the entire Fermi gas, the fermions with near zero momentum are repelled from the BEC, forming a hole inside the Fermi sea. This conjecture could possibly be verified by some short time TOF(time-of-flight) measurement on fermions.

• Proper normalization of Efimov potential(theory problem).

Computing fermion induced effective scattering between Cs atoms relies on including both contribution from the bounded fermion (Efimov) and fermion in continuum. One needs to cutoff the Efimov potential properly for regularization reason. Yet such regularization screens the short range RKKY potential and hurt the prediction. Searching for a proper way to regularize the Efimov potential is a good idea. Furthermore, the effect of narrow Li-Cs Feshbach resonance is used in the project, its impact on theory prediction hasn't been thoroughly discussed.

APPENDIX A

TAPERED AMPLIFIER MAINTENANCE

A.1 Basics on Tapered Amplifier

I sincerely wish you are reading this section for fun, instead of in actual need of repairing a Toptica tapered amplifier (as I was). This appendix will first give a briefing of general working principle of lasing semiconductor and laser diode, followed by a detailed Toptica maintenance guide.

It is a good reminder for the reader that most of common lasers products including ECDL (external-cavity diode lasers), TA (tapered amplifiers), DBR lasers (distributed Bragg reflector) or VECSEL (vertical external-cavity surface-emitting laser) even a multi-mode multi-frequency high power diode bars, are based on energy band gaps with doping and population inversion. The differences arise from the choice of coating and the physical layout inside the semiconductors. For example, common laser diodes used for homemade ECDL is high reflection(HR) coating on its rear and antireflection(AR) on its output, in order to form a cavity with the external grating. The active area of a laser diode is a elongated rectangular area, to ensure single mode output. DBR lasers typically rely on a periodic structure in the refractive index (not just doping concentration) to form a distributed Bragg reflector and therefore result in a pre-determined output wavelength. A VECSEL, on the other hand, is HR coating on its largest surface and emitting photons in a direction which is perpendicular to a traditional laser diodes. Further discussion on laser diodes is out of the scope of this technical manual and I will direct reader to the review by Carl E. Wieman and Leo Hollberg [67] for in depth discussion, different aspects of laser diodes such as laser diodes aging are included there.

Population inversion, stimulated emission and energy band gaps are the most important principles behind lasing. While the former two concepts are usually well familiar by reader

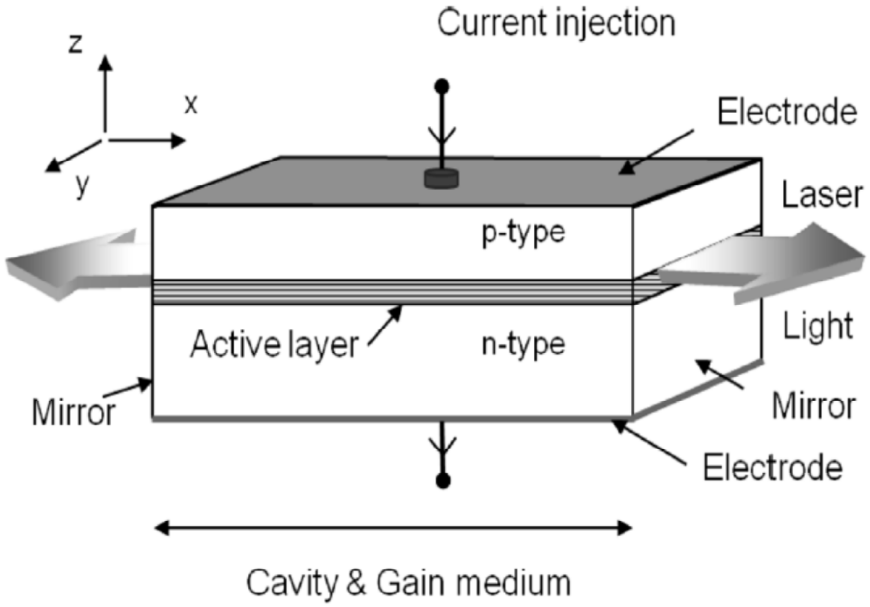

Figure A.1: Schematic of a laser diode. Picture adopted from Ref. [81]

in AMO physics, the latter could be an unfamiliar topic. As a semiconductor, a laser diode is built on a wafer, with a much smaller actual light emitting region in comparison. That region is consists of substrate region and active region, see Fig. (A.1). The physical structure of a laser diode is extremely elongated: along lasing direction, the cavity could be as long as $\sim 500\mu m$, and the perpendicular direction as wide as $\sim 100\mu m$ with its size constrained by the demand of producing a single spatial mode. However, the tight axis where pumping current pass through is only a few micron wide, and the active area, where the photon emits is as thin as $10 - 200$nm. At this extremely thin junction, there is a voltage drop of about $1 - 2$V drop and a current of few hundreds of milliamps. This is saying, aside from energy of emitted photons, the rest is dissipated heat at this junction, which explains why laser diodes are so thermally sensitive to driving current and could break so easily. Across the PN junction, a bias voltage close to the energy band gap is applied, which causes electron population inversion accompanied by radiative electron-hole recombination. The energy band gap is determined by the material of semiconductor, for example, InGaN(Indium doped gal-

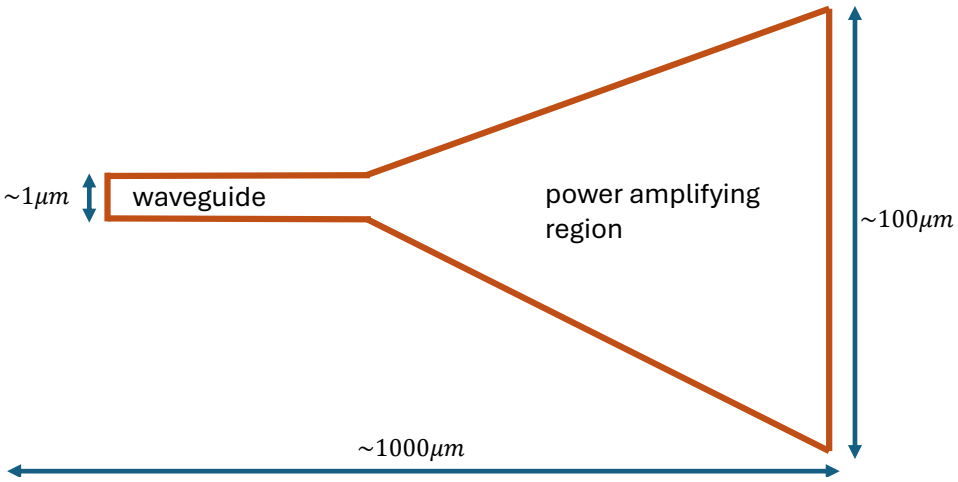

Figure A.2: TA structure, observing direction in perpendicular to active area.

lium nitride) is what behind the famous blue light-emitting diode, and AlGaInP(Aluminum Gallium Indium Phosphide) is used for red lasers. While the band gap of the material determines the bulk part, changing doping concentration will fine tune the lasing wavelength, within the range permitted by properties such as lattice strain and lasing efficiency. On the top all these, the PN junctions are not as what's simply shown in Fig. (A.1), it is built with sophisticated vertical and lateral structures such as grooves and insulating side blocks. These structure are designed with many purposes. For example, engineering an undoped material sandwiched by PN junction forms quantum wells which increases overlap in between active area, photon field and electric field. This increases the photon concentration to dominates over spontaneous emission and increases lasing efficiency. Engineering some certain groove structure helps getting a single spatial mode and determines the dominant polarization (if you ever wonder about what's the origin of laser diode's output polarization). There is far more knowledge about laser diode engineering as I listed here, I would recommend Ref. [81] for more in depth discussion.

A TA is part of MOPA(Master Oscillator Power Amplifier) configuration. Look perpendicular to its active layer, the structure of TA is shown in Fig. (A.2). Two ends of the TA chip are AR coated on both ends to ensure it amplifies the power from seeding laser only

once. The injection end of TA is narrow and long with width of few microns. It serves as a waveguide to filter out spatial modes other than TEM00. However, since such waveguide is not long enough, it can not filter out unwanted spatial modes as good as an optical fiber can do, and this is one of the reason why tweaking angle of injection seeding will affect TA output mode. A wedge shape gain medium follows after the waveguide, with its width increasing gradually until as wide as few hundreds microns near the output. The length of active area determines the TA output power, which is on the order of millimeter and largely limited by factors such as thermal stress. Both heat and optical power are highly concentrated on this tiny region. Take a typical 670nm Eagleyard TA for example, it dissipates about 0.5W of heat and outputs 0.5W of red light. It is not hard to imagine why TA chips require sealed dustless space and good cooling to work properly. As it will be shown later, Toptica has a paradigm design for such requirement.

It is worth a mention that, TA chip at 670nm is a special case. While TA chips at most wavelengths have a quite high gain, properly due to thermal stress consideration, the gain of 670nm chip is usually very low. Therefore, Li TA chip requires higher seeding power and featuring lower output power. When it comes to commercial sources of 670nm lasers, while Eagleyard@Toptica and Sarcher offer traditional MOPA systems, Vexlum offers VECSEL and Precilaser offers solution based on SHG(second harmonic generation) Raman fiber amplifier.

A.2 Toptica TA Repairing

This section describes how to service the Toptica laser when the TA chip fails. I will first introduce the structure of the Toptica laser layer by layer. Fig. (A.3) is what you will see when you open the laser (one isolator is taken down in the photo, though). The brass block named as 'TASK', by Toptica and we will follow this convention. The 'TASK' is consists of a circuit board, a TEC(thermoelectric cooler), a brass block. The brass block is what seals the

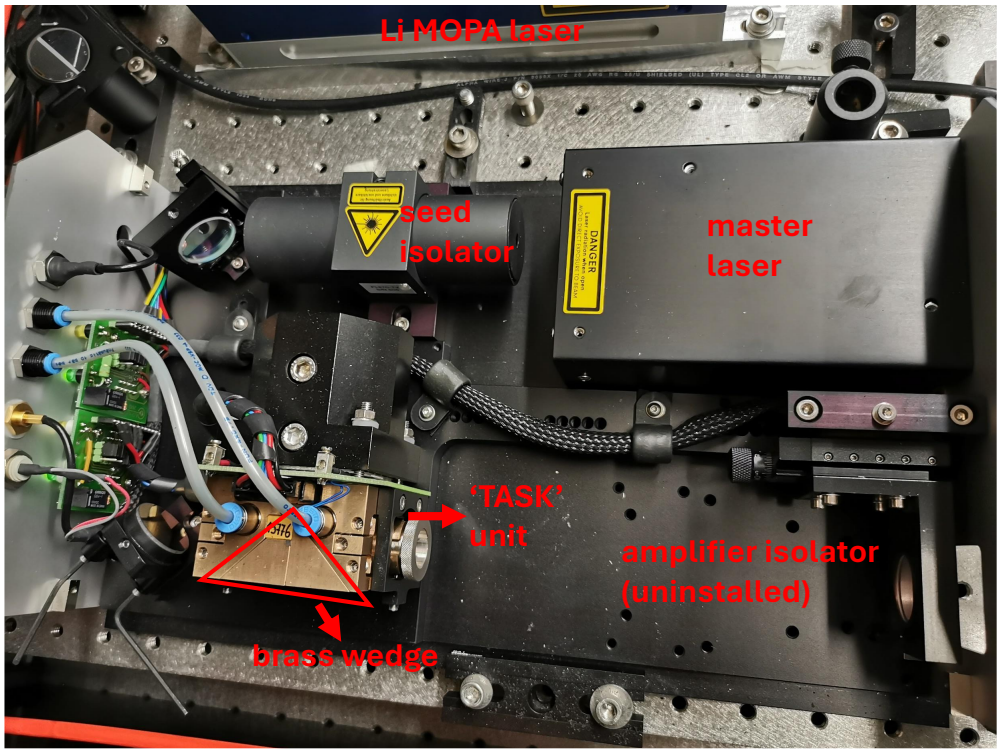

Figure A.3: Toptica MOPA TA layout. The 'TASK' unit is where the TA chip locates.

TA chip. The entire unit is mounted sideway with one of the TEC surface connected with the anodized aluminum block. The rectangular 'TASK' block is directly connected with one of TA chip's polarity, so do perform ESD precautions before any operation. The brass block of 'TASK' unit has two brass wedges to hold a gold bone firmly (gold bone being another unofficial Toptica naming, which refers the TA chip mounting metal coated in gold, as shown in Fig. A.6). Fig. (A.5-a) shows what's inside 'TASK' unit when the two brass blocks are taken out. There are two coupling aspheric lens(sometimes they even can be microscopy) for input and output coupling with a threads for z-axis tuning. In the middle of the brass unit sits the 'gold bone', which is a metal piece coated with gold, for the reason that gold is resistant to oxidization compared with copper or silver and in the meanwhile a good thermal and electric conductor. On the gold bone mounted the TA chip, with a bulk part of it being a mounting ring with a tiny screw fixing the TA chip. To ensure electric conductivity and good thermal dissipation, as well as eliminate dust and dirt, a $75\mu m$ Indium foil is sandwiched

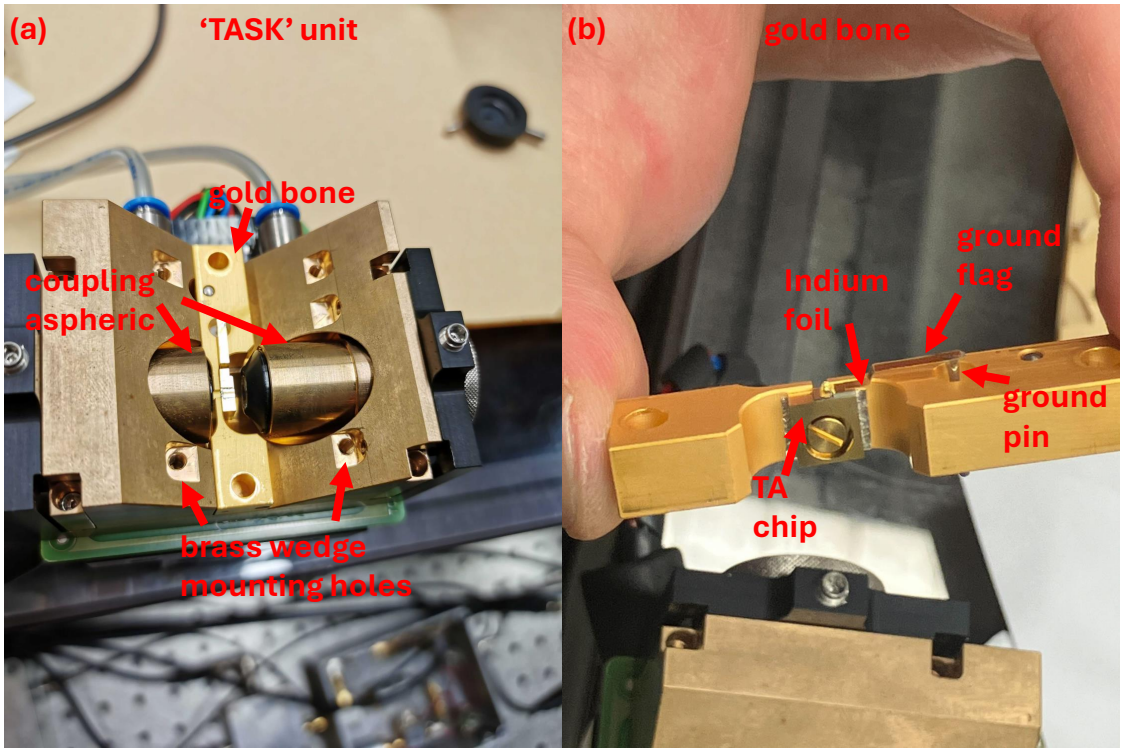

Figure A.4: Layout inside the 'TASK' unit. The 'brass wedge' refers to where the two wedges sits

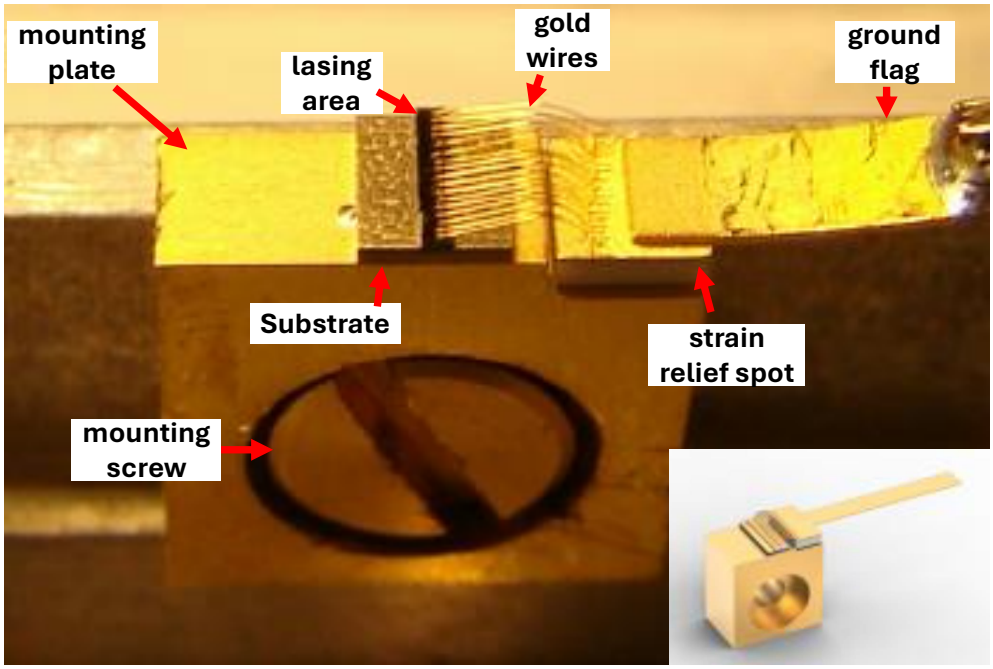

Figure A.5: Structure of Eagleyard TA chip. The photo is adopted from [144] to illustrate the structure of TA chip. The inset picture comes from dataset of Eagleyard Toptica

Figure A.6: Photo from another angle showing the TA chip structure mounted on the gold bone. This picture is adopted from Eagleyard Toptica's website

between the gold bone and TA chip since soft Indium will properly fill the gaps in between serving as thermal paste. On the right, there is a ground pin soldered (sometimes connected by conducting glue) with ground flag. The ground flag carries nearly one ampere current to the TA chip. Fig. (A.5) is a photo of TA chip (adopted from Ref. [144] since I don't have a clear picture). The ground flag is connected to a strain relief spot, which is fixed by insulating material. TA driving current is then distributed by multiple gold wires to so as to uniformly distributed the current onto one junction of TA chip. The really tiny black stripe is what's the lasing unit is. As described in previous section, it is around half millimeter long, around one hundred micron wide and few microns thick. The lasing unit sits on a slightly larger block of substrate. Starting from now, I will introduce a TA chip swapping procedures.

Preparation and Soldering

• **Dust proof** To ensure a dust-minimized environment, I recommend mopping the floor and cleaning tables in the workspace where is TA chip or 'TASK' unit is exposed without a cover protection.

• **ESD caution** Since the TA chip is much fragile than usual electronics, a much higher level of ESD caution should be implemented. Not only the personnel, the relevant optical table and soldering station should be properly grounded, but also ESD caution should be implemented during transportation between platforms. I will recommend covering the TA chip with a

Faraday cage during transportation, and the personnel should ground himself/herself first before touch the TA chip after transportation. This manner will maximally reduces the risk from accumulated charge during people's motion.

• **Solder temperature** Soldering of ground flag should follows the 330°C/10s rule, so please check the melting point of solder and set the solder iron to 330°C. Double check to ensure that my recommendation of 330°C for 10 seconds here, aligns with manufacturer specifications for this specific chip.

• **Tools and material** Cut a few Indium foils, measure their size to ensure this is what needed. Besides, cut a proper size hole on the foils to let the mount screw go through it. Prepare a solder smoke absorber/remover to prevent solder smoke pollution on optical surface. Tweezers. Screw drivers. Soldering iron. Compressed air duster.

• **TA driver current limit and polarity** I recommend set the current limit and check TA polarity earlier.

• **Rehearsal** Before installing a new TA chip, I would highly recommend doing few rounds of rehearsal to familiarize the personnel of all the procedures.

• **Soldering** Make sure the soldering spot and the solder iron are placed in the downstream of air current created by solder smoke absorber/remover to avoid solder smoke pollution. After grounding yourself, use tweezer to place a Indium foil on gold bone and then place the TA chip on it. Screw in the mounting screw with tweezer holding the TA chip to minimize TA chip motion. Then mount the gold bone and make sure the ground flag and ground pin are touching with mechanical spring force from the ground flag. Secure the gold bone, solder the flag and pin together following 330°C/10s rule so that the TA chip won't get burnt. After soldering, turn off solder iron and use duster to blow the gold bone and 'TASK' unit before you install the gold bone back.

TA Alignment

After successful soldering, install gold bone back to 'TASK' unit and secure it with the

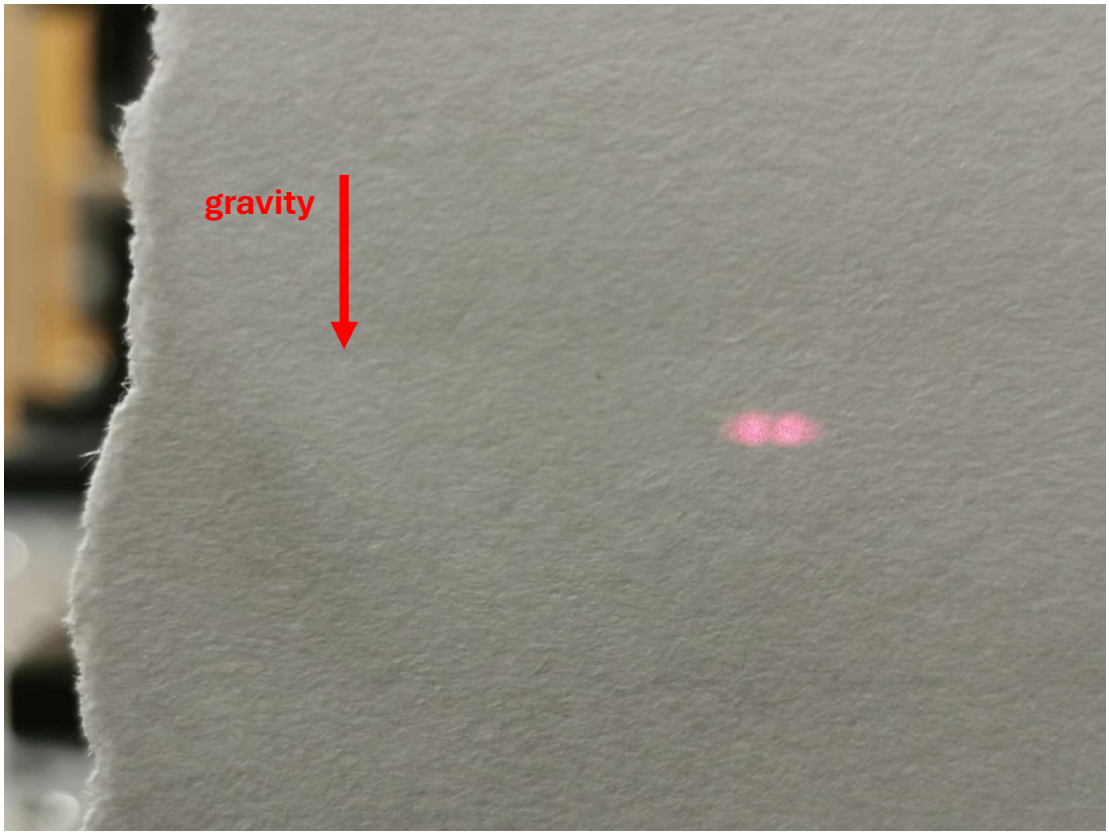

Figure A.7: Appearance of seed light transmitted through TA chip, when seed is properly injected and TA chip current is turned off. One can also check the shape of transmitted seed light from other TA to get a sense. Recall that here the $\sim 100\mu m$ axis of chip is mounted vertical(gravity). The active area in this direction absorb the incoming photon since they are the exact right wavelength. On the other hand, in horizontal direction, the seed beam can travel through the non-active area of the either the P or N junction without be absorbed. Therefore, the transmitted seed light has a two-dots structure in horizontal direction.

two brass wedges. TA alignment is realized by tweaking the group of set screws and z-axis adjustment of aspheric lens mount. TA chip requires clean environment so these tweaking are purely based on mechanical adjustment of screw threads. However, in the meanwhile, the size of TA chip naturally requires a high resolution and accuracy from your tweaking and this is why TA alignment could be painful. This application note from Toptica is a good guidance [150].

• **Input beam** Check input beam shape and power, align the input beam parallel with the TA output. The desired beam shape for the TA chip is indicated by the back-propagating ASE(Amplified spontaneous emission) from the chip. Spatial mode shaping is necessary if the injection beam is not ideal.

• **Alignment with ASE** ASE(Amplified spontaneous emission) is the alignment guide beam in this step, as it tells beam direction and shaping coming out of TA chip. Install the 'TASK' unit back onto laser system, turn off seed laser and set a low TA current(100 mA, for example). ASE from TA chip emits from both direction facets of TA chip. Use the back propagating ASE to coarse align the input aspheric lens and use the ASE from TA output to coarse align the output aspheric lens.

• **Further Injection Alignment** Turned off TA current and turn on seed light. Coarse align the injection light so that you observe pattern similar in Fig. (A.7). Since there is many other structure(e.g. gold wires) near the TA chip, you will often observe very confusing pattern. Note that we want the input coupling aspheric to be aligned well, which can not be achieved by tweaking angle of injection mirror, so please be patient here.

• **Injection fine alignment with photocurrent** Since current traveling across PN junction produces photons at 670 nm, vice versa. We use photocurrent from seed laser absorbed in the active area to maximize injection coupling. Toptica TA circuit board has a D-sub9 output. There are pins for driving current and pins for diagnostic, the latter is connected to the TA chip in series with a 1 kΩ resistor. I would recommend do fine alignment looking at photo-

voltage to minimize risks of ESD killing. As described in Ref. [150], maximizing the photo voltage is not enough as there are two false local maximum peaks when seed light is coupled into the wedge shape gain medium through the non-active substrate sandwiched the mode filtering waveguide, as indicated by Fig. (A.2). As a reference, when I have the correct and maximized injection coupling with 12 mW of seeding light, the 6-digits multi-meters reads 164 µV.

• **Beam shaping and output power calibration** Since isolators sometimes distorts beam shape, first install the amplifier isolator and then adjust beam shape. Remember TA output has strong thermal effect so adjust beam shape at aimed operating current. Output power calibration, such as output power verses current, output power verses injection power and ASE power versus current are useful information to record. Tab. (A.1)(A.2)(A.3) shows the TA output performance after the new chip is installed.

TA current (mA)	**ASE power(mW)**	**TA output(mW)**
0	0.040	0.090
50	0.159	0.227
100	0.340	0.458
150	0.577	1.620
200	0.868	7.69
250	1.213	23.52
300	1.615	48.2
350	2.072	78.8
400	2.599	113.8
450	3.18	150.4
494	3.74	183.2

Table A.1: TA output without isolator. The seeding power is 12mW.

TA current(mA)	**ASE(mW)**	**TA output(mW)**
0	0.045 (room light)	0.1 (room light + seed transmission)
50	0.121	0.15
100	0.251	0.266
150	0.425	1.08
200	0.643	6.29
250	0.899	20.16
300	1.210	41.6
350	1.565	68.9
400	1.978	99.6
450	2.435	132
500	2.97	164.5
550	3.53	196.6
600	4.17	227.8
650	4.87	258.4
700	5.63	287
750	6.50	314
800	7.34	339
850	8.28	366
900	9.27	396
950	10.32	424
1000	11.36	447

Table A.2: TA output after isolator. The seeding power is 12mW.

Injection Power (mW)	0	2	4	6	8	10	12.3
Master Current (mA)	0	69.8	73.4	76.6	80.3	84.9	88.4
TA Current (mA) / TA Output (mW)							
250		3.48	6.90	9.90	12.64	15.17	17.16
300		9.65	16.98	24.41	29.6	34.2	38.0
400		36.7	55.7	72	79.7	86.2	99.6
600		122.1	160.9	191.8	201.7	216.7	223.2
800		197.5	273.5	305	323	327	336

Table A.3: TA output after isolator, at different injection power

APPENDIX B

MISCELLANEOUS

Here are few more things future members may be interested in:

• **NI Card and LabVIEW Control** I wrote a very rough report in OneNote under tab 'Control PC' → 'Guide for NI card and channel'. This is a summary of LiCs lab National Instrument(NI) card physical layout as well as a guide through the LabVIEW program. It also records the history of different PC channel groups and old NI card. Refer to that section if you ever need to make some change about PC control.

• **Field Theory of Bose-Fermi mixtures** I wrote Matlab script 'dispersion_bf.m' for computing BEC quasi-particle energy and damping at finite momentum with weakly coupling field theory based on Ref. [170]. On the other hand, it is much complicated to write code based on strong coupling field theory, see Ref. [139].

APPENDIX C

LIST OF PUBLICATIONS

(1) B.J. DeSalvo, Krutik Patel, **Geyue Cai**, and Cheng Chin. Fermion-Mediated Interactions Between Bosonic Atoms. Nature 568, 61 (2019)

(2) Krutik Patel, **Geyue Cai**, Henry Ando, Cheng Chin. Sound Propagation in a Bose-Fermi Mixture: From Weak to Strong Interactions. Phys. Rev. Lett. 131, 083003 (2023)

(3) **Geyue Cai**, Henry Ando, Sarah McCusker, Cheng Chin. Fermion mediated pairing in the Ruderman-Kittel-Kasuya-Yosida to Efimov transition regime. ArXiv:2502.06266 (2025)

REFERENCES

[1] B Abi. Measurement of the positive muon anomalous magnetic moment to 0.46 ppm. *Phys. Rev. Lett.*, 126:141801, 2021.

[2] David DeMille John M. Doyle Gerald Gabrielse Yulia V. Gurevich Paul W. Hess-Nicholas R. Hutzler-Emil Kirilov Ivan Kozyryev Brendon R. O'Leary Cristian D. Panda Maxwell F. Parsons Elizabeth S. Petrik Ben Spaun Amar C. Vutha Adam D. West ACME Collaboration: Jacob Baron, Wesley C. Campbell. Order of magnitude smallerlimit on the electric dipolemoment of the electron. *Science*, 2014.

[3] Jean-Philippe Aguilar, Eduardo de Rafael, and David Greynat. Muon anomaly from lepton vacuum polarization and the mellin-barnes representation. *Phys. Rev. D*, 77: 093010, 2008.

[4] A.P. Albus, S. A. Gardiner, F. Illuminati, and M .Wilkens. Quantum field theory of dilute homogeneous Bose-Fermi mixtures at zero temperature: General formalism and beyond mean-field corrections . *Phys. Rev. A*, 65:053607, 2002.

[5] William I. McAlexander Guthrie B. Partridge Andrew G. Truscott, Kevin E. Strecker and Randall G. Hulet. Observation of fermi pressure in a gas of trapped atoms. *Science*, 2001.

[6] M. R. Andrews, D. M. Kurn, H.-J. Miesner, D. S. Durfee, C. G. Townsend, S. Inouye, and W. Ketterle. Propagation of sound in a bose-einstein condensate. *Phys. Rev. Lett.*, 69:553, 1997.

[7] Ilya Esterlis Steven A. Kivelson Andrey V. Chubukov, Artem Abanov. Eliashberg theory of phonon-mediated superconductivity — when it is valid and how it breaks down. 2020.

[8] V V Babikov. The phase-function method in quantum mechanics. 1967.

[9] Gillen J. Peng A. et al Bakr, W. A quantum gas microscope for detecting single atoms in a hubbard-regime optical lattice. 2009.

[10] J. B. et al. Balewski. Coupling a single electron to a bose–einstein condensate. 2013.

[11] J. Bardeen, L. N. Cooper, and J. R. Schrieffer. Microscopic theory of superconductivity. *Phys. Rev.*, 106:162–164, Apr 1957. doi:10.1103/PhysRev.106.162.

[12] G. Buchler, H. P. Blatter. Supersolid versus phase separation in atomic bose-fermi mixtures. 2003.

[13] A. M. Belemuk, N. M. Chtchelkatchev, V. N. Ryzhov, and S.-T. Chui. Vortex state in a bose-fermi mixture with attraction between bosons and fermions. *Phys. Rev. A*, 73: 053608, May 2006. doi:10.1103/PhysRevA.73.053608. URL `https://link.aps.org/doi/10.1103/PhysRevA.73.053608`.

[14] A.M. Belemuk and V.N. Rhyzov. Stable and unstable regimes in bose-fermi mixtures with attraction between components. *Phys. Rev. A*, 76:013609, 2007.

[15] A.M. Belemuk and V.N. Rhyzov. Effective hamiltonian study of excitations in a boson-fermion mixture with attraction between components. *J. Phys. B: At. Mol. Opt. Phys.*, 43:225031, 2010.

[16] M. et al. Berninger. Feshbach resonances , weakly bound molecular states , and coupled-channel potentials for cesium at high magnetic fields. 2013.

[17] Manuel Gerken Eleonora Lippi Bing Zhu Juris Ulmanis Moritz Drescher Manfred Salmhofer Tilman Enss Matthias Weidemüller Binh Tran, Michael Rautenberg. Fermions meet two bosons – the heteronuclear efimov effect revisited. *Braz J Phys*, 2020.

[18] Barry Bradlyn and Andrey Gromov. Supersymmetric waves in bose-fermi mixtures. *Phys. Rev. A*, 93:033642, 2016.

[19] M. Bruderer, T. H. Johnson, S. R. Clark, D. Jaksch, A. Posazhennikova, and W. Belzig. Phonon resonances in atomic currents through bose-fermi mixtures in optical lattices. *Phys. Rev. A*, 82:043617, 2010.

[20] Martin Bruderer, Alexander Klein, Stephen R. Clark, and Dieter Jaksch. Polaron physics in optical lattices. *Phys. Rev. A*, 76:011605(R), 2007.

[21] Y. Castin and R. Dum. Bose-einstein condensates in time dependent traps. *Phys. Rev. Lett.*, 77:5315–5319, Dec 1996. doi:10.1103/PhysRevLett.77.5315. URL `https://link.aps.org/doi/10.1103/PhysRevLett.77.5315`.

[22] Cheng Chin. Universal scaling of efimov resonance positions in cold atom systems. 2011.

[23] Cheng Chin. Universal scaling of efimov resonance positions in cold atom systems. 2011.

[24] Cheng Chin, Rudolf Grimm, Paul Julienne, and Eite Tiesinga. Feshbach resonances in ultracold gases. *Rev. Mod. Phys.*, 82:1225, 2010.

[25] Cheng Chin, Rudolf Grimm, Paul Julienne, and Eite Tiesinga. Feshbach resonances in ultracold gases. *Rev. Mod. Phys.*, 82:1225–1286, Apr 2010. doi:10.1103/RevModPhys.82.1225. URL `https://link.aps.org/doi/10.1103/RevModPhys.82.1225`.

[26] L. et al. Chomaz. Quantum-fluctuation-driven crossover from a dilute bose-einstein condensate to a macrodroplet in a dipolar quantum fluid. 2016.

[27] S.T. Chui and V.N. Rhyzov. Collapse transition in mixtures of bosons and fermions. *Phys. Rev. A*, 69:043607, 2002.

[28] V. N. Chui, S. T. Ryzhov. Collapse transition in mixtures of bosons and fermions. 2004.

[29] Isabella Fritsche Erich Dobler Gregor Anich Emil Kirilov Rudolf Grimm Miguel A. Bastarrachea-Magnani Pietro Massignan Georg M. Bruun Cosetta Baroni, Bo Huang. Mediated interactions between fermi polarons and the role of impurity quantum statistics. 2023.

[30] M. M¨uller E. Rico P. Stebler U.-J. Wiese D. Banerjee, M. Dalmonte and P. Zoller. Atomic quantum simulation of dynamical gauge fields coupled to fermionic matter: From string breaking to evolution after a quench. *Phys. Rev. Lett.*, 2012.

[31] Giorgini S. Pitaevskii L. P. Stringari S Dalfovo, F. Theory of bose-einstein condensation in trapped gases. 1999.

[32] I. B De, S. Spielman. Fermion-mediated long-range interactions between bosons stored in an optical lattice. 2014.

[33] S. De and I. B. Spielman. Fermion-mediated long-range interactions between bosons stored in an optical lattice. *Applied Physics B*, 114(4):527–536, Mar 2014. ISSN 1432-0649. doi:10.1007/s00340-013-5556-5.

[34] Marion Delehaye, Sébastien Laurent, Igor Ferrier-Barbut, Shuwei Jin, Frédéric Chevy, and Christophe Salomon. Critical velocity and dissipation of an ultracold bose-fermi counterflow. *Phys. Rev. Lett. 115*, 115:265303, 2015.

[35] B.J. DeSalvo, Krutik Patel, Geyue Cai, and Cheng Chin. Observation of fermion-mediated interactions between bosonic atoms. *Nature*, 568:61–64, 2019.

[36] B.J. DeSalvo, Krutik Patel, Geyue Cai, and Cheng Chin. Observation of fermion-mediated interactions between bosonic atoms. *Nature*, 568:61–64, 2019.

[37] Brian DeSalvo, Krutik Patel, Geyue Cai, and Cheng Chin. Observation of a degenerate fermi gas trapped by a bose-einstein condensate. *Phys. Rev. Lett.*, 119:233401, 2017.

[38] Patel K. Johansen J. Chin C. DeSalvo, B. J. Observation of a degenerate fermi gas trapped by a bose-einstein condensate. 2017.

[39] Hagai Edri, Boaz Raz, Noam Matzliah, Nir Davidson, and Roee Ozeri. Observation of spin-spin fermion-mediated interactions between ultracold bosons. *Rev. Mod. Lett.*, 124:163401, 2020.

[40] G.M. Eliashberg. Interactions between electrons and lattice vibrations in a superconductor. *J. Exptl. Theoret. Phys.*, 38:9676–976, 1960.

[41] T. Enss and W. Zwerger. "Superfluidity near phase separation in Bose-Fermi mixtures . *Eur. Phys. J. B*, 68:383–389, 2009.

[42] Tilman Enss, Binh Tran, Michael Rautenberg, Manuel Gerken, Eleonora Lippi, Moritz Drescher, Bing Zhu, Matthias Weidemüller, and Manfred Salmhofer. Scattering of two heavy fermi polarons: Resonances and quasibound states. *Phys. Rev. A*, 102:063321, Dec 2020. doi:10.1103/PhysRevA.102.063321. URL `https://link.aps.org/doi/10.1103/PhysRevA.102.063321`.

[43] L. Pieri R. Concas W. J. Kwon G. Roati F. Scazza, G. Del Pace. Two-element mixture of bose and fermi superfluids. *https://arxiv.org/abs/2104.12730*, 2021.

[44] FCalogero. Variable phase approach to potential scattering. 1967.

[45] F. et al Ferlaino. Observation of a degenerate fermi gas trapped by a bose-einstein condensate. 2003.

[46] Inguscio M. Jastrzebski W. Modugno G. Roati G Ferrari, G. Collisional properties of ultracold k-rb mixtures. 2002.

[47] I. et al Ferrier-Barbut. A mixture of bose and fermi superfluids. 2014.

[48] Kadau H. Schmitt M. Wenzel M. Pfau T. Ferrier-Barbut, I. Observation of quantum droplets in a strongly dipolar bose gas. 2016.

[49] Sophie Fisher, Olumakinde Ogunnaike, and Leonid Levitov. Three-body bound states of quantum particles: Higher stability through braiding. *Phys. Rev. A*, 109:043323, Apr 2024. doi:10.1103/PhysRevA.109.043323. URL `https://link.aps.org/doi/10.1103/PhysRevA.109.043323`.

[50] Elisa Fratini and Pierbiagio Pieri. Pairing and condensation in a resonant Bose-Fermi mixture . *Phys. Rev. A*, 81:051605, 2010.

[51] Isabella Fritsche, Cosetta Baroni, Erich Dobler, Emil Kirilov, Bo Huang, Rudolf Grimm, Georg M. Bruun, and Pietro Massignan. Stability and breakdown of fermi polarons in a strongly interacting fermi-bose mixture. *Phys. Rev. Lett. 115*, 103:053314, 2021.

[52] D. Jervis D. C. McKay R. Day S. Trotzky J. H. Thywissen G. J. A. Edge, R. Anderson. Imaging and addressing of individual fermionic atoms in an optical lattice. 2015.

[53] A Gammal, T Frederico, Lauro Tomio, and Ph Chomaz. Atomic bose–einstein condensation with three-body interactions and collective excitations. *J. Phys. B: At. Mol. Opt. Phys.*, 33:4053–4067, 2000.

[54] Krzysztof Gawryluk, Tomasz Karpiuk, Mariusz Gajda, Kazimierz Rzazewski, and Miroslaw Brewczyk. Unified way for computing dynamics of Bose–Einstein condensates and degenerate Fermi gases . *Int. J. Comput. Math.*, 95:11:2143–2161, 2018.

[55] Joseph M. Geary. Introduction to lens design with zemax examples. 2002.

[56] M. Gehm. Properties of 6li. 2003.

[57] S. Giorgini. Damping in dilute bose gases: A mean-field approach. *Phys. Rev. A*, 57: 2949–2957, Apr 1998. doi:10.1103/PhysRevA.57.2949. URL https://link.aps.org/doi/10.1103/PhysRevA.57.2949.

[58] Francesco Riboli Francesca Ferlaino Robert J. Brecha Giovanni Modugno, Giacomo Roati and Massimo Inguscio. Collapse of a degenerate fermi gas. *Science*, 2002.

[59] Feliciano Giustino. Electron-phonon interactions from first principles. *Rev. Mod. Phys.*, 89:015003, Feb 2017. doi:10.1103/RevModPhys.89.015003. URL https://link.aps.org/doi/10.1103/RevModPhys.89.015003.

[60] JOSEPH W. GOODMAN. Introduction to fourier optics. 1996.

[61] JOSEPH W. GOODMAN. Statistical optics. 2000.

[62] Andrew T. Grier, Igor Ferrier-Barbut, Benno S. Rem, Marion Delehaye, Lev Khaykovich, Frédéric Chevy, and Christophe Salomon. Λ-enhanced sub-doppler cooling of lithium atoms in D_1 gray molasses. *Phys. Rev. A*, 87:063411, Jun 2013. doi:10.1103/PhysRevA.87.063411. URL https://link.aps.org/doi/10.1103/PhysRevA.87.063411.

[63] E. et al. Guardado-Sanchez. Probing the quench dynamics of antiferromagnetic correlations in a 2d quantum ising spin system. 2018.

[64] Kenneth Günter, Thilo Stöferle, Henning Moritz, Michael Köhl, and Tilman Esslinger. Bose-fermi mixtures in a three-dimensional optical lattice. *Phys. Rev. Lett.*, 96:180402, 2006.

[65] Z. Hadzibabic, C. A. Stan, K. Dieckmann, S. Gupta, M. W. Zwierlein, A. Görlitz, and W. Ketterle. Two-species mixture of quantum degenerate bose and fermi gases. *Phys. Rev. Lett.*, 88:160401, Apr 2002. doi:10.1103/PhysRevLett.88.160401. URL https://link.aps.org/doi/10.1103/PhysRevLett.88.160401.

[66] K. R. A. et al. Hazzard. Many-body dynamics of dipolar molecules in an optical lattice. 2014.

[67] Carl E. Wieman; Leo Hollberg. Using diode lasers for atomic physics. *Review of Scientific Instruments*, 1991.

[68] T. Holstein. Studies of polaron motion : Part i. the molecular-crystal model. *Annals of Physics*, 8(3):325–342, 1959.

[69] Feng L. Zhang Z. et al Hu, J. Quantum simulation of unruh radiation. *Nat. Phys.*, 2019.

[70] Bo Huang. Bose-einstein condensate immersed in a fermi sea: Theory of static and dynamic behavior across phase separation. *Phys. Rev. A*, 101:063618, 2020.

[71] Bo Huang, Isabella Fritsche, Rianne S. Lous, Cosetta Baroni, Jook T. M. Walraven, Emil Kirilov, , and Rudolf Grimm. Breathing mode of a bose-einstein condensate repulsively interacting with a fermionic reservoir. *Phys. Rev. A*, 99:041602(R), 2019.

[72] Klaus Hueck, Niclas Luick, Lennart Sobirey, Jonas Siegl, Thomas Lompe, Henning Moritz, Logan W. Clark, and Cheng Chin. Calibrating high intensity absorption imaging of ultracold atoms. *Opt. Express*, 25(8):8670–8679, Apr 2017. doi:10.1364/OE.25.008670. URL `https://opg.optica.org/oe/abstract.cfm?URI=oe-25-8-8670`.

[73] S. Laurent A. T. Grier M. Pierce B. S. Rem F. Chevy I. Ferrier-Barbut, M. Delehaye and C. Salomon. A mixture of bose and fermi superfluids. *Science*, 2014.

[74] Andrews M. Stenger J. et al. Inouye, S. Observation of feshbach resonances in a bose–einstein condensate. *Nature*, 1998. URL `https://doi.org/10.1038/32354`.

[75] Daniel González-Cuadra Javier Argüello-Luengo, Alejandro González-Tudela. Tuning long-range fermion-mediated interactions in cold-atom quantum simulators. *PRL*, 2022.

[76] Fred Jegerlehner and Andreas Nyffeler. The muon g2. *Physics Reports*, 477(1):1–110, 2009. ISSN 0370-1573. doi:https://doi.org/10.1016/j.physrep.2009.04.003. URL `https://www.sciencedirect.com/science/article/pii/S0370157309001306`.

[77] Yuzhu Jiang, Ran Qi, Zhe-Yu Shi, and Hui Zhai. Vortex lattices in the bose-fermi superfluid mixture. *Phys. Rev. Lett.*, 118:080403, Feb 2017. doi:10.1103/PhysRevLett.118.080403. URL `https://link.aps.org/doi/10.1103/PhysRevLett.118.080403`.

[78] DeSalvo B. J.-Patel K. Chin C. Johansen, J. Testing universality of efimov physics across broad and narrow feshbach resonances. 2017.

[79] J. Johansen. Feshbach and efimov resonances in a ^{6}li - ^{133}cs atomic mixture. 2017.

[80] Jacob Johansen, B.J. DeSalvo, Krutik Patel, Geyue Cai, and Cheng Chin. Testing universality of efimov physics across broad and narrow feshbach resonances. *Nature Physics*, 13:731–735, 2017.

[81] Peter W. Epperlein A John. Semiconductor laser engineering, reliability and diagnostics: A practical approach to high power and single mode devices. 1991.

[82] J. Joseph, B. Clancy, L. Luo, J. Kinast, A. Turlapov, and J. E. Thomas. Measurement of sound velocity in a fermi gas near a feshbach resonance. *Phys. Rev. Lett.*, 98:170401, 2007.

[83] T. et al Karpiuk. Soliton trains in bose-fermi mixtures. 2004.

[84] Tomasz Karpiuk, Mariusz Gajda, and Mirosaw Brewczyk. Bistability of bose–fermi mixtures. *New J. Phys*, 22:103025, 2020.

[85] Tomasz Karpiuk, Marek Nikołajuk, Mariusz Gajda, and Mirosaw Brewczyk. Modelling quantum aspects of disruption of a white dwarf star by a black hole. *Sci Rep*, 11:2286, 2021.

[86] Savely G. Karshenboim. Precision physics of simple atoms: Qed tests, nuclear structure and fundamental constants. *Physics Reports*, 422(1):1–63, 2005. ISSN 0370-1573. doi:https://doi.org/10.1016/j.physrep.2005.08.008. URL https://www.sciencedirect.com/science/article/pii/S0370157305003637.

[87] A. M. Kaufman, B. J. Lester, and C. A. Regal. Cooling a single atom in an optical tweezer to its quantum ground state. *Phys. Rev. X*, 2:041014, Nov 2012. doi:10.1103/PhysRevX.2.041014. URL https://link.aps.org/doi/10.1103/PhysRevX.2.041014.

[88] G.M. Kavoulakis and C.J. Pethick. Quasi-one-dimensional character of sound propagation in elongated bose-einstein condensed clouds. *Phys. Rev. A*, 58:1563, 1998.

[89] Dam Thanh Son Ke Wang, Thimo Preis. Droplets of bosons at a narrow resonance. 2024. doi:https://doi.org/10.48550/arXiv.2407.03102.

[90] Shu Nagata Zhiqiang Wang K. Levin Ke Wang, Zhendong Zhang. Dynamics of the unitary bose gas near a narrow feshbach resonance: universal coherent atom-molecule oscillations. 2024. doi:https://doi.org/10.48550/arXiv.2408.08415.

[91] B. Keimer, S. A. Kivelson, M. R. Norman, S. Uchida, and J Zaanen. From quantum matter to high-temperature superconductivity in copper oxides. *Nature*, 518:179–186, 2015.

[92] Andrew J. Kerman, Vladan Vuletić, Cheng Chin, and Steven Chu. Beyond optical molasses: 3d raman sideband cooling of atomic cesium to high phase-space density. *Phys. Rev. Lett.*, 84:439–442, Jan 2000. doi:10.1103/PhysRevLett.84.439. URL https://link.aps.org/doi/10.1103/PhysRevLett.84.439.

[93] Jami Kinnunen, Zhigang Wu, and Georg M. Bruun. Induced p-wave pairing in bose-fermi mixtures. *Phys. Rev. Lett.*, 121:253402, 2018.

[94] M. Kulic. Interplay of electron–phonon interaction and strong correlations: the possible way to high-temperature superconductivity. *Physics Reports*, 338:1–264, 2000.

[95] W. E. Lamb and R. C. Rutherford. Fine structure of the hydrogen atom by a microwave method. *Phys. Rev.*, 72:241, 1947.

[96] A Lanzara, P. V. Bogdanov, X. J. Zhou, S. A. Kellar, D. L. Feng, E. D. Lu, T. Yoshida, H. Eisaki, A. Fujimori, K. Kishio, T. Noda J.-I. Shimoyam and, S. Uchida, Z. Hussain, and Z.-X. Shen. Evidence for ubiquitous strong electron-phonon coupling in high-temperature superconductors. *Nature*, 412:510–514, 2001.

[97] Williams C. J. Julienne P. S. Leo, P. J. Collision properties of ultracold ^{133}cs atoms. 2000.

[98] R. S. et al Lous. Probing the interface of a phaseseparated state in a repulsive bose-fermi mixture. 2018.

[99] Burdick N. Q. Youn S. H. Lev B. L. Lu, M. Strongly dipolar bose-einstein condensate of dysprosium. 2011.

[100] L.Viverit and S. Giorgini. Ground-state properties of a dilute bose-fermi mixture. *Phys. Rev. A*, 66:063604, 2002.

[101] David James MacNeill and Fei Zhou. Pauli blocking effect on efimov states near a feshbach resonance. *Phys. Rev. Lett.*, 106:145301, Apr 2011. doi:10.1103/PhysRevLett.106.145301. URL `https://link.aps.org/doi/10.1103/PhysRevLett.106.145301`.

[102] Koki Manabe and Yoji Ohashi. Thermodynamic stability, compressibility matrices, and effects of mediated interactions in a strongly interacting bose-fermi mixture. *Phys. Rev. A*, 103:063317, Jun 2021. doi:10.1103/PhysRevA.103.063317. URL `https://link.aps.org/doi/10.1103/PhysRevA.103.063317`.

[103] Francesca M. Marchetti, Charls J. M. Mathy, and David A. Huse. Phase separation and collapse in Bose-Fermi mixtures with a Feshbach resonance . *Phys. Rev. B*, 78: 134517, 2008.

[104] Bogdan Mihaila. Lindhard function of a d-dimensional fermi gas. 2011.

[105] Arpita Das Matthew D. Frye Yanliang Guo Jeremy M. Hutson Manuele Landini Hanns-Christoph Nägerl Milena Horvath, Sudipta Dhar. Bose-einstein condensation of non-ground-state caesium atoms. 2024.

[106] Daniel T. Colbert; William H. Miller. A novel discrete variable representation for quantum mechanical reactive scattering via the s-matrix kohn method. *J. Chem. Phys*, 1991.

[107] David D. Grimes Yen-Wei Lin Andrei H. Gheorghe Romain Vexiau Nadia Bouloufa-Maafa Olivier Dulieu Till Rosenband Kang-Kuen Ni Ming-Guang Hu, Yu Liu. Direct observation of bimolecular reactions of ultracold krb molecules. 2019.

[108] Takahiko Miyakawa, Hiroyuki Yabu, and Toru Suzuki. Peierls instability, periodic bose-einstein condensates, and density waves in quasi-one-dimensional boson-fermion mixtures of atomic gases. *Phys. Rev. A*, 70:013612, 2004.

[109] Klaus Molmer. Bose condensates and fermi gases at zero temperature. *Phys. Rev. Lett.*, 80:1804, 1998.

[110] Takuya Ikemachi Yukihito Aratake Makoto Kuwata-Gonokami Masato Koashi Munekazu Horikoshi, Aki Ito. Appropriate probe condition for absorption imaging of ultracold ^6li atoms. *J. Phys. Soc. Jpn.*, 2017.

[111] Y. Nambu. Quasi-particles and gauge invariance in the theory of superconductivity. *Phys. Rev.*, 117:648, 1960.

[112] K.-K. Ni, S. Ospelkaus, M. H. G. de Miranda, A. Pe'er, B. Neyenhuis, J. J. Zirbel, S. Kotochigova, P. S. Julienne, D. S. Jin, and J. Ye. A high phase-space-density gas of polar molecules. *Science*, 322:231–235, 2008.

[113] K.-K. et al. Ni. A high phase-space-density gas of polar molecules. 2008.

[114] Yusuke Nishida. Casimir interaction among heavy fermions in the bcs-bec crossover. *Phys. Rev. A*, 79:013629, 2009.

[115] Yusuke Nishida. Nishida2009. *Phys. Rev. A*, 79:013629, Jan 2009. doi:10.1103/PhysRevA.79.013629. URL `https://link.aps.org/doi/10.1103/PhysRevA.79.013629`.

[116] G. L. Oliver and J. P. Perdew. Spin-density gradient expansion for the kinetic energy . *Phys. Rev. A.*, 20:397, 1979.

[117] S. Ospelkaus, C. Ospelkaus, O. Wille, M. Succo, P. Ernst, K. Sengstock, and K. Bongs. Localization of bosonic atoms by fermionic impurities in a three-dimensional optical lattice. *Phys. Rev. Lett.*, 96:180403, 2006.

[118] David Laroze Pablo Díaz and Boris A Malomed. Correlations and synchronization in a bose–fermi mixture. 2015.

[119] Rosario Paredes, Georg Bruun, and Arturo Camacho-Guardian. Interactions mediated by atoms, photons, electrons, and excitons. *Phys. Rev. A*, 110:030101, Sep 2024. doi:10.1103/PhysRevA.110.030101. URL `https://link.aps.org/doi/10.1103/PhysRevA.110.030101`.

[120] K. Patel. Interactions and excitations in quantum degenerate 133cs-6li bose-fermi mixtures. 2022.

[121] Krutik Patel, Geyue Cai, Henry Ando, and Cheng Chin. Sound propagation in a Bose-Fermi mixture: From weak to strong interactions. *Physical Review Letters*, 131(8):083003, August 2023. ISSN 0031-9007, 1079-7114. doi:10.1103/PhysRevLett.131.083003.

[122] E. Pazy and A. Vardi. Holstein model and peierls instability in one-dimensional boson-fermion lattice gases. *Phys. Rev. A*, 72:033609, 2005.

[123] C. Pethick and H. Smith. *Bose-Einstein condensation in dilute gases*. Cambridge University Press, 2002.

[124] D. Rakshit, Tomasz Karpiuk, Miroslaw Brewcyzk, and Mariusz Gajda. Quantum bose-fermi droplets. *SciPost Phys.*, 6:079, 2019.

[125] Ryan Bowler Richard Roy, Alaina Green and Subhadeep Gupta. Two-element mixture of bose and fermi superfluids. *PRL*, 2017.

[126] R.Meppelink, S.B.Koller, and P.van der Straten. Sound propagation in a bose-einstein condensate at finite temperatures. *Phys. Rev. A*, 80:043605, 2009.

[127] G. Roati, F. Riboli, G. Modugno, and M. Inguscio. Fermi-bose quantum degenerate ^{40}K$-^{87}$Rb mixture with attractive interaction. *Phys. Rev. Lett.*, 89:150403, Sep 2002. doi:10.1103/PhysRevLett.89.150403. URL `https://link.aps.org/doi/10.1103/PhysRevLett.89.150403`.

[128] R. Roth and H. Feldmeier. Mean-field instability of trapped dilute boson-fermion mixtures. *Phys. Rev. A*, 65:021603(R), 2002.

[129] Green A. Bowler R. Gupta S. Roy, R. Two-element mixture of bose and fermi superfluids. 2017.

[130] C. Ruderman, M. A. Kittel. Indirect exchange coupling of nuclear magnetic moments by conduction electrons. 1954.

[131] M. A. Ruderman and C. Kittel. Indirect exchange coupling of nuclear magnetic moments by conduction electrons. *Phys. Rev.*, 96:99–102, Oct 1954. doi:10.1103/PhysRev.96.99.

[132] D. H. Timmermans Santamore. Fermion-mediated interactions in a dilute bose-einstein condensate. 2008.

[133] Kenkre V. M. Konotop V. V. Santhanam, J. Solitons of bose-fermi mixtures in a strongly elongated trap. 2006.

[134] C. L. Satter, S. Tan, and K. Dieckmann. Comparison of an efficient implementation of gray molasses to narrow-line cooling for the all-optical production of a lithium quantum gas. *Phys. Rev. A*, 98:023422, Aug 2018. doi:10.1103/PhysRevA.98.023422. URL `https://link.aps.org/doi/10.1103/PhysRevA.98.023422`.

[135] F. Schreck, L. Khaykovich, K. L. Corwin, G. Ferrari, T. Bourdel, J. Cubizolles, and C. Salomon. Quasipure bose-einstein condensate immersed in a fermi sea. *Phys. Rev. Lett.*, 87:080403, Aug 2001. doi:10.1103/PhysRevLett.87.080403. URL `https://link.aps.org/doi/10.1103/PhysRevLett.87.080403`.

[136] J. Schwinger. On quantum-electrodynamics and the magnetic moment of the electron. *Phys. Rev. A.*, 1948.

[137] J. Schwinger. p-wave cooper pairing of fermions in mixtures of dilute fermi and bose gases. *Phys. Rev. B.*, 2002.

[138] I. Shammass, S. Rinott, A. Berkovitz, R. Schley, and J. Steinhauer. Phonon dispersion relation of an atomic bose-einstein condensate. *Phys. Rev. Lett.*, 109:195301, Nov 2012. doi:10.1103/PhysRevLett.109.195301. URL `https://link.aps.org/doi/10.1103/PhysRevLett.109.195301`.

[139] Xin Shen, Nir Davidson, Georg M. Bruun, Mingyuan Sun, and Zhigang Wu. Strongly interacting bose-fermi mixtures: Mediated interaction, phase diagram, and sound propagation. *Phys. Rev. Lett.*, 132:033401, Jan 2024. doi:10.1103/PhysRevLett.132.033401. URL `https://link.aps.org/doi/10.1103/PhysRevLett.132.033401`.

[140] Steven W. Smith. Digital signal processing. 1999.

[141] Warren J. Smith. Modern lens design. 1992.

[142] John Sous, Monodeep Chakraborty, Roman V. Krems, and Mona Berciu. Light bipolarons stabilized by peierls electron-phonon coupling. *Phys. Rev. Lett.*, 121:247001, 2018.

[143] D. Steck. Cesium d line data. 1998.

[144] Jayampathi C. B. Kangara; Andrew J. Hachtel; Matthew C. Gillette; Jason T. Barkeloo; Ethan R. Clements; Samir Bali; Brett E. Unks; Nicholas A. Proite; Deniz D. Yavuz; Paul J. Martin; Jeremy J. Thorn; Daniel A. Steck. Design and construction of cost-effective tapered amplifier systems for laser cooling and trapping experiments. *American Journal of Physics*, 2014.

[145] J. Stenger, S. Inouye, A. P. Chikkatur, D. M. Stamper-Kurn, D. E. Pritchard, and W. Ketterle. Bragg spectroscopy of a bose-einstein condensate. *Phys. Rev. Lett.*, 82: 4569–4573, Jun 1999. doi:10.1103/PhysRevLett.82.4569. URL `https://link.aps.org/doi/10.1103/PhysRevLett.82.4569`.

[146] Wu Z. Chevy F. Bruun G. M. Suchet, D. Longrange mediated interactions in a mixed-dimensional system. 2017.

[147] Seiji Sugawa, Kensuke Inaba, Shintaro Taie, Rekishu Yamazaki, Makoto Yamashita, and Yoshiro Takahashi. Interaction and filling-induced quantum phases of dual mott insulators of bosons and fermions. *Nature Physics*, 7:642–648, 2011.

[148] J. Szczepkowski, R. Gartman, M. Witkowski, L. Tracewski, M. Zawada, and W. Gawlik. Analysis and calibration of absorptive images of bose–einstein condensate at nonzero temperatures. *Review of Scientific Instruments*, 80(5):053103, 05 2009. ISSN 0034-6748. doi:10.1063/1.3125051. URL `https://doi.org/10.1063/1.3125051`.

[149] M Tinkham. Introduction to superconductivity. 1975.

[150] Toptica. Alignment of a dfb mopa system with dfb tpa configuration. URL https://toptica-eagleyard.com/wp-content/uploads/2023/01/eyP_AppNote_TPA_2-0.pdf.

[151] M. Tsurumi, T. Wadati. Dynamics of magnetically trapped boson-fermion mixtures. 2000.

[152] S. K. et al. Tung. Ultracold mixtures of atomic ^{6}li and ^{133}cs with tunable interactions. 2013.

[153] Shih Kuang Tung, Karina Jimenez-Garcia, Jacob Johansen, Colin V. Parker, and Cheng Chin. Geometric scaling of efimov states in a ^{6}Li - ^{133}Cs mixture. *Phys. Rev. Lett.*, 113:240402, 2014. ISSN 10797114. doi:10.1103/PhysRevLett.113.240402.

[154] S.K. Tung, Colin Parker, Jacob Johansen, Cheng Chin, Yujun Wang, and Paul S. Julienne. Ultracold mixtures of atomic ^{6}li and ^{1}33 cs with tunable interactions. *Phys. Rev. A*, 87:010702(R), 2013.

[155] J Ulmanis, S Häfner, R Pires, E D Kuhnle1, M Weidemüller, and E Tiemann. Universality of weakly bound dimers and efimov trimers close to li–cs feshbach resonances. *New J. Phys.*, 17:055009, 2015.

[156] Romain Veyron, Vincent Mancois, Jean-Baptiste Gerent, Guillaume Baclet, Philippe Bouyer, and Simon Bernon. Quantitative absorption imaging: The role of incoherent multiple scattering in the saturating regime. *Phys. Rev. Res.*, 4:033033, Jul 2022. doi:10.1103/PhysRevResearch.4.033033. URL https://link.aps.org/doi/10.1103/PhysRevResearch.4.033033.

[157] Jo˜ao P. Braga Vitor D. Viterbo1, Nelson H.T. Lemes. Variable phase equation in quantum scattering. *Revista Brasileira de Ensino de Física*, 2014.

[158] L. Viverit, C. J. Pethick, and H. Smith. Zero-temperature phase diagram of binary boson-fermion mixtures. *Phys. Rev. A*, 61:053605, 2000.

[159] D.S. Durfee W. Ketterle and D.M. Stamper-Kurn. Making, probing and understanding bose-einstein condensates. 1999.

[160] Jia Wang, J. P. D'Incao, B. D. Esry, and Chris H. Greene. Origin of the three-body parameter universality in efimov physics. *Phys. Rev. Lett.*, 108:263001, Jun 2012. doi:10.1103/PhysRevLett.108.263001. URL https://link.aps.org/doi/10.1103/PhysRevLett.108.263001.

[161] Yujun Wang, Jia Wang, J. P. D'Incao, and Chris H. Greene. Universal three-body parameter in heteronuclear atomic systems. *Phys. Rev. Lett.*, 109:243201, Dec 2012. doi:10.1103/PhysRevLett.109.243201. URL https://link.aps.org/doi/10.1103/PhysRevLett.109.243201.

[162] Yu-Ping Wu Xiang-Pei Liu Xiao-Qiong Wang Xiao Jiang Youjin Deng Yu-Ao Chen Jian-Wei Pan Xing-Can Yao, Hao-Ze Chen. Two-element mixture of bose and fermi superfluids. *PRL*, 2016.

[163] Zoe Yan, Yiqi Ni, Carsten Robens, and Martin W. Zwierlen. Bose polarons near quantum criticality. *Science*, 368:190–104, 2020.

[164] S.K. Yip. Collective modes in a dilute bose-fermi mixture. *Phys. Rev. A*, 64:023609, 2001.

[165] H Yukawa. On the interaction of elementary particles i. 1935.

[166] S Yukawa, H. Sakata. On the interaction of elementary particles ii. 1937.

[167] Keisuke Fujii Masaru Hongo Yukinao Akamatsu, Shimpei Endo. Complex-valued in-medium potential between heavy impurities in ultracold atoms. *Physical Review A*, 2023.

[168] J. et al. Zeiher. Many-body interferometry of a rydbergdressed spin lattice. 2016.

[169] Nagata S. Yao KX. et al Zhang, Z. Many-body chemical reactions in a quantum degenerate gas. *Nat. Phys.*, 2023.

[170] Dong-Chen Zheng, Chun-Rong Ye, Lin Wen, and Renyuan Liao. Polarizing the medium: Fermion-mediated interactions between bosons. *Phys. Rev. A*, 103:L021301, Feb 2021. doi:10.1103/PhysRevA.103.L021301. URL `https://link.aps.org/doi/10.1103/PhysRevA.103.L021301`.